UNIVERSIDADE DE SÃO PAULO
INSTITUTO DE FÍSICA DE SÃO CARLOS

LAIS RIBOVSKI

Bionanomaterials for biological barrier crossing and controlled drug delivery

São Carlos
2020

LAIS RIBOVSKI

Bionanomateriais para o cruzamento de barreira biológica e entrega controlada

Tese apresentada ao Programa de Pós-Graduação em Física do Instituto de Física de São Carlos da Universidade de São Paulo - Brasil e Faculty of Medical Sciences, University Medical Center Groningen, University of Groningen, Países Baixos para obtenção da Dupla Titulação de Doutora em Ciências.

Área de concentração: Física Aplicada
Opção: Física Biomolecular
Orientadores:
Prof. Dr.Valtencir Zucolotto
Profª. Drª.Inge S. Zuhorn
Profª. Drª Juliana Cancino-Bernardi
Prof. Dr.Patrick van Rijn

Versão Corrigida

(versão original disponível na Unidade que aloja o Programa)

São Carlos
2020

Ribovski, Lais
Bionanomateriais para o cruzamento de barreira biológica e entrega controlada / Lais Ribovski; orientador Valtencir Zucolotto; co-orientadora Juliana Cancino-Bernardi - versão corrigida -- São Carlos, 2020.
158 p.

Tese (Doutorado - Programa de Pós-Graduação em Física Aplicada Biomolecular) -- Instituto de Física de São Carlos, Universidade de São Paulo, 2020.

1. Nanomedicina. 2. Barreira hematoencefálica. 3. Entrega controlada. 4. Câncer. I. Zucolotto, Valtencir, orient. II. Cancino-Bernardi, Juliana, co-orient. III. Título.

LAIS RIBOVSKI

Bionanomaterials for biological barrier crossing and controlled drug delivery

Thesis presented to the Graduate Program in Physics at the Instituto de Física de São Carlos, Universidade de São Paulo, Brazil and Institute of Physics, Faculty of Medical Sciences, University Medical Center Groningen, University of Groningen, The Netherlands to obtain the double degree of Doctor of Science.

Concentration area: Applied Physics
Option: Biomolecular Physics
Advisors:
Prof. Dr.Valtencir Zucolotto
Profª. Drª.Inge S. Zuhorn
Profª. Drª Juliana Cancino-Bernardi
Prof. Dr. Patrick van Rijn

Corrected Version

(original version available on the Program Unit)

São Carlos
2020

Ribovski, Lais
Bionanomaterials for biological barrier crossing and controlled drug delivery / Lais Ribovski; advisor Valtencir Zucolotto; co-advisor Juliana Cancino-Bernardi - corrected version -- São Carlos 2020.
158 p.

Thesis (Doctorate - Graduate Program in Biomolecular Physics) -- Instituto de Física de São Carlos, Universidade de São Paulo - Brasil University Medical Center Groningen, 2020.

1. Nanomedicine. 2. Blood-brain barrier. 3. Controlled drug delivery. 4. Câncer. I. Zucolotto, Valtencir, advisor. II. Cancino-Bernardi, Juliana, co-advisor. III. Title.

ACKNOWLEDGEMENTS

To my parents, Vivian and Edilberto, I would like to thank you for your continuous support. Even not fully comprehending what I do, you are always a safe house and it allows me to go for bigger challenges.

To my amazing sister Marina, for simply being who you are and always making me proud of being your sister.

To my grandparents, for all your love and wisdom.

To my lovely grandmother Izabel for always be an inspiration and amazing role model.

I would like to thank Cecilia, Ewout, Tobias and Casper for being my family in the Netherlands and always welcome me in your house.

To my godparents, Ives and Eulália, who worried about me and always have a kind word to say.

To my dearest boyfriend who always takes such good care of me even when I forget to do myself. Your patience and kindness always comfort me.

I would like to thank all my supervisors who contribute to every word in this thesis. Inge, you constantly impress me, I learn a lot from every scientific discussion we had. I would like to thank you and Patrick for always motivating me. I also would like to. thank Zucolotto and Juliana for all the thrust and freedom you gave through those many years.

A more than special thank you for Paula's friendship and support through those years. Our delightful morning coffee routine would boost my motivation for a whole day of experiments. Also, for all the remote help with the endless bureaucratic issues and for giving me the motivation to finish writing the thesis.

To all the members of the Nanomedicine and Nanotoxicology Group (GNano), especially Bruna, Romeu e Simone for all your support.

To all Zuhorn's group members for been such nice and friendly colleagues. I would like to thank Edwin for all the very useful insights about the BBB model and for always being so helpful.

To the members of Patrick's group also for being great colleagues. Specially our microgel team Guangyue, Damla, Olga and Clio.

A warm thank to Cris and Olavo for always being such great colleagues and friends inside and outside the lab.

To Raissa, I could not thank you enough for your friendship and way of always make things better with your contaminant sweetness.

To Luana, Aline, Mirjam, Maíra and many other students that even briefly I could collaborate to your projects and learn a lot with you.

I am grateful to the University of São Paulo for all the high-quality education I received through the years and all the infra-structure provided to develop my research. I also thank all the staff for the technical and bureaucratic support. Silvio and Ricardo for always handling the endless administrative paperwork.

To Maria Neusa and all library support team, your help and patience made the whole correction and approval processes more enjoyable. Thank you.

I thank the University of Groningen for providing a great environment for research and a nice ensemble of interesting courses for the development of my carrier as a researcher, especially the Faculty of Medical Sciences, University Medical Center Groningen. Also, I

am very grateful to the staff of the Biomedical Engineering Department for being always so helpful and professional creating a nice work environment.

I thank Reinier for trying to keep the cell culture organized, but mainly for was always be very helpful and willing to discuss protocols and experimental troubleshooting.

I would to thank all the professors that teach me so much about science and inspired me with your passion. Special thanks to professors Alessandro Nascimento and Franscisco Alcaraz for accepting me as assistant student during your courses. I learned a lot watching you teach and manage students.

I also would like to thank the Coordenação de Aperfeiçoamento de Pessoal de Nível Superior (CAPES) for financing my PhD scholarship in Brazil. This study was financed in part by the Coordenação de Aperfeiçoamento de Pessoal de Nível Superior - Brasil (CAPES) - Finance Code 001.

I would like to thank the The Abel Tasman Talent Program of the Graduate School of Medical Sciences of the University of Groningen for the funding during my years in Groningen.

To the de Cock-Hadders Stichting, thank for the grant that support part of my PhD research in Groningen.

Inspired by Olavo Amorin, I should leave my gratitude to all the cells that honorably sacrificed their lives for this higher cause and apologize for those ones that died in vain from my mistakes. I will never forget each one of you.

RESUMO

RIBOVSKI, L. **Bionanomateriais para o cruzamento de barreira biológica e entrega controlada**. 2020. 158 p. Tese (Doutorado em Ciências) - Instituto de Física de São Carlos, Universidade de São Paulo, São Carlos, 2020.

Sistemas de liberação em nanoescala, capazes de identificar e responder ativamente e com precisão a estímulos externos ou internos ao microambiente celular visando uma cinética de liberação sob demanda, são de grande interesse para a liberação de compostos terapêuticos. No entanto, para o desenvolvimento desses sistemas, é necessária uma profunda compreensão da interação entre nanomaterial e células. No capítulo I desta tese, descrevemos como nanogéis (NGs) de acrilamida no seu estado intumescido e com diferentes densidades de reticulação, (e consequentemente, diferente rigidez) são internalizados por uma monocamada polarizada de células endoteliais microvasculares cerebrais humanas (hCMEC / D3), e como isso se correlaciona com sua capacidade de atravessar a barreira hematoencefálica (BBB). Os NGs mais rígidos mostraram uma maior captação pela camada celular polarizada, enquanto os NGs mais elásticos exibiram maior capacidade em atravessar a BBB sem comprometer a permeabilidade da monocamada, sendo que 8,2, 7,5 e 5,2% dos NGs atingiram o compartimento basolateral após 16 horas de incubação a 37 ° C em atmosfera úmida com 5% de CO_2. Também observamos que a taxa de transporte dos NGs é elevada nas duas horas iniciais de interação. Os mesmos NGs descritos no Capítulo I foram empregados em um segundo estudo relatado no Capítulo II, para avaliar a resposta da rigidez em monocultura 2D e na co-cultura direta de células de glioma, C6, e macrófagos, J774, em relação à internalização e à citotoxicidade dos NGs. Os resultados apontam uma internalização favorecida pelos NGs mais rígidos, e um efeito tóxico mais elevado do NG mais elástico. O capítulo III aborda o desenvolvimento e a avaliação *in vitro* de nanocarreadores (NCs) revestidos por membrana de células de câncer de mama (MCF-7), compostos de poli (D, ácido L-láctico-co-glicólico) (PLGA) e contendo paclitaxel (PTX) como fármaco modelo. O carreamento do fármaco em PLGA-PTX NCs foi de aproximadamente 4 wt% (98 ± 1% da eficiência do encapsulamento) e apresentou redução significativa da viabilidade

celular contra células de câncer de mama quando comparado aos NCs não revestidos (interação homotípica) e ainda, exibiu um aumento da associação de NCs revestidos por membrana com outros tipos de células epiteliais. O Capítulo IV descreve o projeto e desenvolvimento de um sistema de liberação sob demanda induzido pela luz, empregando motores moleculares hidrofóbicos (MM) para desestabilizar a bicamada lipídica de lipossomos compostos por lipídios insaturados. Demonstramos que a combinação dos lipossomas com o MM resultou em um sistema de liberação sensível à luz controlável.

Palavras-chave: Nanomedicina. Barreira hematoencefálica. Entrega controlada. Câncer

ABSTRACT

RIBOVSKI, L. **Bionanomaterials for biological barrier crossing and controlled drug delivery**. 2020. 158 p. Tese (Doutorado em Ciências) - Instituto de Física de São Carlos, Universidade de São Paulo, São Carlos, 2020.

Nanoscale delivery systems capable of actively identify and respond precisely to external stimuli or internal cues in the cellular microenvironment aiming *on demand* kinetics release are of great interest to the delivery of therapeutic compounds. However, to be able to create these systems a deep understanding of nanomaterial-cell interaction is necessary. In the Chapter I of this thesis, we describe how swollen acrylamide nanogels (NGs) with different cross-linking densities and, consequently, different stiffnesses are internalized by a polarized monolayer of human cerebral microvascular endothelial cells (hCMEC/D3) and how does it correlate with their ability to cross the blood-brain barrier (BBB) using a filter-free *in vitro* BBB model. The harder NGs showed a higher uptake by the polarized cell layer while the softer NGs exhibited an enhanced capacity of crossing the BBB without affecting the monolayer permeability with 8.2, 7.5 and 5.2 % of NGs reaching the basolateral compartment after 16 hours incubation at 37 °C in humidified atmosphere with 5% CO_2. We also observed that NGs transport rate is elevated in the first 2 hours of interaction. The same NGs described in Chapter I were employed in a second study reported in Chapter II to assess the effect of their varied stiffness in 2D monoculture and direct coculture of C6 glioma cells and J774 macrophages regarding NGs internalization and cytotoxicity. The results showed a preferred internalization of harder NGs but a higher toxic effect from the softer NG, NG1.5. Chapter III addresses the development and *in vitro* evaluation of MCF-7 breast cancer cell membrane-coated nanocarriers (NCs) composed of poly (D, L-lactic-co-glycolic acid) (PLGA) and containing paclitaxel as a drug model. The PLGA-PTX NCs drug loading is roughly 4 wt% (98 ± 1% of encapsulation efficiency) and presented significant reduction of cell viability against breast cancer cells when compared to the non-coated NCs (homotypic interaction), and also reveals the increased membrane-coated NCs association with other epithelial cell types. To conclude, Chapter IV describes the design and development of a light-induced on demand release system

employing hydrophobic molecular motors (MM) to destabilize the lipid bilayer of liposomes composed of unsaturated lipid. We demonstrate that the combination of the liposomes with the MM resulted in a controllable light-sensitive release system.

Keywords: Nanomedicine. Blood-brain barrier. Controlled drug delivery. Cancer.

LIST OF FIGURES

Figure 1.1 – Schematic representation of the blood-brain barrier and main transport systems. A) Cross-sectional view of a cerebral capillary of the blood-brain barrier. B) Diagram of mechanisms of transport across the blood-brain barrier. 42

Figure 1.2 – Schematic representation of a typical *in vitro* blood-brain barrier model using a Transwell® insert. Endothelial cells are seeded on an ECM-coated porous membrane and grown to form a polarized monolayer of endothelial cells. 43

Figure 1.3 – Simplified representation of the quantification of NP transport in the filter-free BBB model. hCMEC/D3 cells are grown for 5 days on top of a collagen gel until they form a polarized cell monolayer that shows restrictive permeability. Then nanomaterials are applied on top of the monolayer. Following incubation, the apical, cellular and basolateral fractions are separated using collagenase A treatment and centrifugation. Each fraction is collected and transendothelial delivery is evaluated by fluorescence spectroscopy. 44

Figure 2.1 - pNIPMAM nanogel characterization. pNIPMAM nanogel images obtained by negative staining by transmission electron microscopy with A) 1.5 mol% BIS (NG1.5), B) 5 mol% BIS (NG5), C) 14 mol% BIS (NG14) and D) 5 mol% BIS (NG5l^{arge}). E) Swelling ratio of NG1.5, NG5 and NG14, and F) thermoresponsive curves displaying the hydrodynamic diameter as a function of temperature (increment 2ºC) for nanogels NG5 and NG14. Bars: 500 µm. 58

Figure 2.2 - Nile blue-labelled nanogels uptake. Effect of NG stiffness on the uptake by a monolayer of hCMEC/D3 polarized cells A) at 37 ºC with incubation times of 15, 30 and 120 minutes and B) at 4 and 37°C with 2 h incubation. Uptake levels NG with same crosslinking content and different sizes C) 37 ºC with incubation times of 15, 30 and 120 minutes and D) at 4 and 37 ºC with 2 h incubation. Represented values are mean ± SD of three experiments with at least 40000 events. Data was analyzed using two-sample t-test and significances are indicated by * for p-value < 0.05, ** for p-value < 0.01, *** for p-value < 0.005 and **** for p-value < 0.0005. 59

Figure 2.3 - Representative confocal microscopy images of hCMEC/D3 cell monolayers interaction with nanogels NG1.5, NG5, NG14 and NG5^{large} after 2 h incubation at 37°C, followed by fixation and F-actin staining. Scale bars are 20 µm. Images were obtained using the same settings. 61

Figure 2.4 - Effect of NG size and stiffness on NG transport across an *in vitro* filter-free BBB model. hCMEC/D3 cell monolayers were incubated with nile

blue-labeled NG1.5, NG5, and NG14 at 37 ºC for (A) 2, (B) 4, and (C) 16 hours, after which fluorescence in the apical, cell, and basal fractions was determined by fluorescence spectroscopy. (D) Percentage of exocytosed nanogel (exocytosed nanogel (%) = $fluorescence_{basolateral}$ x 100/($fluorescence_{cells}$ + $fluorescence_{basolateral}$) after 2 h incubation. (E) Transcytosis levels for NG5 and $NG5^{large}$ after 2, 4 and 16 h incubation. (F) Apparent permeability (P_{app}) of FITC-dextran (MW 4 kDa) in hCMEC/D3 cell monolayers incubated with NG1.5, NG5, NG14 and $NG5^{large}$ for 2, 4 and 16 hours. Control is hCMEC/D3 cell monolayer incubated without nanogel. Values are represented as mean ± SD of four independent experiments and each experiment was performed in duplicate. Data were analyzed using two-sample t-test and statistically significant differences are indicated by * for p-value < 0.05, ** for p-value < 0.01 and *** for p-value < 0.05 64

Figure 2.5 - Nile blue-labelled nanogel-cell interaction in a filter-free *in vitro* BBB model with hCMEC/D3 polarized cells after 2 h incubation of nanogels A) NG1.5, B) NG5 and C) NG14 at 37°C. 3D viewing (left) displays basolateral (top) and apical (bottom) views of nanogels (red) interaction with F-actin (green) from hCMEC/D3 cell layers and collagen gel. Z-stacks were also represented in XZ orthogonal views (right, top) and three-dimension projections (right, bottom). Images were acquired with same system settings. 65

Figure 3.1 – Representation of cell population discrimination in direct co-culture of glioma cells and macrophages by gating fluorescence. C6 (glioma cells) and J774 (macrophages) populations were distinguished by staining the macrophages populations with CellTracker™ Green CMFDA Dye at 2 µmol L^{-1} in DMEM-HG supplemented with 10% (v/v) FBS and GlutamaxTM-I for 40 min at 37°C and gating fluorescence intensity. FITC-A- represents the C6 glioma cells population and FITC-A+, the J774 macrophages population. 79

Figure 3.2 - Effect of NGs stiffness and size on the interaction with monoculture and co-culture of glioma and macrophages cells. NG1.5, NG5 and NG14 (stiffness effect) in A) C6 glioma cells in monoculture and co-culture with J774+ cells and, B) J774+ cells in monoculture and co-culture with C6 glioma cells. NG5 and NG5large (size effect) intracellular fluorescence levels evaluation in C) C6 glioma cells in monoculture and co-culture with J774+ cells and, D) NG5 and NG5large (size effect) intracellular fluorescence levels evaluation in J774+ cells in monoculture and co-culture with C6 glioma cells. C6 and J774+ cells were exposed to 50 µg (100 µg ml^{-1}) of nile-blue labelled nanogels NG1.5, NG5, NG5large and NG14 for 2 h at 37 °C, 5% CO2 and interaction was evaluated by flow cytometry. The intracellular fluorescence intensities were corrected by dividing the mean fluorescence intensity of the cells by the fluorescence intensity of the

NG stock dispersions (100 µg ml^{-1}). Values are represented as mean ± SD of four independent experiments and each experiment was performed in duplicate. Data was analyzed using two-sample t-test and significances are indicated by * for p-value < 0.05, ** for p-value < 0.01 and *** for p-value < 0.001. 81

Figure 3.3 - Evaluation of NGs uptake in monoculture and co-culture of glioma cells and macrophages. Comparison between intracellular fluorescence of nanogels NG1.5, NG5, NG14 and $NG5^{large}$ by C6 cells and J774 CellTracker™ Green CMFDA Dye-stained macrophages in A) mono (C6 and J774+) and B) co-culture (coC6 and coJ774+). 500 µl of a 100 µg ml^{-1} NGs dispersion were incubated for 2 h for uptake assessment. The intracellular fluorescence intensities were corrected by dividing the mean fluorescence intensity of the cells by the fluorescence intensity of the NG stock dispersions (100 µg ml^{-1}). Values are represented as mean ± SD of four independent experiments. Data was analyzed using two-sample t-test and significances are indicated by * for p-value < 0.05, ** for p-value < 0.01 and *** for p-value < 0.001 82

Figure 3.4 – Glioma cells response to p(NIPMAM) NGs stiffnesses and size. Cell viability evaluation by colorimetric MTT viability assay of C6 glioma cells exposed to nanogels with A) different cross-linking density, NG1.5, NG5 and NG14, and B) different sizes, NG5 $NG5^{large}$ for 24 hours at 37 °C, 5% CO_2. C) Toxicity assessment of C6 glioma cells by fluorescence microscopy exposed to 1 mg ml^{-1} of NG1.5, NG5, NG14 and $NG5^{large}$ for 24 hours at 37 °C, 5% CO_2. Nuclei were stained with 2 µg ml^{-1} DAPI for 30 min and images were acquire with and HCX PL FLUOTAR L 40x/0.60 DRY objective. Values are represented as mean ± SD of three independent experiments and each experiment was performed in triplicate. Data was analyzed using two-sample t-test and significances are indicated by * for p-value < 0.05 and *** for p-value < 0.001. Bars: 20 µm. 84

Figure 3.5 - Monocultures response to NGs stiffness. Fluorescence microscopy of monocultures of A) C6 glioma cells and B) J774 macrophages after exposed to NG1.5, NG5, NG14 and $NG5^{large}$ for 24 hours at 1 mg ml^{-1}. Images were acquired with and N PLAN 10x/0.25 DRY objective and nuclei are stained with DAPI. Bars: 20 µm. 85

Figure 3.6 - Fluorescence microscopy of co-culture of C6 glioma cells and J774 macrophages after exposed for 24 h to NG1.5, NG5 and NG14. Nuclei are stained with DAPI and macrophages were stained with CellTracker™ Green CMFDA Dye. NGs were labelled with nile blue, although the fluorescence intensity is not the identical among them, where NG1.5 shows the higher intensity followed by NG5 and NG14. Scale bar: 20 µm. 86

Figure 3.7 – Optical microscopy of monocultures of C6 glioma cells, J774 macrophages and co-culture of C6 and J774 cells after exposed for 24 hours to NG1.5, NG5, NG14 and $NG5^{large}$ in 6-well plates. First row are the cells without exposure to NGs. 87

Figure 3.8 – Crystal formation in the presence of NG5 and NG1.5 nanogels. Optical microscopy of monocultures of C6 glioma cells exposed to 500 µg ml^{-1} of A) NG1.5 and B) NG5 for 24 h and of J774 macrophages 500 µg ml^{-1} of C) NG1.5 and D) NG5 for 24 h. Optical microscopy images of co-culture of C6 and J774 cells after exposed for 24 hours to 1 mg ml^{-1} E) NG1.5 and F) NG5. 88

Figure 3.9 – Confocal images of multinucleated macrophage J774 cell. A) Hoechst staining, B) NGs, C) Lysotracker (lysosomes and late endosome staining) and D) Merge of A, B and C. 89

Figure 3.10 – Intracellular ROS generation by NGs in monoculture and co-culture. A) Evaluation of ROS production by NGs with different stiffness, NG1.5, NG5 and N14 in monoculture of C6 and J774 and co-culture of C6 and J774. B) ROS generation in monoculture and co-culture conditions due to NGs response. Cells were treated for 2 h with 50 µg (100 µg ml^{-1}) at 37 °C, 5% CO_2. Data was analyzed using two-sample t-test and significances are indicated by * for p-value < 0.05, ** for p-value < 0.01 and *** for p-value < 0.001. 90

Figure 4.1 - Representative size distributions of A) PLGA-PTX NCs, B) MCF-7 membrane-coated PLGA-PTX NCs and C) MCF-7 membrane extract. D) PLGA-PTX, mPLGA-PTX and MCF-7 membrane extract zeta potential in 0.1 x PBS (pH 7.4). PLGA-PTX and mPLGA-PTX zeta potential values are represented as mean ± SD of three batches, MCF-7 membrane is representative of one extraction. 105

Figure 4.2 - CryoTEM images of A) PLGA-PTX, B) MCF-7 extracted membranes and C) (MCF-7)-membrane-coated PLGA-PTX measured in 0.1 x PBS (pH 7.4) where scale bars represent 100 nm. Negative staining transmission electron microscopy (TEM) of D) PLGA-PTX NCs and E) mPLGA-PTX NCs where scale bars represent 100 nm. F) Scanning electron microscopy (SEM) image of PLGA-PTX NCs imaged at 2 kV at high vacuum with Inlens detector where scale bar represents 500 nm. 107

Figure 4.3 - FITR spectra of PLGA nanocarriers variations, PLGA and Pluronic®-F127 with 4 cm^{-1} resolution over 128 scans from 4000 to 400 cm^{-1}. 108

Figure 4.4 - Representative HPLC chromatograms of pure paclitaxel at 227 nm in the concentration range from 0.5 to 25 µg ml^{-1}. 109

Figure 4.5 - Cellular uptake comparison between PLGA-Curcumin NCs and mPLGA-Curcumin NCs by A) MCF-7 breast cancer cells incubated for 2, 4 and 24 hours B) A549 lung cancer cells incubated for 2 and 4 hours and C) MCF-10A non-tumorigenic breast cells incubated for 4 hours. Measurements are average ± SE of three independent experiments. Data was analyzed by analysis of variance (ANOVA) and Tukey's test. Significances are indicated with * for p-value < 0.05, ** for p-value < 0.01 and *** for p-value < 0.001. 111

Figure 4.6 - Effect of MCF-7 membrane coating of PLGA NCs in cellular uptake. A) Cellular uptake and B) percentage of cells positive for curcumin-loaded PLGA NCs coated with MCF-7 membrane (mPLGA) and non-coated (PLGA) after 4 hours incubation with MCF-7, A549 and MCF-10A cells at 37 °C in atmosphere with 5% CO_2. Measurements are average ± SE of three independent experiments. Data was analyzed by ANOVA and Tukey's test. Significances are indicated with * for p-value < 0.05, ** for p-value < 0.01 and *** for p-value < 0.001. 112

Figure 4.7 - Confocal laser scanning images of MCF-7 and MCF-10A cells treated with coated and non-coated PLGA-Fluorescein NCs for 4 hours. Cell were imaged with a 63x oil-immersion objective and acquired in z-stacks at 0.2 µm intervals. Images were acquired with the same system and laser settings. 113

Figure 4.8 - Cellular viability of A) MCF-7, B) A549 and C) MCF-10A after 48 h incubation with different concentrations of mPLGA-PTX and PLGA-PTX NCs evaluated by MTT viability assay. Data was analyzed using using two-sample t-test and significances are indicated. Significances are indicated by ** for p-value < 0.01. 115

Figure 5.1 - Schematic representation of the mode of operation of on demand release from liposome loaded with molecular motors inside by bilayer. The unidirectional molecular rotation disturbs the bilayer and thereby facilitates release of stored molecular components, here calcein as a model compound. 123

Figure 5.2 - Dynamic Light Scattering of (Δ9-cis)PC liposomes without MM (no MM), and with MM at mixing ratio 1:50 (MM1) and 2:25 (MM2) after purification with Sephadex® G100. Size control was induced via extrusion through a polycarbonate filter (pore-size 100 nm) and the measurements were performed at 20°C. 126

Figure 5.3 - The zeta (ζ)-potential of (Δ9-cis)PC liposomes without MM (no MM), and with MM at mixing ratio 1:50 (MM1) and 2:25 (MM2) after purification with Sephadex® G100. ζ-potential values are mean ± SD of

three measurements of the same batch. Data was analyzed using two-sample t-test and significance is indicated by * for p-value < 0.05. 127

Figure 5.4 - Liposomes without and with MM (1:50) without irradiation (A) and with irradiation for 30 seconds (B) of which the calcein release was studied using fluorescence spectroscopy. Measurements are average ± SD of three independent experiments. 129

Figure 5.5 - Liposomes without and with MM (1:50) with irradiation for 30 seconds of which the calcein release was studied at fixed time-points using fluorescence spectroscopy. Measurements are average ± SE of three independent experiments. Data was analyzed by analysis of variance (ANOVA) and Tukey's test. Significances are indicated with * for p-value < 0.05, ** for p-value < 0.01 and *** for p-value < 0.001. 130

Figure 5.6 - Liposomes with MM (1:50) without irradiation and with irradiation for 30 and 60 seconds of which the calcein release was studied using fluorescence spectroscopy. 131

Figure S1 - Hydrodynamic diameter of p(NIPMAM) nanogels with 5 mol% BIS in ddH_2O synthesized in the presence of 1.6, 2.2 and 2.6 mM of SDS with polymerization time above 6 hours. 152

Figure S2 - P(NIPMAM) nanogels (5 mol% BIS) hydrodynamic diameter as function of polymerization time Values represented are mean ± SD of 3 measurements from the same batch. 152

Figure S3 - A) Fluorescence of Nile blue in p(NIPMAM) nanogels in EMB-2 complete medium at 100 µg ml^{-1} with excitation at 633 nm and emission was record from 645 to 1000 nm, and B) flow cytometry histogram profiles of hCMEC/D3 cells after nanogels incubation for 2 hours at 37ºC using the APC channel (670/30 band pass filter) and laser excitation 640 nm. 153

Figure S4 - A) PDMS mold after plasma treatment, B) hCMEC/D3 polarized layer on collagen gel after PDMS mold removal and C) schematic representation of PDMS mold containing collagen gel and hCMEC/D3 cell layer. 155

Figure S1 - HPLC chromatograms for evaluation of matrix influence for the determination of encapsulation efficiency of paclitaxel in PLGA NCs. 157

Figure S2 - Confocal laser scanning images of MCF-7 and MCF-10A cells treated with coated and non-coated PLGA-NLR NCs for 4 hours. Cell were imaged with a 63x oil-immersion objective and acquired in z-stacks at 0.4 µm intervals, 512 x 512 pixels. 158

LIST OF TABLES

Table 1.1 - Literature reports evaluating cell-(spherical)NPs interaction and described NPs properties. [a]Indication of stiffness reported as bulk material. [b]Indication of stiffness reported as Young's modulus. Evaluated cell types are indicated by (I) cancer cells, (II) macrophages and (III) endothelial cells. 35

Table 2.1 - Synthesis conditions to obtain p(NIPMAM) nanogels with different cross-linking densities, sizes and monodisperse populations. All reactions were performed at 70°C in oil bath. 51

Table 2.2 - p(NIPMAM) nanogel properties. [1]Number of particles measured from TEM images to estimate nanogel size. [2] PdI was recalculated according to a single peak. 3 For NG1.5 we report 57

Table 4.1 - Z-average, PdI (polydispersity index) and ζ-potential of PLGA-PTX (n=3), mPLGA-PTX (n=3) and MCF-7 (n=1) membrane extract were measured in 0.1x PBS. NTA size values are the mean of 2 different batches for PLGA-PTX and mPLGA-PTX NCs as well as particles concentration. MCF-7 membrane is representative of one extraction. 106

Table 4.2 - Regression parameters for weighted regressions of the analytical curve ($y = ax + b$) where ω_i is the weight tested for the calibration with ω_i = 1 representing the unweighted regression and ΣER(%) respective sums of the relative errors (n=4). 110

Table 4.3 - Analytical parameters for the HPLC method using UV/ Vis detector at 227 nm and 30 °C. 110

Table S1 - APC positive populations frequency for nile blue-labelled nanogels with different cross-linking densities. 154

LIST OF ABREVIATIONS ANS ACRONYMS

(∆9-cis)PC	1,2-dioleoyl-sn-glycero-3-phosphocholine
APS	ammonium persulfate
BBB	blood-brain barrier
BIS	N,N′-methylenebis(acrylamide)
CLSM	confocal laser scanning microscopy
CryoTEM	cryogenic transmission electron microscopy
CV%	percent coefficient of variation
ddH_2O	double-distilled water
DEA-HEMA	(N,N-Diethyl acrylamide)-(2-hydroxyethyl methacrylate)
DextS/PLArg	dextran sulfate sodium salt/poly-L-arginine hydrochloride
DLS	dynamic light scattering
DMEM	Dulbecco's modified eagle medium
DMSO	dimethyl sulfoxide
DOPC	1,2-dioleoyl-sn-glycero-3-phosphocholine
EBM-2	endothelial basal medium 2
EDTA	ethylenediamine tetraacetic acid
EE	encapsulation efficiency
EGF	epidermal growth factor
EMEA	European medicines agency
EpCAM	epithelial cell adhesion molecule

EPON	epoxy embedding medium
EPR	permeability and retention effect
FBS	fetal bovine serum
FDA	food and drug administration
FE-SEM	field-emission scanning electron microscopy
Fiji	Fiji is just ImageJ
FITC	fluorescein isothiocyanate
FTIR	Fourier-transform infrared spectroscopy
HBSS	Hank's balanced salt solution
HEMA	2-hydroxyethyl methacrylate
HPLC	high-performance liquid chromatography
HS	horse serum
ICAM-1	intercellular adhesion molecule 1
LbL	layer-by-layer
LCST	lower critical solution temperature
LMVs	large multilamellar vesicles
LOQ	quantification limit
MEBM	mammary epithelial cell growth basal medium
MEGMTM	mammary epithelial cell growth medium singlequots^{tm} kit
MM	molecular motors
MTT	3-(4,5-dimethylthiazol-2-yl)-2,5-diphenyltetrazolium bromide

MW	molecular weight
NC	nanocarrier
NG	nanogel
NIPMAM	N-isopropylmethacrylamide
NLB	nile blue acrylamide
NLR	nile red
NPs	nanoparticles
NTA	nanoparticle tracking analysis
OCL	PEG-polycaprolactone
p(NIPMAM)	poly-N-isopropylmethacrylamide
PBS	phosphate-buffered saline
PDMS	polydimethylsiloxane
PFA	paraformaldehyde
PLGA	poly lactic-co-glycolic acid
PSS/PAH	poly(sodium 4-styrenesulfonate)/poly(allylamine hydrochloride)
PTX	paclitaxel
PVA	polyvinyl alcohol
SD	standard deviation
SDS	sodium dodecyl sulfate
SEM	scanning electron microscopy
SUVs	smaller and unilamellar vesicles
TA/PVPON	tannic acid/poly(N-vinylpyrrolidone)

TAMs	tumor-associated macrophages
TEM	transmission electron microscopy
Tf	transferrin
TfR	transferrin receptor
UV	ultraviolet-visible
VPTT	volume phase transition temperature

LIST OF SYMBOLS

σ	standard deviation of linear coefficient
A	absorbance
$\mathbf{P_{app}}$	apparent permeability
$\mathbf{R^2}$	correlation coefficient
$\mathbf{C_0}$	initial concentration
$\mathbf{\Delta Q/\Delta t}$	rate of permeation
$\mathbf{\sum ER}$	respective sums of the relative errors
α	slope
λ	wavelength
ω_i	weight tested for the calibration
ζ	zeta potential

CONTENTS

1 INTRODUCTION 33

1.1 SOFT NANOPARTICLES 33

1.1.1 Nanogels 34

1.1.2 Biodegradable polymeric nanoparticles 38

1.1.3 Liposomes 39

1.2 BIOLOGICAL MICROENVIRONMENTS AND BARRIERS 41

1.2.1 Blood-brain barrier and *in-vitro* blood-brain barrier models 41

1.2.2 Tumor microenvironment 44

2 CHAPTER II: LOW STIFFNESS FAVORS NANOGEL TRANSCYTOSIS ACROSS THE BLOOD-BRAIN BARRIER 47

2.1 INTRODUCTION 49

2.2 METHODS AND MATERIALS 51

2.2.1 Nanogel synthesis 51

2.2.2 Nanogel characterization 52

2.2.3 Brain endothelial cell culture 53

2.2.4 Transcytosis assay 53

2.2.5 Flow cytometry assessment of nanogel uptake in polarized brain endothelial cell monolayers 54

2.2.6 Confocal microscopy of nanogels in polarized brain endothelial cell monolayers 55

2.3 RESULTS 56

2.3.1 Nanogel characterization 56

2.3.2 High nanogel stiffness favors uptake by polarized brain endothelial cell monolayers 58

2.3.3 Low nanogel stiffness favors transcytosis across polarized brain endothelial cell monolayers 62

2.4 CONCLUSION 66

3 CHAPTER III: ASSESSMENT OF NANOGELS STIFFNESS EFFECT ON DIRECT CO-CULTURE OF GLIOMA CELLS AND MACROPHAGES. 69

3.1 INTRODUCTION 73

3.2 METHODS AND MATERIALS 74

3.2.1 Nanogel preparation and characterization 74

3.2.2 Cell culture 75

3.2.3 Flow cytometry 75

3.2.4 Cell viability assay 76

3.2.5 Fluorescence microscopy 77

3.2.6 Confocal microscopy 77

3.3 RESULTS AND DISCUSSION 78

3.3.1 Nanogel characterization 78

3.3.2 Direct co-culture 78

3.3.3 *In vitro* cellular uptake of nanogels in monoculture and co-culture 79

3.3.3 Nanogels stiffness has an impact on cell viability 83

3.4 CONCLUSION 91

4 CHAPTER IV: EPITHELIAL CANCER-CELL MEMBRANE COATED PLGA NANOCARRIERS ENHANCED UPTAKE LEADS TO MORE EFFECTIVE CANCER TREATMENT 93

4.1 INTRODUCTION 95

4.2 MATERIALS AND METHODS 96

4.2.1 Preparation of PTX-loaded and dye-loaded PLGA nanocarriers 96

4.2.2 Cell lines and cell culture 97
4.2.3 Cell membrane isolation 97
4.2.4 PLGA-PTX and PLGA-dye NCs coating with MCF-7 cells membrane extract 98
4.2.5 Transmission electron microscopy and cryogenic transmission electron microscopy 98
4.2.6 Scanning electron microscopy (SEM) 99
4.2.7 Fourier-transform infrared spectroscopy (FTIR) 99
4.2.8 High-performance liquid chromatography (HPLC) for paclitaxel quantification 99
4.2.9 Cellular uptake studies by flow cytometry 102
4.2.10 Confocal laser scanning microscopy 102
4.2.11 Cell viability 103
4.3 RESULTS 105
4.3.1 PLGA-PTX NCS and mPLGA-PTX NCs characterization 105
4.4.2 Encapsulation efficiency of paclitaxel in PLGA NCs 109
4.4.3 (MCF-7)-membrane-coated PLGA NCs preferential cellular uptake 111
4.3.4 In vitro evaluation of (MCF-7)-membrane coated PLGA-PTX NCs against epithelial cell types 114
4.5 DISCUSSION 115
4.6 CONCLUSIONS 117
5 CHAPTER V: LIGHT-INDUCED MOLECULAR ROTATION TRIGGERS ON-DEMAND RELEASE IN LIPOSOMES 119
5.1 INTRODUCTION 121
5.2 MATERIALS AND METHODS 124
5.2.1 Liposome preparation 124
5.2.2 Liposomes characterization 125

5.3 RESULTS 125

5.4 CONCLUSION 131

REFERENCES 133

APPENDICES 151

Appendix A – Supporting Information: Low nanogel stiffness favors nanogel transcytosis across the blood-brain barrier 151

Appendix B – Supporting Information 157

1 INTRODUCTION

The use of nanotechnology in medicine is rapidly developing and leading to the advancement on how we treat and diagnose several diseases.[1] However, with the application of nanomaterials in medicine also comes the need for understanding their interaction with biological systems, not only for allowing better tunable nanomaterials properties, but also for their safe application. Nanomaterials have been employed to various purposes e.g., drug delivery,[2-5] theranostic nanomedicine,[6-8] antibacterial platforms[9-12] and diagnostic technique as imaging[13-15] and biosensing.[16-18] Nanomaterials are often categorized according to their physical-chemical properties like size, surface charge, surface chemistry, shape and composition. Tailoring each of these properties affects how nanoparticles (NPs) interact with each cell type and ultimately affects how they are distributed *in vivo* and how do they act in the biological system. Before reaching their intended end target, NPs must overcome a number of biological barriers from biodistribution and immune-response to internalization and vesicular trafficking.[19-21] This thesis contains four experimental chapters in which the interaction between nanomaterials and cells is investigated. We also propose a new nano-delivery system with controllable properties.

1.1 SOFT NANOPARTICLES

Nanoparticles formulations are mainly composed of organic or inorganic elements, or a combination of them (hybrid materials). Inorganic NPs are usually hard particles including metallic NPs, quantum dots - usually made of semiconductor materials- silica NPs, etc. Organic NPs, however, are soft nanomaterials such as the polymeric NPs, DNA NPs, dendrimer NPs, liposomes, polymersomes and micelles. Here we focus on soft nanoparticles, in particular, biodegradable polymeric NPs, nanogels and liposomes.

1.1.1 Nanogels

Nanogels (NGs) and microgels are an important example of soft particles. Composed of a polymeric network, the NGs are deformable and capable of changing between collapsed and swollen states triggered by an external stimulus, e.g., pH- and thermo-induced collapsed. When collapsed, NGs stiffness increases and they behave similar to a hard particle. In the swollen state, nanogels became softer under good solvent conditions, in which solvent can account for about 85% of the nanogel volume.[22-23] Acrylamide-based nanogels are thermoresponsive nanoparticles that switch between collapsed and swollen state by increasing or decreasing the temperature of the dispersion. Above the volume phase transition temperature (VPTT) or lower critical solution temperature (LCST), nanogels are collapsed and below it, swollen. Different polyacrylamides exhibit a VPTT-transition, for example, poly(N-isopropylacrylamide) (p(NIPAM)) has a VPTT at 32 °C while for poly(N-isopropylmethacrylamide) (p(NIPMAM)), VPTT is at 44 °C. The swollen state of nanogels is thermodynamically stable and kept by hydrogen-bonds between polymer and solvent.[24]

The deformable nature of the nanogels and ability to cross through pores with a diameter smaller than the nanogels diameter at their swollen state is remarkable. Such capability can be tuned by changing cross-linking density or temperature of reaction. NGs can be synthesized by one-pot precipitation polymerization where cross-linking density and temperature of reaction can be well controlled. Still, their size can be controlled by the addition of a surfactant or by changes in the polymerization time.[25]

Chapters II and III evaluate *in vitro* the ability of nanogels of different stiffnesses to cross the blood-brain barrier (BBB) as well as their internalization by macrophages and glioma cells, and their toxic effect in monocultures and coculture of macrophages and glioma cells. A compilation with the main studies assessing particle stiffness effect on cells can be seen in Table 1.1.

Table 1.1 - Literature reports evaluating cell-(spherical)NPs interaction and described NPs properties. [a]Indication of stiffness reported as bulk material. [b]Indication of stiffness reported as Young's modulus. Evaluated cell types are indicated by (I) cancer cells, (II) macrophages and (III) endothelial cells.

Particle	Size	Mechanical properties	Effects of stiffness	References
PEG hydrogel spheres	200 nm	10 – 3000 kPa[a]	(I), (II) and (III) favor uptake of stiffer particles (*in vitro*). Longer circulation by softer particles, although more significant at short times (30 min, in vivo).	26
PLGA-lipid (core-shell) NPs	100 nm	Values not specified	(I) and (III) favor uptake of stiffer particles (*in vitro*).	27
pCB-AuNPs NGs	250 nm	0.18-1.35 MPa[b]	Increased blood half-life for softer NPs and lower splenic accumulation (*in vivo).*	28
PLGA-lipid (core-shell) and PLGA-water-lipid (core-water layer spheres	40 nm	0.76 – 1.20 GPa[b]	(I), (III) favor uptake of stiffer particles. Clathrin-mediated endocytosis is indicated for particle internalization independent of stiffness (*in vitro*).	29
Hyaluronic acid capsules	2.4 μm	7.5 – 27.2 N/m	(I) favors internalization of softer particles (*in vitro*).	30
(DextS/PLArg) and (PSS/PAH) LbL capsules	4.1 - 4.7 μm	0.25 – 5 N/m	In (I), (II) and (III) softer particles were transported faster to the lysosomes (*in vitro*).	31

HEMA hydrogel spheres	900 - 1300 nm	16.7 – 155.7 kPa[a]	(I) favors internalization of softer particles. Energy-dependent endocytosis is indicated. Softer particles: internalization mainly by macropinocytosis. Stiffer particles: caveolae- and clathrin-mediated endocytosis and macropinocytosis (*in vitro*).	32
(TA/PVPON) LbL capsules and spheres	2 µm	4.30 – 1x10^4 MPa[b]	(I), (II) and(III) favor uptake of stiffer particles (*in vitro*)	33
Polyacrylamide spheres	1 - 6 µm	3-fold higher Young's modulus	(III) favors uptake of stiffer particles	34
Polypeptide (PGA) templated capsules	800 nm	2.5 – 22.5 kPa[b]	In human peripheral blood mononuclear cells, stiffer particles show increased activation of (CD83+/CD40+) (*in vitro*).	35
PLGA-lipid (core-shell) spheres	50 - 160 nm	50- 110 MPa[b]	Particles of moderate rigidity show superior diffusivity through mucus than both their soft and hard counterpart (2D and 3D *in vitro* and *in vivo*).	36
DEA-HEMA hydrogel spheres	150 - 170 nm	18 – 211 kPa[b]	(II) favors uptake of particles of intermediate elasticity, that are internalized via	37

			multiple mechanisms (*in vitro*). Soft particles: internalization preferentially by micropinocytosis (*in vitro*) Stiffer particles: involve clathrin-mediated routes (*in vitro*).	
DOPC NLGs	160 nm	45-1.9x10^4 kPa[b]	(I) favors internalization of softer particles (*in vitro*). Soft NLGs uptake was not affect by endocytosis inhibitors in (I) (*in vitro*). Stiffer NLGs uptake by (I) was affected when cells were incubated with Dynasore and Chlorpromazine but not Fillipin (*in vitro*). Soft NLGs show more accumulation in tumors (*in vivo*). Stiffer NLGs accumulate preferentially in the liver (*in vivo*).	[38]

PEG - polyethylene glycol
PLGA - poly(D, L-lactic-co-glycolic acid)
DextS/PLArg - dextran sulfate sodium salt/poly-L-arginine hydrochloride
PSS/PAH - poly(sodium 4-styrenesulfonate)/poly(allylamine hydrochloride)
HEMA - 2-hydroxyethyl methacrylate
TA/PVPON - tannic acid/poly(N-vinylpyrrolidone)
LbL - layer-by-layer
OCL - PEG-polycaprolactone
DEA-HEMA – (N,N-Diethyl acrylamide)-(2-hydroxyethyl methacrylate)
DOPC - 1,2-dioleoyl-sn-glycero-3-phosphocholine
Source: By the author.

The studies reported in Table 1.1 demonstrate that NP stiffness plays an important role in NPs-cell interactions but also show the possible influence of NP size and surface chemistry on the processes. Some theoretical models describe the interaction between elastic particles and cellular membranes.[39-40] Particularly interesting is the Lagrangian-Eulerian description that Li *et al*.[39] employed to explore a nanocapsule interaction with a cellular membrane. They suggest that the Eulerian description is more

suitable to simulate the cellular deformation, which can be attributed to simplicity since the Lagrangian approach would require a mapping of the material configuration, which is avoided by the Eulerian approach.[41] The particle elasticity however, is approached by the Lagrangian formalism. They argue that the wrapping phase is highly dependent of particle size, adhesion energy and bending rigidity ratio between the particle and membrane, meaning that the rise in elastic energy that is required to achieve full wrapping of the particle and thus its internalization, is affected by particle stiffness. For nanocapsules and vesicles with the same bending rigidity a higher elastic energy change was required for the uptake of the nanocapsules, which implies that nanocapsules full wrapping is more demanding.

1.1.2 Biodegradable polymeric nanoparticles

Biodegradable polymeric nanoparticles have enormous potential as drug delivery systems. According to the synthesis process, these NPs can result in different capsular structures: liquid core, polymeric core or as an active substance in molecular dispersion. Composed of aggregated polymers, this latter structure may contain a substance, such as a drug, distributed in a polymeric matrix, while the other cited structures store the compound in a liquid or polymeric cavity surrounded by a polymeric membrane.[42] Therapeutic compounds can be entrapped in polymeric NCs by binding the compound to the polymer or monomer, or by physical entrapment. The method for physical entrapment of therapeutics agents by polymers nanostructures will depend mainly on the compound hydrophobicity. Hydrophobic molecules entrapment is typically more efficient when compared to hydrophilic molecules, although drug loading is still not ideal and usually less than 5 wt% (i.e., weight % of the transported drug versus the carrier material). Still, the NPs offer a good system to protect the drug against degradation, being also capable of sustained or controlled release and improved bioavailability, compared to free molecules.

Poly (D,L-lactic-co-glycolic acid) (PLGA) is a biodegradable, biocompatible copolymer, approved by the Food and Drug Administration (FDA) and sensitive to pH variations.[43] PLGA is also a versatile copolymer that can be synthesized in different

proportions of lactic and glycolic acid, which leads to different properties such as solubility and glass transition temperature, affecting its degradation time.[44-45] Among several techniques to physically entrap drug in PLGA NPs, nanoprecipitation and emulsion-based techniques are widely employed. Developed by Fessi *et al*.[46] nanoprecipitation is an easily reproducible and simple method, commonly used in the encapsulation of hydrophobic molecules.[47] Also known as the solvent displacement method, the formation of NPs is based on the displacement of a semi-polar solvent, such as acetone, ethyl acetate or dimethyl sulfoxide (DMSO), from an organic phase to an aqueous phase in which the solvent is miscible. To prevent aggregation, it is common for the aqueous phase to contain a surfactant such as poloxamer, polyvinyl alcohol (PVA) and Tween®80. The displacement of the solvent can be explained by the Gibbs-Marangoni effect, which describes the movement of a liquid of higher surface tension to a liquid of lower surface tension in the presence of a stress gradient.[48]

In Chapter IV, we describe the development of a paclitaxel-loaded PLGA NP coated with breast cancer MCF-7 cells membrane in which we take advantage of the homotypic adhesion between cancer cells to improve their therapeutic effect and specificity.

1.1.3 Liposomes

Liposomes were one of the first nanoscale systems to be proposed for the delivery and controlled release of therapeutic agents. Their biocompatibility and lack of toxicity are important characteristics for delivery systems and motivate their use in clinical applications. Liposomes are composed of one or more lipid bilayers and contain an aqueous hydrophilic core. The formation of the liposomal structures occurs due to the amphiphilic nature of the phospholipids (hydrophilic head group linked to a hydrophobic tail). Not only hydrophilic but also hydrophobic molecules can be incorporated into liposomes. Water-soluble molecules are loaded in the aqueous core while hydrophobic molecules are associated to the lipid bilayer due to interaction with the hydrophobic chains of the phospholipids.[49- 50]

Lipid thin-film hydration is a well-known method to prepare large multilamellar vesicles (LMVs) from which smaller and unillamellar vesicles (SUVs) can be produced by extrusion or sonication. By employing thin-film hydration method, a hydrophobic compound can be associated within the lipid bilayer by simply mixing it with the lipid solution and drying to a thin film. Water-soluble molecules, can be added to the aqueous solution, typically a buffer solution, that is used to hydrate the lipid film.[50] The drug release from plain liposomes is dependent on their interaction with cells and can occur after endocytosis, fusion with the cell membrane and adsorption to the cell wall. Even though liposomes can improve drug delivery, there is still a need to better control the release of the drugs.

Stimuli-responsive liposomes can be engineered to respond to specific external triggers, e.g. temperature,[51-53] ultrasound[54-56] and light,[57-59] or to triggers that are intrinsic to the organism, e.g. pH,[60-61] and redox potential.[62-64] Intrinsic factors may vary between patients and diseased sites. External triggers, in contrast, offer better control over the system. Light-responsive systems respond to an external irradiation source in the ultraviolet (UV), visible (Vis) or near-infrared (NIR) spectral regions. The main strategy to obtain photo-responsive liposomes is the insertion of a photoreactive group, where trigger mechanisms are photo-thermal,[65-66] photopolymerization,[67] photo-oxidation,[57] photocleavage,[68-69] and photo-isomerization.[70- 73] Most systems release the drugs upon the burst or destruction of the system, except for the ones based on photo-isomerization.[74]

Photoisomerization of light-driven molecular motors induces a shift to a nonequilibrium state, leading to a rotary motion with spatial-temporal precision,[75-76] In Chapter V, we demonstrate that UV-induced rotation of hydrophobic synthetic molecular motors that are stored inside the lipid membrane of liposomes, disrupts the membrane to such an extent that small molecules (calcein) are released, generating controlled drug release from liposomes through reversible membrane destabilization upon UV irradiation of the molecular motors.

1.2 BIOLOGICAL MICROENVIRONMENTS AND BARRIERS

1.2.1 Blood-brain barrier and *in-vitro* blood-brain barrier models

The blood-brain barrier (BBB) is a collection of specialized blood vessels that separate the vascular system from the brain parenchyma. The BBB is composed of a layer of polarized cerebral microvascular endothelial cells that regulate the transport of molecules across this barrier. Large molecules (> 500 Da) are unable to permeate the polarized cerebral microvascular endothelial cells, hampering the delivery of therapeutic compounds to the brain. Drug delivery to the brain can occur via diffusion across cell membranes, paracellular transport, transport proteins, and transcytosis. Diffusion (of lipid-soluble compounds) is largely limited by the presence of drug efflux pumps, while paracellular transport (of water-soluble compounds) is essentially limited to small molecular transport.[20] Transcytosis is a transcellular vesicular transport pathway from blood to brain and vice versa, which allows for the transport of bigger molecules and particles. The process essentially involves endocytosis, followed by intracellular vesicular transport and, exocytosis at the opposite side of the BBB. Figure 1.1A shows a diagram of the blood-brain barrier cross-section. and Figure 1.1B shows a diagram of the main transport pathways across the BBB. NPs are transported mainly by carrier-mediated transcytosis, receptor – mediated transcytosis, adsorptive transcytosis and diffusion. Diffusion is a mechanism used by small gold nanoparticles.[77-78] Adsorptive transcytosis is often induced by cationic NPs through electrostatic interaction with the negatively charged endothelial cell membranes.[79-81] Carrier-mediated transport of NPs exploit affinity to transport proteins like the glucose transporter.[82] Finally, ligand-conjugated NPs are widely used to target the receptor-mediated transcytosis pathway, including targeting to the transferrin receptor (TfR), insulin receptor, LDL receptor, and GM1.[4,20,83-86] Nevertheless, NP affinity to a cell surface receptor promotes internalization by the endothelial cells, but does not guarantee its transcytosis. High-affinity antibodies for TfR were shown to display less transcytosis than lower- affinity antibodies because the antibodies with higher affinity remained associated to the TfR.[87] Therefore, in order to exploit the process of transcytosis for NP-mediated drug delivery across the BBB not

only the receptor-mediated internalization, but also the subsequent vesicular trafficking and exocytosis of NPs should be taken into consideration. In Chapter II, NPs with different mechanical properties and sizes are examined in relation to uptake and transcytosis at the BBB.

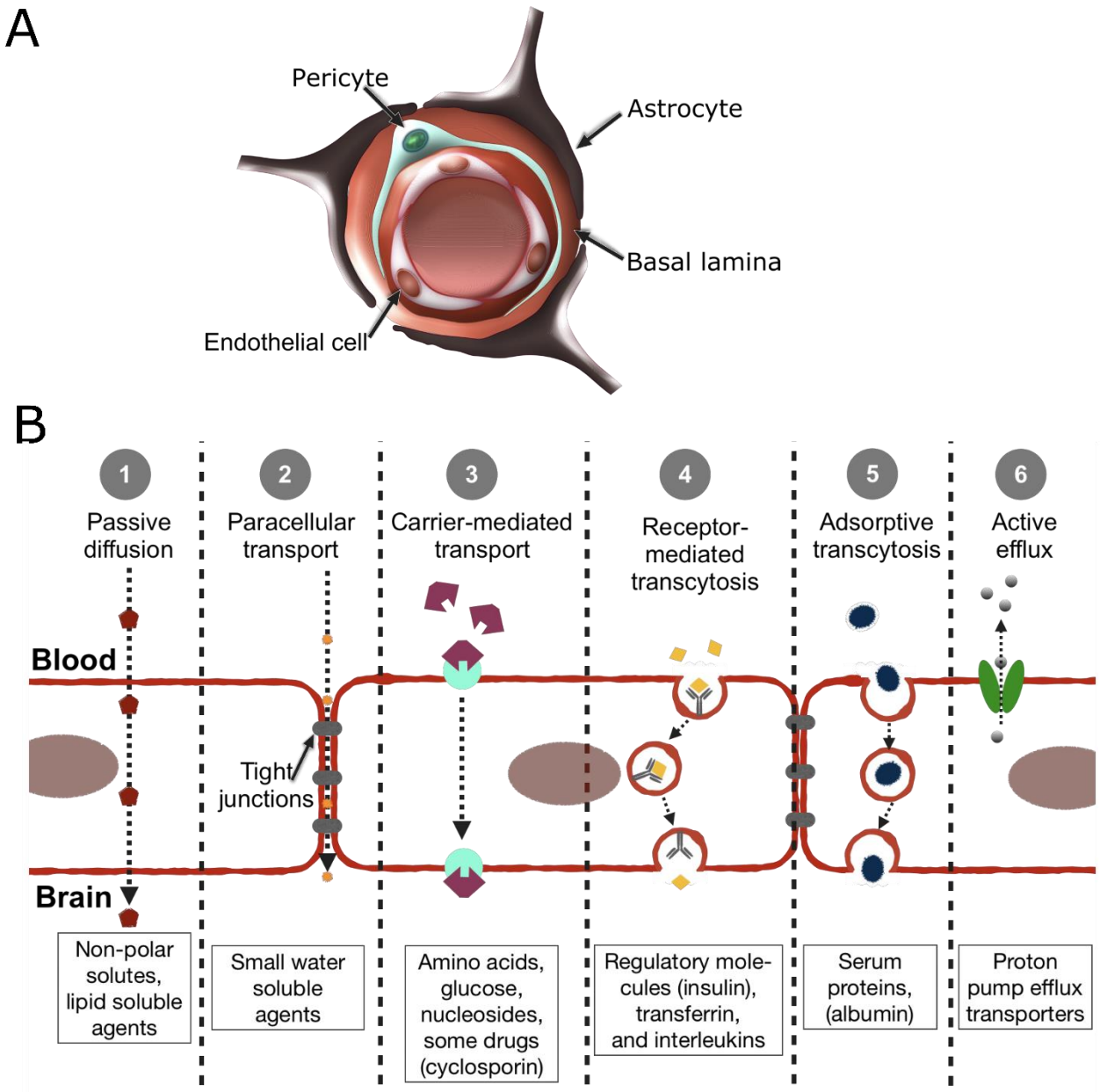

Figure 1.1 – Schematic representation of the blood-brain barrier and main transport systems. A) Cross-sectional view of a cerebral capillary of the blood-brain barrier. B) Diagram of mechanisms of transport across the blood-brain barrier.

Source: By the author.

In vitro blood-brain barrier models

Several *in-vitro* BBB models have been developed and employed to study the transport of nanosized systems as well as macromolecules and small molecules through the BBB. Those models include monolayer models,[84,88] microfluidic models,[89-91] three-dimensional (3D) organoids,[92] and 3D templated models.[93-94] A proper model should contain restrictive tight junctions and low permeability through paracellular transport. Occludin, claudins, and junctional adhesion molecules are the main providers of structural integrity and polarization of endothelial cells.[95-96] Paracellular permeability can be investigated by using a paracellular marker such as lucifer yellow, fluorophore-labeled dextran and mannitol. The most well-known BBB model uses ECM-coated porous membranes (in Transwell® inserts) with a monolayer of brain microvascular endothelial cells grown on top (Figure 1.2).

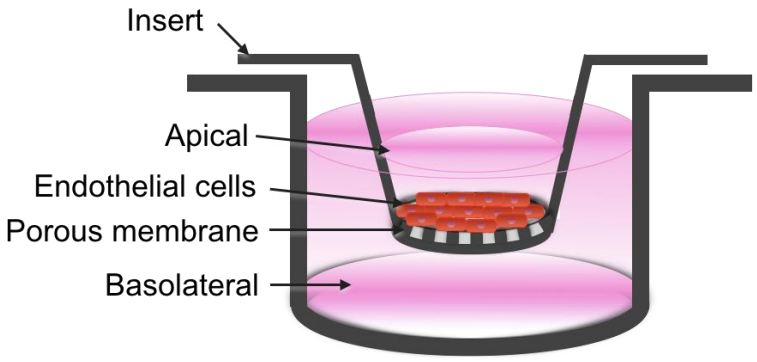

Figure 1.2 – Schematic representation of a typical *in vitro* blood-brain barrier model using a Transwell® insert. Endothelial cells are seeded on an ECM-coated porous membrane and grown to form a polarized monolayer of endothelial cells.
Source: By the author.

Not only Transwell® systems but also most microfluidic systems employ the filter-based approach to mimic the BBB. However, Ye *et al*.[97] showed that particle agglomeration may hinder NP transport through the filter pores. Considering this limitation, we used a filter-free BBB model, recently developed by De Jong *et al*.,[84] in the studies described in this thesis of which the simplified procedure is presented in Figure 1.3. Essentially, a monolayer of human brain microvascular endothelial cells (hCMEC/D3) is grown on a

collagen gel for 5 days. The medium at the apical side of the hCMEC/D3 cell monolayer is carefully removed and replaced with medium containing fluorescently-labeled nanomaterials. After an incubation period, the apical medium is collected, and cells are separated from the basolateral fraction (collagen gel) by incubation with collagenase A for 90 min at 37°C, 5% CO_2, and collected by centrifugation. After centrifugation, the supernatant is separated from the cells and represents the basolateral compartment. Finally, cells are lysed by soaking the pellet in ultrapure water. Then, the apical, cell, and basolateral fractions are transferred to a black flat-bottom 96-wells plate and fluorescence is measured using a plate reader by fluorescence spectroscopy.

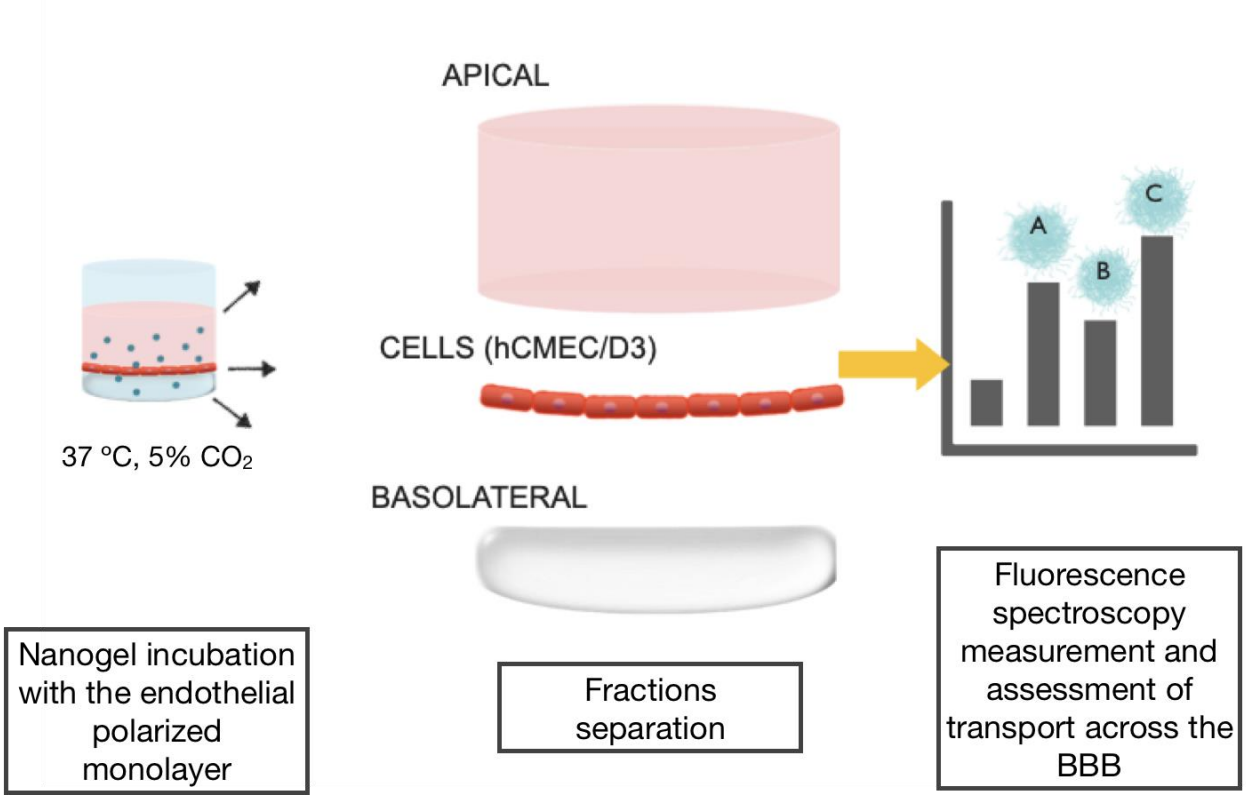

Figure 1.3 – Simplified representation of the quantification of NP transport in the filter-free BBB model. hCMEC/D3 cells are grown for 5 days on top of a collagen gel until they form a polarized cell monolayer that shows restrictive permeability. Then nanomaterials are applied on top of the monolayer. Following incubation, the apical, cellular and basolateral fractions are separated using collagenase A treatment and centrifugation. Each fraction is collected and transendothelial delivery is evaluated by fluorescence spectroscopy.
Source: By the author.

1.2.2 Tumor microenvironment

A pivotal area of research involves the development of cancer therapies that are more effective in killing cancer cells while being less harmful to non-malignant cells, as this will prevent the short-term and long-term side effects of current cancer treatment. Among the most promising alternatives, nanosized delivery systems stand out. Some advantages of nanodelivery systems are: they are non-invasive, show lower toxicity compared to the free therapeutic agents like chemotherapeutics but do not compromise efficacy, protect the therapeutics from degradation, can promote longer circulation, increase therapeutic agent half-life, reduce immunogenicity, can be tailored to cross biological barriers, and enhance accumulation at specific sites.[98-104] However, still a lot is yet to be explored and understood about how the nanosized delivery systems interact with the tumor microenvironment (TME) and how such information can be applied to further improve the efficacy, specificity, and suitability of those systems.

Tumor cells and their microenvironment show many features that are different from normal cells. Nanomaterials for cancer treatment and diagnosis often try to exploit the characteristics of the microenvironment to improve efficacy and specificity, and to control release kinetics of stored drugs. A limiting factor for the current methods is the inability of nanomaterials to completely distinguish between normal and cancer cells, which causes side effects even though these are reduced compared to free agents. Deregulated gene expression is an inherent characteristic in cancer cells that leads to uncontrolled cell growth and proliferation.[105-106] Cancer progression is also greatly influenced by the interaction of the cancer cells with their surroundings, including the extracellular matrix (ECM), blood vessels, associated macrophages, and associated fibroblasts. In addition, the abnormal and dynamic cell adhesion behavior of cancer cells affects tumor progression and can lead to the detachment of cancer cells from the primary tumor followed by their adhesion on secondary sites, configuring metastasis.[107] Inventively, the observed increased homotypic cell adhesion between cancer cells can be exploited to target NPs to the cancer by coating the NP surface with cancer cell-membrane extracts instigating the adhesion of NPs to the cancer cells.[108-109] In Chapter IV, we report the development of a cancer cell membrane-coated polymeric drug delivery system for cancer treatment that shows homotypic interaction with the source

cell (MCF-7, breast cancer) and interaction between the cancer cell membrane-coated NPs and lung cancer (A549) cells and non-tumorigenic breast cells (MCF-10A).

Another characteristic of the tumor microenvironment (TME) is the presence of other associated cell types, e.g. fibroblasts and macrophages. Macrophages are phagocytic cells that dynamically change their phenotype and function in response to environmental cues. During tumor initiation and progression, macrophage behavior in the TME is connected to macrophage polarization. Although, it is an oversimplification, M1 (classic) macrophages show pro-inflammatory activities, while M2 (alternative) macrophages show pro-tumoral activities. Such a classification is defined by the phenotypic characteristics and up- and downregulation of specific markers. However, macrophage classification is complex and should be interpreted with caution.[110-111] As for gliomas, not only peripheral macrophages but also microglia, macrophage-like cells of the central nervous system, infiltrate the tumor environment and influence cancer progression. The macrophages can represent a large portion of the tumor volume, usually 30-50%.[112-114] Gabrusiewicz *et al*.[114] evaluated glioblastoma-associated myeloid cells from glioblastoma patients using immune phenotyping, whole-genome microarray analysis, and microRNA expression profiling and curiously enough found that their genetic profile is not corresponding to the M2-type but resembles the non-polarized M0 macrophage phenotype.

Even though TME cell heterogeneity is a well-known fact, most *in vitro* studies regarding nanomaterials only evaluate NP-cell interactions in cell monocultures, which may not properly reflect *in vivo* conditions. In Chapter III, we study the effect of NGs stiffness in mono- and co-culture of C6 glioma and J774 macrophage cells and discuss the relevance of co-culture models to comprehensively study the nanomaterials performance in TME.

2 CHAPTER II: LOW STIFFNESS FAVORS NANOGEL TRANSCYTOSIS ACROSS THE BLOOD-BRAIN BARRIER

Authors: Laís Ribovski;[1,2] Edwin de Jong;[1] Guangyue Zu;[1] Patrick van Rijn;*[1] Inge S. Zuhorn.*[1]

[1]University of Groningen, University Medical Center Groningen, Department of Biomedical Engineering, Groningen, the Netherlands. A. Deusinglaan 1, 9713 AV Groningen, The Netherlands

[2]Nanomedicine and Nanotoxicology Group, Physics Institute of São Carlos, University of São Paulo, CP 369, 13560-970 São Carlos, SP, Brazil

*Corresponding authors: Inge S. Zuhorn

E-mail address: i.zuhorn@umcg.nl

ABSTRACT

Transport of therapeutics across the blood-brain barrier (BBB) is a fundamental requirement for effective treatment of numerous brain diseases. However, most therapeutics (>500 Da) are unable to permeate through the BBB and do not achieve therapeutic doses. Nanoparticles (NPs) are being investigated to facilitate drug delivery to the brain. NP physicochemical properties, including size, surface charge, and surface chemistry have been shown to affect accumulation of NPs in the brain. Here, we investigate the effect of a physical characteristic, i.e., nanoparticle stiffness, on NP transport across an *in vitro* BBB model. Poly-N-isopropylmethacrylamide (p(NIPMAM)) nanogels were prepared by precipitation polymerization, while nanogel stiffness was varied by the inclusion of 1.5 mol% (NG1.5), 5 mol% (NG5), and 14 mol% (NG14) N,N′-methylenebis(acrylamide) (BIS) cross linker to investigate the stiffness effect on the nanogel transport across the BBB. Fluorescently labeled p(NIPMAM) nanogels were used to quantify nanogel uptake and transcytosis in an *in vitro* BBB model. The more densely cross-linked p(NIPMAM) nanogels showed the highest levels of uptake by polarized brain endothelial cells, whereas the less densely cross-linked nanogels demonstrated the highest transcytotic potential. These findings suggest that nanogel stiffness has opposing effects on nanogel uptake and transcytosis at the BBB.

Keywords: Nanogel. Blood-brain barrier. Nanoparticle stiffness. Transcytosis.

2.1 INTRODUCTION

Treatment and diagnosis of brain diseases e.g. neurodegenerative diseases and brain cancer are hindered by biological barriers, especially the blood-brain barrier (BBB). The BBB prevents that compounds reach therapeutic doses in the brain, hampering treatment efficacy and increasing side-effects and drug-resistance development. Nanoscale materials offer an opportunity to enhance treatment delivery, while materials properties critically determine delivery efficacy. Nanoparticle (NP) characteristics, including size,[115-118] surface chemistry[80,116,119] as well as surface functionalization with target-specific ligands[4,80,85,115,120-121,123] have been shown to influence NP transport across the BBB. One approach often used to enhance the transport of NPs across the BBB is to promote their endocytic uptake by brain endothelial cells.[4,120,122] Notwithstanding NP uptake has an important role in the process, NPs transcellular transport is also dependent on subsequent intracellular vesicle trafficking and exocytosis. Yu *et al*.[87] showed that high-affinity antibodies for the transferrin receptor accumulate to a lesser extent in the brain than low-affinity antibodies. Likewise, Wiley *et al*.[83] coupled different amounts of transferrin (Tf) to gold nanoparticles and investigated their interaction with brain endothelial cells. They demonstrated that NPs with larger quantities of Tf bind to the BBB but do not accumulate in the brain parenchyma as efficiently as NPs with lower amounts of Tf. Understanding both how nanosized materials are transported into cells and how they get through cell barriers is essential to design drug delivery strategies.

Understanding on how these nanosized materials are transported into cells and through cell barriers is essential to design delivery strategies. One class of materials to be explored are soft nanoparticles, regarding not only size and surface properties, but also stiffness. It has been shown that hydrophilic harder nanoparticles have a higher uptake by macrophages, cancer and endothelial at *in vitro* conditions, except in cases a polymeric particle (core) was encapsulated by a lipid layer (shell).[26,36-38,124-128] Also, soft particles favor *in vivo* circulation which leads to enhanced targeting at tumor sites, however, the difference in blood persistence and organs accumulation seems more pronounced for short observation times.[26,124-125,129] The adhesive wrapping of an elastic

vesicle by a membrane theoretical model described by Yi *et al*.[130] suggests that for a soft particle the membrane has no initial deformation but still needs to reach full wrapping phase, which will require a higher adhesion energy. Complementary to the evaluation of elasticity in spherical NPs, hydrophobicity and size can change the resulting outcome where theoretical analysis indicates increased hydrophobicity favors soft particles.[128] Although there have been considerable efforts to understand the cellular response to nanoparticle stiffness, theoretical and experimentally, few has been explored regarding stiffness effect on transcytotic capacity across the BBB.

Nanogels (NGs) are nanoparticles composed of a cross-linked hydrophilic polymer network. Important aspects of NGs are their customizable stiffness and low level of protein adhesion.[131-132] NG stiffness can be easily modulated by varying the extent of polymer crosslinking, with minimal alterations to the NG composition. This offers an excellent opportunity to evaluate the influence of nanoparticle stiffness on fundamental biological cellular processes, including transcellular transport. Here, we explored the effect of the stiffness of p(NIPMAM) nanogels on their interaction with an *in vitro* BBB model. NGs of ~200 nm with varying stiffness were made by inclusion of 1.5 mol%, 5 mol%, and 14 mol% N,N′-methylenebis(acrylamide) (BIS) cross-linker during synthesis. The stiffer NG14 nanogel showed higher uptake by brain endothelial cells than the softer NG1.5 and NG5 nanogels. In contrast, NG1.5 and NG5 exhibited higher levels of transcytosis compared to NG14. An increase in the size of NG particles to ~400 nm, while keeping stiffness constant, was shown not to influence uptake nor transcytosis. Altogether, our data suggest that nanogel stiffness has opposing effects on nanogel uptake and transcytosis at the BBB and that stiffness is a more determinant factor than size for the transcytosis of NG particles. Whereas high stiffness of NGs promotes uptake by brain endothelial cells, low NG stiffness stimulates transcytosis across the *in vitro* BBB.

2.2 METHODS AND MATERIALS

2.2.1 Nanogel synthesis

Nanogels were synthesized by precipitation polymerization as previously described with some adaptations to suit this study purposes.[133] Briefly, NIPMAM (Sigma-Aldrich #423548), nile blue acrylamide (NLB, Polysciences #25395), BIS (Sigma-Aldrich #146072) and sodium dodecyl sulfate (SDS) were added to a 100 ml glass round-bottom flask and dissolved in 45 ml of filtered ddH_2O (0.2 µm Whatman filter), stirred and purged with N_2. The solution was placed in an oil thermal bath at 70 °C and ammonium persulfate (APS, Sigma-Aldrich #A3679) dissolved in ddH_2O and purged with N_2 was added after 30 min. Polymerization time was recorded after addition of APS. Prior to use, NIPMAM 97% was purified by recrystallization from n-hexane and dried at reduced pressure using a rotary evaporator. Table 2.1 details the formulation conditions of the different nanogels used in this study. Variations in the crosslinking degree affects nanogels stiffness.

Table 2.1 - Synthesis conditions to obtain p(NIPMAM) nanogels with different cross-linking densities, sizes and monodisperse populations. All reactions were performed at 70°C in oil bath.

Nanogel	**NIPMAM**		**BIS**		**SDS**	**NLB**	**APS**	**Polymerization time**
	mg	mol%	mg	mol	mM	mg	mg	hours
NG1.5	626	98.5	12	1.5	1.6	8	11	4
NG5	604	95	39	5	2.5	10	11	2.5
NG14	604	86	117	14	2.5	10	11	2.5
$NG5^{large}$	604	95	39	5	1.6	10	11	> 6

Source: By the author.

The SDS concentration (Figure S1, Appendix A) and polymerization time (Figure S2, Appendix A) affect the nanogels size and dispersity and were varied to obtain monodisperse nanogels at 200 and 400 nm range sizes and monodispersity.

All nanogels were extensively dialyzed in ethanol 96 %vol (AnalaR NORMAPUR® – VWR) followed by dialysis in ddH_2O using a cellulose dialysis tube (6-8 kDa cutoff, Spectrum™) and dialysis medium was changed at least once a day. After dialysis nanogels were freeze-dried.

2.2.2 Nanogel characterization

Size and PdI at 37°C, zeta potential (ζ-potential) at room temperature and temperature-dependent behavior were determined using a Zetasizer Nano ZS (Malvern Instruments). The nanogels show a thermoresponsive behavior shifting between swollen and collapsed states with volume phase transition temperature (VPTT) at 44˚C, being swollen at 37˚C, i.e., at physiological body temperature, and collapsed at temperatures > 44˚C. 20 μg ml^{-1} nanogels in 1 mM SDS in ddH_2O to obtain the thermoresponsive curves between 20 and 60°C with 2°C intervals and an equilibration time of 180 s. TEM images were acquired on a transmission electron microscope and analyzed using Fiji.[134] At least 100 particles were measured to obtain the size range, except for 1.5 mol% BIS where 25 particles were measured due to sample limitation. The swelling ratio reflects nanogels cross-linking density and was determined by the ratio between hydrodynamic diameter at swollen and collapsed states.

Negative staining of nanogels drop-casted over carbon film-coated copper grids was performed with 5 μl of 2% uranyl acetate. Samples were investigated with a Philips CM120 electron microscope coupled to a 4k CCD camera operated at 120 kV. Images were analyzed using Fiji software.[134] At least 100 particles were measured for each nanogel formulation for size analysis, except for 1.5 mol% BIS nanogels where 25 particles were measured because of sample limitation.

2.2.3 Brain endothelial cell culture

Human cerebral microvascular endothelial cell line (hCMEC/D3) cells were cultured in endothelial basal medium 2 (EBM-2; Lonza, #CC-3156) supplemented with 5% (v/v) foetal bovine serum (FBS), 5 µg ml^{-1} ascorbic acid (Sigma-Aldrich #A4544), 1 ng ml^{-1} basic fibroblast growth factor (PeproTech, #100-18D), 1% (v/v) chemically defined lipid concentrate (Gibco #11905-031), 10 mmol L^{-1} HEPES (Gibco #15630106), 1.4 µmol L^{-1} hydrocortisone (Sigma # H0888) and 1% (v/v) penicillin-streptomycin in 25 cm^2 flasks coated with 150 µg ml^{-1} rat tail collagen type-I (Enzo Life Sciences, #ALX-522-435, LOT 08071815 or LOT 04201734). Cells were grown at 37ºC in an incubator with 5% CO_2 atmosphere and used for experiments at passage 28 to 38.

2.2.4 Transcytosis assay

Transcytosis assays were performed using a filter-free blood-brain barrier model previously described in detail by our group.[84] In short, collagen gels were prepared from a 5 mg ml^{-1} rat tail collagen type-I sterile solution in 0.02 N acetic acid that was neutralized by 1 mol L^{-1} NaOH, made isotonic from 10x phosphate-buffered saline (PBS) and diluted to 2 mg ml^{-1} with sterilized ddH_2O and final buffer composition of 1x PBS. hCMEC/D3 cell were grown over the collagen gels for 5 days at initial seeding density of 1×10^5 cells per cm^2, the medium was changed every other day and cells were washed with HBSS at day 2 and 5. After 5 days, the monolayer reached confluency and nanogels transcytosis was assessed as well as monolayer permeability. At 100 µg ml^{-1} in complete EBM-2 medium, 500 µl of each nanogel was incubated for 2, 4 or 16 hours after washing the cell layer once with 1x Hank's balanced salt solution (HBSS). One hour before incubation period was finished, 55 µl of 5 mg ml^{-1} fluorescein isothiocyanate (FITC)-labelled dextran of 4 kDa (Sigma-Aldrich #FD-4) was added to the apical compartment to evaluate paracellular permeability. The percentage of nanogels associated to each compartment - apical, cell and basolateral - is expressed as the fluorescence of each compartment over the total fluorescence over all compartments

with excitation at 633 nm and emission at 680 nm. Basolateral compartment values were correct using samples without treatment, also in duplicate, due to collagenase A.

$$\%\, nanogels = \frac{compartment\ fluorescence}{total\ fluorescence}\ x\ 100 \qquad (2.1)$$

Apparent permeability (P_{app}) was calculated using the following equation

$$P_{app} = \left(\frac{\Delta Q}{\Delta t}\right) A C_0 \qquad (2.2)$$

where $\Delta Q/\Delta t$ represents the rate of permeation of dextran (µg min^{-1}), A is the surface area (cm^2), C_0 is the initial concentration of FITC-dextran (µg ml^{-1}) when added to the apical side. FITC-dextran fluorescence was recorded at λ_{ex} = 485 nm and λ_{em} = 520 nm. Apparent permeability was verified for all samples and assays. The fluorescence was measured using Synergy H1 Hybrid plate reader (BioTek Instruments Inc.)

2.2.5 Flow cytometry assessment of nanogel uptake in polarized brain endothelial cell monolayers

hCMEC/D3 cells were seeded in 24-well plates pre-coated with 150 µg ml^{-1} collagen rat tail collagen type-I at a density of $1x10^5$ cells per cm^2. Cells were grown for 5 days and media was changed every other day. At the 5^{th} day, media was removed and cells were washed once with 1x HBSS. 500 µl of 100 µg ml^{-1} nanogel in EBM-2 complete media was added to each well and incubated for 15, 30 and 120 minutes. After incubation, medium containing nanogels was removed, cells were washed twice with 1x HBSS and 200 µl trypsin-EDTA was added per well and incubated for 5 min for cell detachment. 400 µl of EBM-2 (5%FBS) complete were added to each well, cells were pipetted vigorously up and down at least 10 times and samples were collected. Wells were washed once with 200-400 µl of 1x HBSS to collect remaining cells. Samples were centrifuged (500 g, 5 min, 4°C), the supernatant was discarded and the cells were resuspended in 400 µl of ice-cold 1x PBS supplemented with 2% (v/v) FBS and 5 mM

EDTA (PFE buffer). For experiments at 4°C, the cell layer was incubated at 4°C for 30 min and ice-cold 1xHBSS was used to wash the cells prior to ice-cold nanogel incubation for 2 hours at 4 °C. Nanogels were removed and cells washed with ice-cold 1x HBSS two times, followed by trypsinization. Fluorescence in cells was measured with a CytoFlex S Flow Cytometer (Beckman Coulter) using the APC channel (670/30 band pass filter) and laser excitation 640 nm. Data were analyzed using FlowJo V10 software (Tree Star, Inc.) and Origin. Because the different nile blue-labelled nanogels do not have the same fluorescence intensity, the geometric mean fluorescence values were corrected according to the fluorescence of each nanogel at 656 nm ($\lambda_{excitation}$ = 633 nm) at 100 µg ml^{-1} in EBM-2 complete medium (Figure S3, Appendix A) in order to compare the cellular uptake of the different nanogels.[135]

2.2.6 Confocal microscopy of nanogels in polarized brain endothelial cell monolayers

Collagen gels were prepared on glass slides using polydimethylsiloxane (PDMS) gel as a mold (Supplementary Information). hCMEC/D3 cells were seeded at an initial density of 1 x 10^5 per cm^2 and grown for 5 days in EBM-2 medium with supplements. Medium was changed every day. After 5 days, medium was removed and the monolayer was washed once with 1x HBSS, followed by incubation with 50 µg of nanogel in 500 µl of EBM-2 medium with supplements for 2 hours. 30 minutes before incubation was finished, Hoeschst was added to the cells at a final concentration of 2 µg ml^{-1}. Apical medium containing nanogels and Hoeschst was removed and the cell monolayer was washed twice with 1xHBSS before fixation. Cells were incubated with 3.7% paraformaldehyde (PFA) in 1xPBS for 15 min, followed by 3 washes with 1xPBS and incubation with 0.2% (v/v) of Triton X-100 in PBS for 10 minutes. Again, the monolayer was washed with 1xPBS thrice for 15 min under mild agitation. Cells were incubated with Phalloidin-FITC (Sigma-Aldrich #P5282) at 1:100 dilution for 90 minutes protected from light. Wash was performed three times, samples were mounted with PBS:glycerol (50:50) and a cover slip was carefully placed over the samples. Images were collected using a Leica TSC SP2 confocal microscope (63x immersion oil objective) and analyzed

with Fiji software.[134] Z slice images were collected sequentially using two or three channels and excitation lasers 488 (ArKr) and 633 nm (HeNe). Ninety stacks were collected for each image, each image being an average of two frames composed of 512 × 512 pixels.

2.3 RESULTS

2.3.1 Nanogel characterization

P(NIPMAM) nanogels of varying stiffness were prepared by tuning their cross-linking densities and reactant contents. Nanogels of ca.200 nm diameter were prepared with 1.5, 5, and 14 mol% BIS crosslinker. The size of the nanogels was determined by means of dynamic light scattering, and confirmed by TEM (Table 2.2, Figure 2.1A-C). All nanogels showed a negative ζ-potential (Table 2.2). In addition, nanogels of ca. 400 nm diameter and 5 mol% BIS crosslinker were prepared (Table 2.2, Figure 2.1D). Nanogels with similar sizes and different cross-linking densities showed the highest swelling ratio for the nanogel with the lower amount of crosslinker (Table 2.2, Figure 2.1E). Nanogels with different sizes and the same crosslinker density showed a similar swelling ratio (Table 2.2).

Table 2.2 - p(NIPMAM) nanogel properties. [1]Number of particles measured from TEM images to estimate nanogel size. [2] PdI was recalculated according to a single peak. 3 For NG1.5 we report

	Z-average at 37 °C (nm)	PdI	TEM size (mean ± SD) (nm)	Swelling ratio ($d_{swollen}/d_{collapsed}$)	ζ-potential at 25 °C (mV)
NG1.5	274/170 ± 44[3]	0.07[2]	148 ± 18 (25)[1]	2.4+-0.1	-6.8 ± 3.1
NG5	230 ± 64	0.04	222 ± 56 (101)[1]	1.9 ± 0.1	-9.9 ± 6.5
NG14	175 ± 40	0.02	163 ± 56 (107)[1]	1.5 ± 0.02	-23.4 ± 7.9
$NG5^{large}$	423 ± 118	0.06	474 ± 121 (379)[1]	2.1 ± 0.08	-6.5 ± 5.5

Source: By the author.

Swelling ratio is significantly different between nanogels with different crosslinking densities but not between nanogels NG5 and $NG5^{large}$ (Table 2.2, Figure 2.1E). ζ-potential distributions at 25 °C are equivalent between all nanogels except between NG1.5 and NG14.

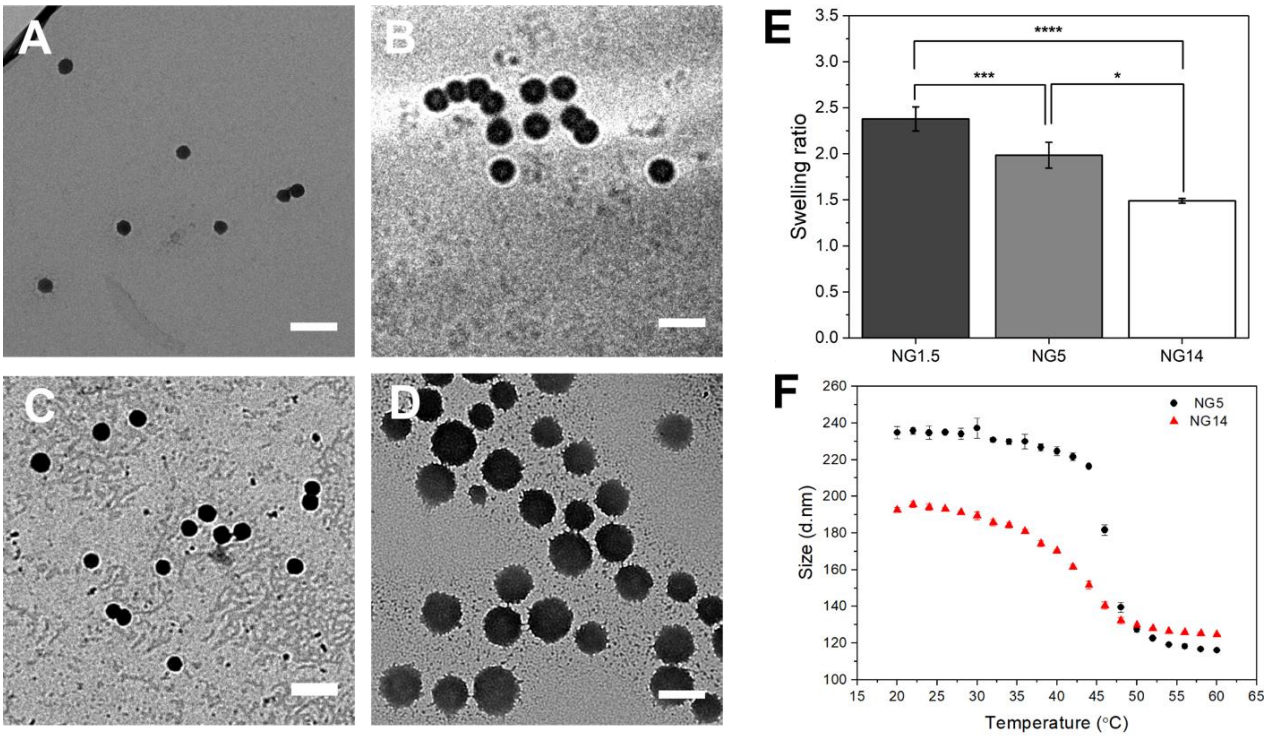

Figure 2.1 - pNIPMAM nanogel characterization. pNIPMAM nanogel images obtained by negative staining by transmission electron microscopy with A) 1.5 mol% BIS (NG1.5), B) 5 mol% BIS (NG5), C) 14 mol% BIS (NG14) and D) 5 mol% BIS (NG5l^{arge}). E) Swelling ratio of NG1.5, NG5 and NG14, and F) thermoresponsive curves displaying the hydrodynamic diameter as a function of temperature (increment 2ºC) for nanogels NG5 and NG14. Bars: 500 µm.
Source: By the author.

The observed p(NIPMAM) nanogel thermoresponsive behavior reveals an inverse correlation between cross-linking density and swelling ratio, which is in accordance with literature, i.e., micro/nanogels with higher cross-linking density show a lower swelling ratio, which is indicative for an enhanced stiffness.[75,79]

2.3.2 High nanogel stiffness favors uptake by polarized brain endothelial cell monolayers

Previous studies have indicated that stiffer particles generally present higher internalization levels in eukaryotic cells, including endothelial cells.[26,80] This phenomenon has been attributed to an easier wrapping of the plasma membrane of cells around stiff particles.[39] Here, the uptake of nanogels with varying stiffness, i.e., NG1.5, NG5, and NG14, was measured in polarized hCMEC/D3 cell monolayers.

Fluorescently labeled nanogels were incubated with hCMEC/D3 cell monolayers for 15, 30, and 120 minutes at 37 °C.

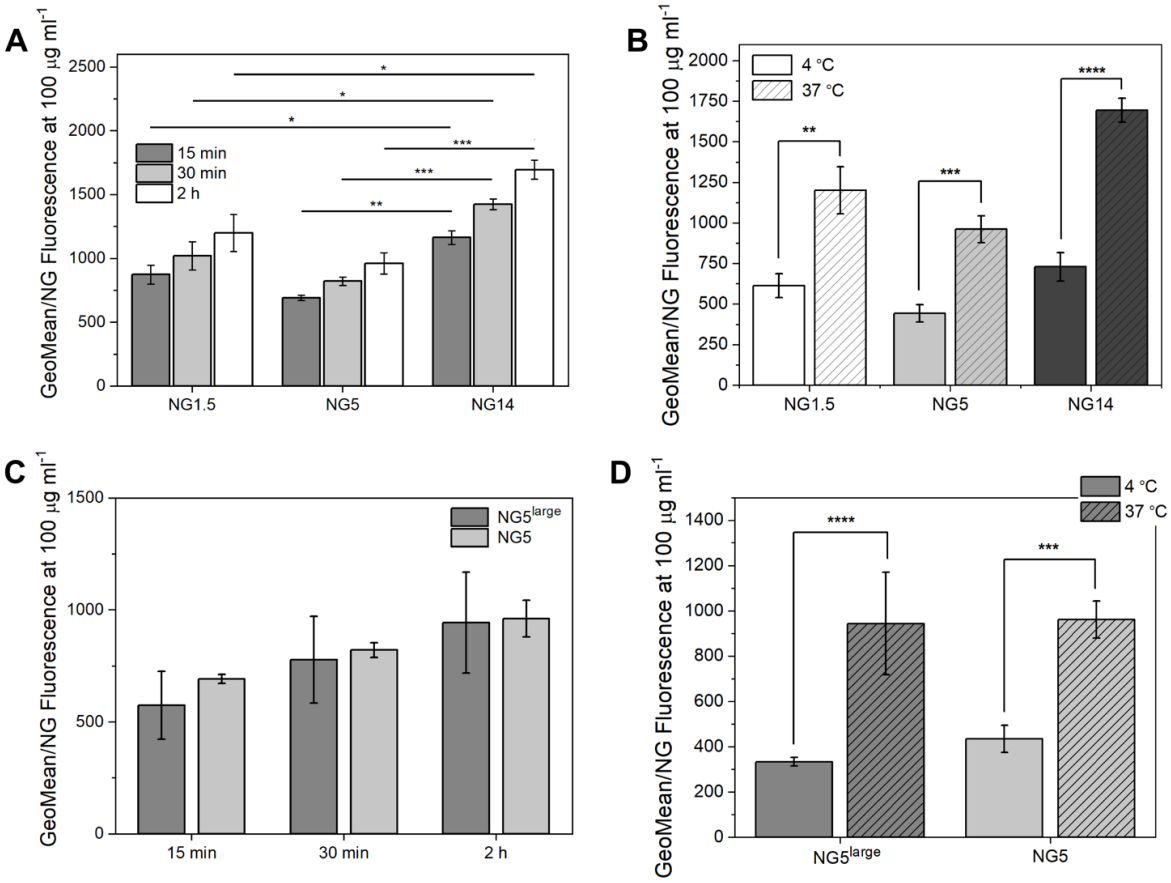

Figure 2.2 - Nile blue-labelled nanogels uptake. Effect of NG stiffness on the uptake by a monolayer of hCMEC/D3 polarized cells A) at 37 ºC with incubation times of 15, 30 and 120 minutes and B) at 4 and 37°C with 2 h incubation. Uptake levels NG with same crosslinking content and different sizes C) 37 ºC with incubation times of 15, 30 and 120 minutes and D) at 4 and 37 ºC with 2 h incubation. Represented values are mean ± SD of three experiments with at least 40000 events. Data was analyzed using two-sample t-test and significances are indicated by * for p-value < 0.05, ** for p-value < 0.01, *** for p-value < 0.005 and **** for p-value < 0.0005.
Source: By the author.

Figure 2.2A shows that NG1.5 and NG5 show similar uptake by hCMEC/D3 cells, whereas the uptake of NG14 nanogels is significantly higher. In addition, the effect of nanogel size on uptake by hCMEC/D3 cell monolayers was investigated. Two NG formulations with the same crosslinking density but different sizes, i.e., NG5 and $NG5^{large}$, were incubated with hCMEC/D3 cell monolayers for 15, 30, and 120 minutes (37 °C). Both types of NGs were internalized by hCMEC/D3 cells to a similar extent (Figure 2.2C), indicating that NGs with a size of 425 nm are internalized as efficiently as

NGs of 230 nm.

Theoretical models indicate that soft particles must overcome a high-energy barrier to induce their enwrapping by the plasma membrane of cells. This is due to the fact that soft particles induce low membrane bending, which is caused by their spreading over the cell surface due to particle deformation.[39-40, 130] Moreover, using coarse-grained molecular dynamics Shen et al. showed that the difference in wrapping efficiency of soft and rigid particles scales with particle size.[138] With that in mind, we could explain the lack of significant variation in uptake between NG1.5 and NG5 as an insufficient variation in particle stiffness ($\Delta E_{NG5\text{-}NG1.5}$ = 96 kPa) for particles in the 150-250 nm size range, and suggest that there is a rather sharp response toward NG stiffness.

Figure 2.3 shows that virtually all cells in the cell monolayer contain NGs (quantified in Table S1, Appendix A) which tend to accumulate at the perinuclear region. The cellular distribution was similar for all 4 NGs. Of note, because of the different fluorescence intensities of the different NG formulations (see Figure S3) a comparison of the uptake levels of the different NGs by direct visual inspection of the fluorescence images is not possible.

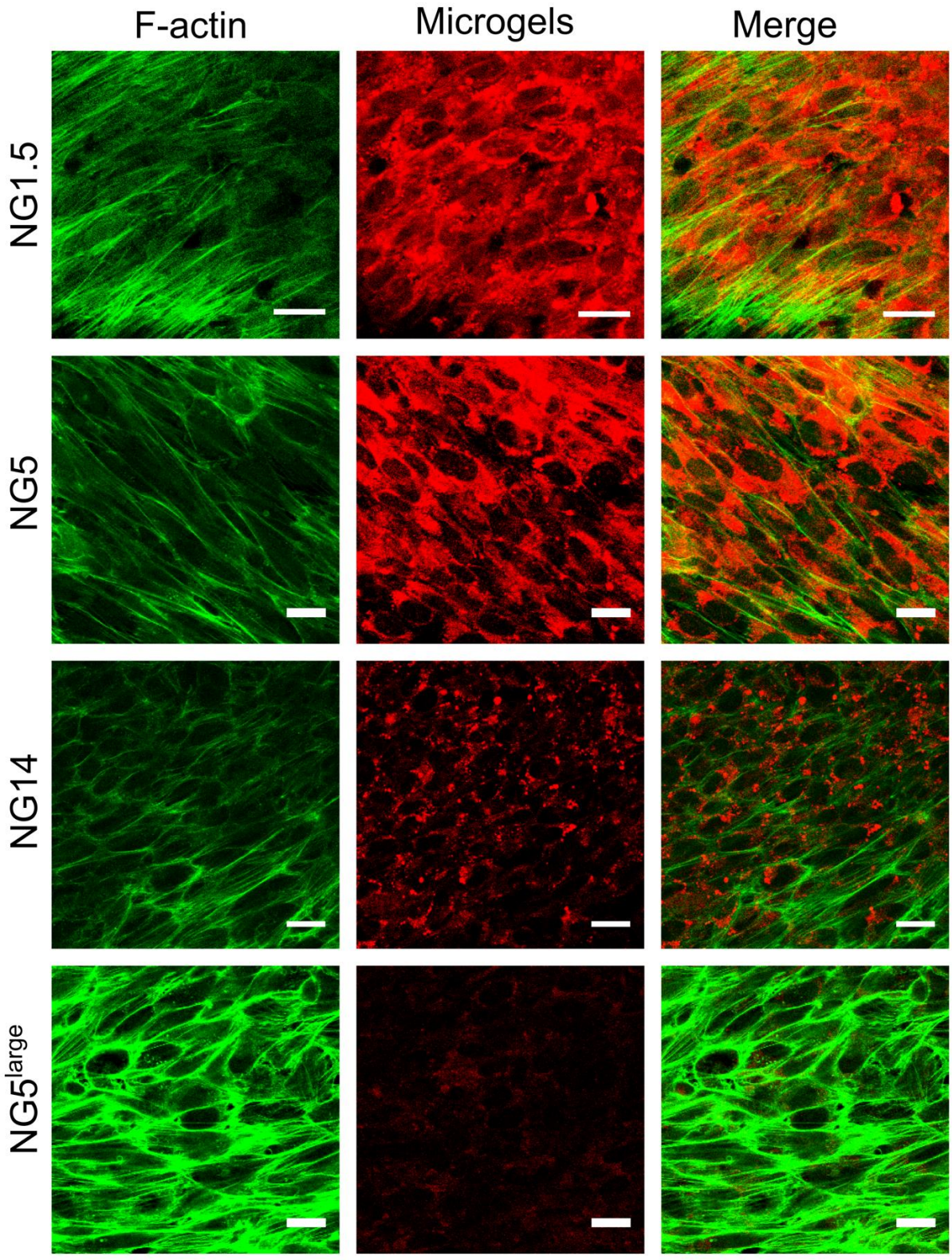

Figure 2.3 - Representative confocal microscopy images of hCMEC/D3 cell monolayers interaction with nanogels NG1.5, NG5, NG14 and $NG5^{large}$ after 2 h incubation at 37°C, followed by fixation and F-actin staining. Scale bars are 20 µm. Images were obtained using the same settings.
Source: By the author.

When NG uptake studies in hCMEC/D3 cell monolayers were performed at 4 °C, reduced uptake levels were observed for all 4 types of NGs (Figure 2.2B and 2.2D). This indicates an involvement of an active, energy-dependent process in the nanogel internalization process. The reduction in NG uptake by hCMEC/D3 cells after incubation at 4 °C compared to incubation at 37 °C is more prominent for cells incubated with the stiffer NGs, i.e., 2.0, 2.2, and 2.3-fold for NG1.5, NG5, and NG14, respectively (Figure 2.2B) This would fit with the theory that stiff particles (passively) induce plasma membrane deformation that triggers (active) endocytosis, whereas soft particles that exhibit high deformability less efficiently trigger endocytosis because they induce less membrane deformation.[130] Lowering the temperature will not prevent deformation, but it will inhibit endocytosis. As a consequence, the largest inhibition in uptake when lowering the temperature below the endocytosis-permissive temperature is to be expected for the stiffest NGs. In line with this, the largest reduction in the number of NG-positive cells following incubation at 4 °C compared to 37C was observed for cells incubated with NG14. Following incubation at 4 °C, the cellular uptake of $NG5^{large}$, was reduced 2.8-fold, while for NG5 the reduction was 2.2-fold (Figure 2D).

2.3.3 Low nanogel stiffness favors transcytosis across polarized brain endothelial cell monolayers

The effect of NG stiffness on NG transport across an *in vitro* BBB model was investigated. Fifty µg of nile blue-labelled NG1.5, NG5, $NG5^{large}$, and NG14 was incubated at 100 µg ml^{-1} for 2, 4 and 16 hours with the filter-free BBB model, after which the fluorescence in the apical, cell, and basal compartments was quantified. After 2 h incubation, the softer particles NG1.5 and NG5 showed an enhanced accumulation at the basal side of the cell monolayer compared to the stiffest NG14 nanogel (Figure 2.4A). Longer incubation periods resulted in a modest increase in basal accumulation of the NGs with again highest basal accumulation for NG1.5 and NG5 (Figure 2.4B, C). $NG5^{large}$ and NG5 exhibited a similar transcytotic capacity (Figure 2.4A). To exclude paracellular transport of NGs due to a compromised BBB, the P_{app} of the hCMEC/D3 cell monolayers for 4 kDa dextran, a marker for paracellular leakage, was evaluated during

the final 60 min of incubation with the NGs. Incubation of cell monolayers with NGs did not induce an increase in the P_{app} for dextran compared to control cells, indicating that the barrier properties of the BBB model remained intact during incubation with NGs (Figure 2.4F). When calculating the percentage of nanogels that interacted with the cellular compartment and reached the basolateral compartment, it becomes evident that the softer nanogels NG1.5 and NG5 are more efficiently secreted at the basal side of the hCMEC/D3 monolayer than the stiff NG14 nanogel (Figure 2.4D).

Taken together, our data show that increased levels of uptake do not necessarily lead to improved transport across the BBB. This means that a greater internalization level might not lead to enhanced transcytosis. Similarly, Freese et al.[139] demonstrated that elevated cell association of poly(2-hydroxypropylmethacrylamide) coated-gold nanoparticles did not result in their improved transport across the BBB, which was attributed to the confinement of the particles in intracellular vesicles. A negative correlation between ligand-receptor affinity and transcytosis has been observed for TfR antibodies.[87, 140] Intermediate ligand-receptor affinity was shown to promote TfR antibody transcytosis, while high affinity was connected to delivery to lysosomes. A similar positive correlation between intermediate ligand-receptor affinity and transcytosis at the BBB has been reported for receptors at the BBB other than the transferrin receptor.[141-142] However, intermediate affinity of ligand-decorated nanoparticles to cells generally leads to lower uptake compared to nanoparticles with high affinity. Clark and Davis ingeniously obviated the need to use intermediate ligand-receptor affinity through the use of gold nanoparticles decorated with acid-cleavable ligands.[143] They demonstrated that gold nanoparticles functionalized with an acid-cleavable transferrin ligand reached the brain parenchyma at higher quantities compared to gold with non-cleavable transferrin (Tf). Following endocytosis of the gold nanoparticles, the separation between the particle and Tf, as induced by a drop in endosomal pH, was held responsible for facilitating nanoparticle release at the basal side of the BBB.

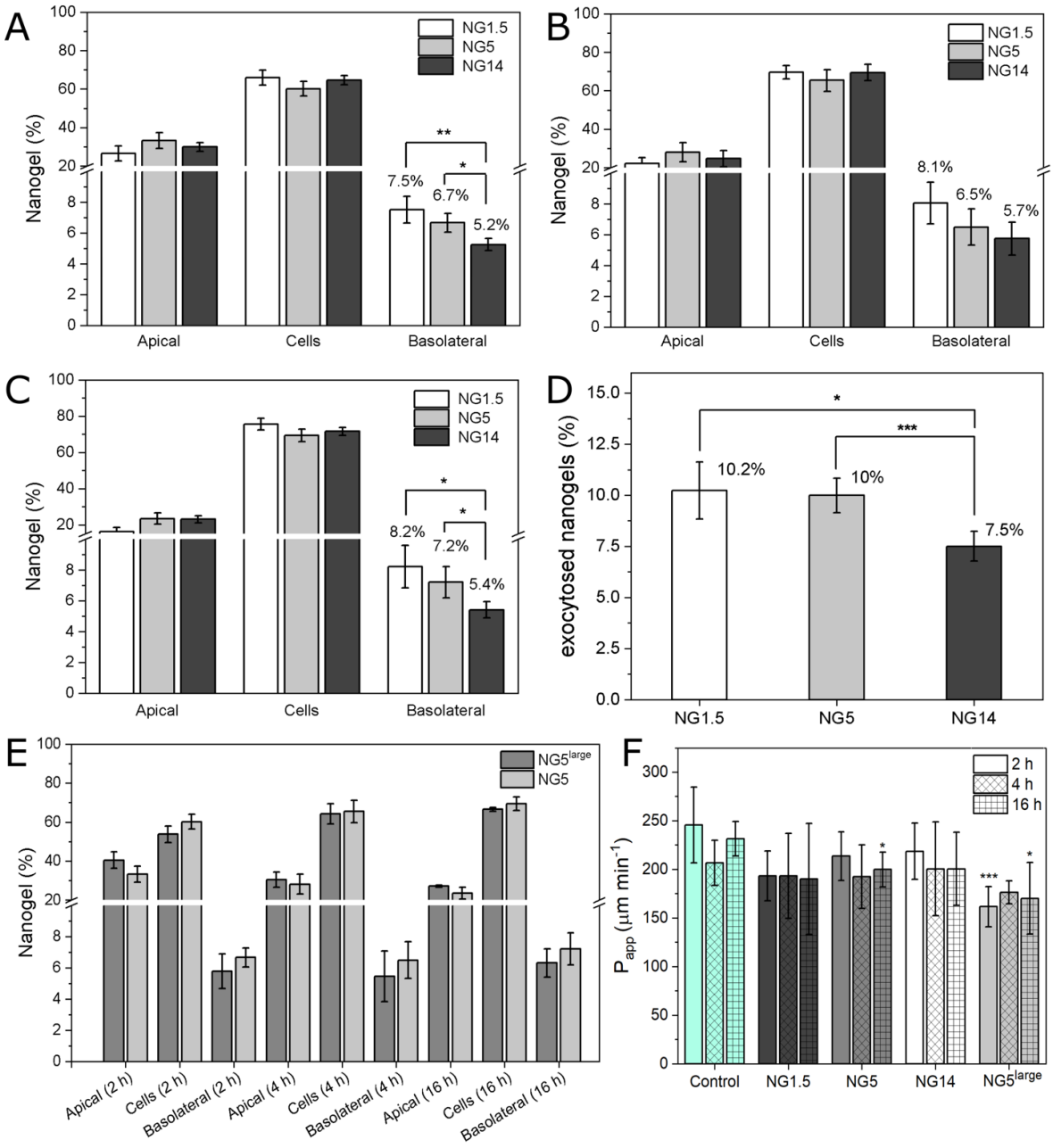

Figure 2.4 - Effect of NG size and stiffness on NG transport across an *in vitro* filter-free BBB model. hCMEC/D3 cell monolayers were incubated with nile blue-labeled NG1.5, NG5, and NG14 at 37 ºC for (A) 2, (B) 4, and (C) 16 hours, after which fluorescence in the apical, cell, and basal fractions was determined by fluorescence spectroscopy. (D) Percentage of exocytosed nanogel (exocytosed nanogel (%) = $fluorescence_{basolateral}$ x 100/($fluorescence_{cells}$ + $fluorescence_{basolateral}$) after 2 h incubation. (E) Transcytosis levels for NG5 and $NG5^{large}$ after 2, 4 and 16 h incubation. (F) Apparent permeability (P_{app}) of FITC-dextran (MW 4 kDa) in hCMEC/D3 cell monolayers incubated with NG1.5, NG5, NG14 and $NG5^{large}$ for 2, 4 and 16 hours. Control is hCMEC/D3 cell monolayer incubated without nanogel. Values are represented as mean ± SD of four independent experiments and each experiment was performed in duplicate. Data were analyzed using two-sample t-test and statistically significant differences are indicated by * for p-value < 0.05, ** for p-value < 0.01 and *** for p-value < 0.05

Source: By the author.

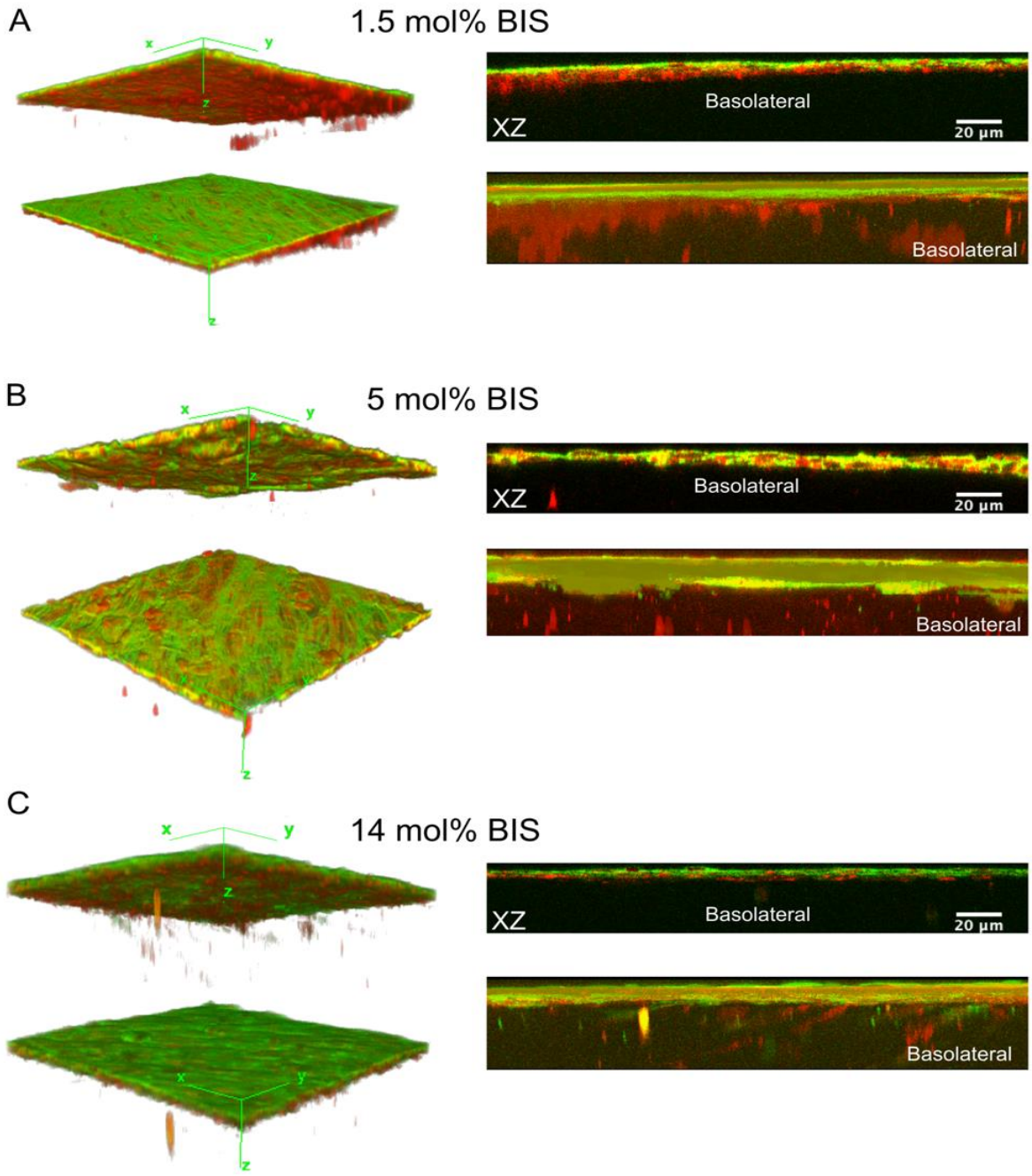

Figure 2.5 - Nile blue-labelled nanogel-cell interaction in a filter-free *in vitro* BBB model with hCMEC/D3 polarized cells after 2 h incubation of nanogels A) NG1.5, B) NG5 and C) NG14 at 37°C. 3D viewing (left) displays basolateral (top) and apical (bottom) views of nanogels (red) interaction with F-actin (green) from hCMEC/D3 cell layers and collagen gel. Z-stacks were also represented in XZ orthogonal views (right, top) and three-dimension projections (right, bottom). Images were acquired with same system settings.

Source: By the author.

To visualize transcytosed NGs in the BBB model, hCMEC/D3 polarized cell monolayers on collagen gels were prepared using a PDMS mold (see Material and Methods), incubated for 2 hours with fluorescently labeled NGs, and investigated by confocal microscopy. Figure 2.5 supports the nanogels' ability to be internalized by the endothelial cell layer and cross the BBB. Orthogonal views indicate that nanogels interact with BBB and three-dimension projections substantiate that nanogels reach basolateral side and collagen gel.

2.4 CONCLUSION

To investigate the influence of nanoparticle stiffness on nanoparticle transport across the blood-brain barrier, p(NIPMAM) nanogels with varying crosslinking densities, i.e., 1.5 mol%, 5 mol%, and 14 mol% BIS were prepared. As expected, the crosslinking density of the NGs showed a positive correlation with their stiffness (Young's modulus). Upon their incubation with an *in vitro* BBB model, composed of a polarized hCMEC/D3 cell monolayer grown on a collagen gel, the more densely cross-linked p(NIPMAM) nanogels (NG14) showed the highest level of uptake by polarized brain endothelial cells, whereas the less densely cross-linked nanogels (NG1.5, NG5) demonstrated the highest transcytotic potential. These findings suggest that nanogel stiffness has opposing effects on nanogel uptake and transcytosis at the BBB. If decoration of soft nanogels with ligands would improve their uptake without changing their transcytotic capacity remains to be investigated.

Since the process of transcytosis involves not only cellular uptake via endocytosis, but also intracellular vesicle trafficking and exocytosis, we hypothesize that low NG stiffness promotes intracellular trafficking and exocytosis. In addition, NGs with different stiffnesses may get internalized via different endocytic pathways that are intrinsically connected to transcytosis to a different extent. Furthermore, the effect of NG stiffness on cellular uptake and transcytosis may (partly) be an indirect effect, caused by the formation of distinct protein coronas on soft and more rigid NGs. Although, protein corona formation on nanoparticles is extensively being investigated,[144] there are just few studies describing the protein corona of nanogels.[131-132,145-147] These studies show that

protein adhesion to nanogels is low compared to adhesion to nanoparticles, while nanogel hydrophobicity promotes protein adhesion.

Our finding that soft p(NIPMAM) nanogels are more efficiently transported across an *in vitro* BBB than their stiff counterparts could be exploited in the design of soft nanogels for drug delivery across the BBB, to improve current and future treatment of brain diseases.

3 CHAPTER III: ASSESSMENT OF NANOGELS STIFFNESS EFFECT ON DIRECT CO-CULTURE OF GLIOMA CELLS AND MACROPHAGES.

Authors: Laís Ribovski;[1,2] Gwenda Vasse;[1] Mirjan Koster;[1] Patrick van Rijn;*[1] Inge Zuhorn.*[1]

[1]University of Groningen, University Medical Center Groningen, Department of Biomedical Engineering, Groningen, the Netherlands. A. Deusinglaan 1, 9713 AV Groningen, The Netherlands

[2]Nanomedicine and Nanotoxicology Group, Physics Institute of São Carlos, University of São Paulo, CP 369, 13560-970 São Carlos, SP, Brazil

*Corresponding authors: Inge S. Zuhorn

E-mail address: i.zuhorn@umcg.nl

ABSTRACT

Nanoparticles (NPs) are being developed for the delivery of drugs to disease targets. The interactions of NPs with biological systems critically determine NP drug delivery efficiency and need to be better understood to optimize nanomaterials to better serve their intended purpose. Generally, *in vitro* studies are performed in which NPs interact with mono cell cultures. However, *in vivo* cells are part of a cooperative regulated environment that contains multiple cell types. For example, in tumors the microenvironment includes, besides cancer cells, macrophages. Macrophages are known to have a great impact on the efficacy of nanomedicine, due to their phagocytic capacity. In glioma (a form of brain tumor), not only peripheral macrophages are associated with the tumor cells but also microglia, the resident macrophages of the central nervous system (CNS). Together they form the glioma-associated macrophages (GAMs). In addition, macrophages in the circulation impact the circulation half-life of NPs and, consequently, their accumulation at the target site. Taking these facts into consideration, an appropriate *in vitro* assessment of NPs capacity to target glioma should not only consider the interaction of the NPs with glioma cells but also the interaction with GAMs. Here, we explored the interaction of monocultures and direct co-cultures of C6 glioma cells and J774 macrophages with poly(N-isopropylmethacrylamide) (p(NIPMAM)) nanogels (NGs) of different stiffness and sizes.

We identified that stiff and large NGs are more efficiently internalized by C6 glioma cells and J774 macrophages than soft and small NGs. In monocultures and co-cultures the absolute uptake of stiff and large NGs is significantly higher for J774 than C6 cells, which is expected based on the phagocytic activity of macrophages. In monocultures, the soft NGs are equally internalized by C6 and J774 cells, while in co-culture uptake of the soft NGs by J774 is enhanced at the expense of uptake by C6 cells. We hypothesize that the increased internalization of NPs by macrophages in co-culture may be associated with macrophage stimulation in the presence of glioma cells and/or distinct corona profiles on the NGs. Additionally, soft NGs were found to be cytotoxic towards C6 glioma cells, which was correlated with higher ROS production by C6 glioma cells in the presence of soft NGs. However, in direct co-culture ROS levels

and cytotoxicity were diminished, which suggests a cytoprotective effect of the presence of macrophages on glioma cells. The observed differences in C6 glioma and macrophage responses toward NGs in monocultures compared to co-cultures, suggest a potential benefit of investigating NP performance in co-culture systems.

Keywords: nanoparticles, glioma, tumor microenvironment, tumor-associated macrophages, co-culture, nanogels, stiffness.

3.1 INTRODUCTION

The tumor microenvironment (TME) is a complex system composed of cancer cells and a variety of other, non-neoplastic cell types. One particular cell type that accounts for roughly 30-50% of the cells present in the TME are macrophages.[112] In glioma infiltrating macrophages from the bone marrow and microglia, together termed glioma associated macrophages (GAMs), are present.[112,148] GAMs are recruited by glioma cells and have an impact on tumor formation and growth, while macrophages and microglia are described to distribute to different tumor regions and be recruited at different stages of tumor formation and progression.[148-149] For example, both macrophages and microglia have been described to influence tumor neovascularization.[150-152] However, we should highlight that markers to discriminate between microglia and macrophages are still poorly described and literature is contradictory. Nonetheless, it is well understood that the presence of macrophages and microglia in gliomas modulates the tumor environment and development, and ultimately patients' prognosis. Moreover, the action of macrophages affects the concentration of nanomaterials and their drug delivery efficacy at the tumor.[134, 153-156] Therefore, it is imperative to understand the interaction between nanoparticles (NPs) and glioma cells but also glioma associated macrophages in order to design NPs for glioma treatment.

Strategies for NP evasion from macrophage action are widely sought with varying success. One strategy is to modify nanomaterials with CD47, i.e., a "do not eat me sign".[157-159] CD47 is an integrin-associated protein present in normal cellular membranes, and commonly overexpressed in cancer cells, which avoids that these cells are engulfed and cleared by the mononuclear phagocytic system (MPS). Likewise, CD47 anti-phagocytic activity is related to the inability of microglia and macrophages to phagocytose glioma cells.[149, 160] CD47 has been widely applied in immunotherapy[161] and also in nanomedicine to avoid the clearance of NPs by macrophages. Main methods employed are the covering of the NP surface with anti-CD47 or with complete cellular membranes.[157-158] Another strategy for macrophage evasion is the use of poly(ethylene glycol) (PEG) coated NPs. PEG coated NPs show reduced interaction with the immune

system by preventing NP opsonization by serum proteins.[162] Several reports show that pegylated NPs avoid macrophages, which can be tuned by adjusting the density of PEG.[163] Gold nanoparticles (AuNPs) pegylated with different molecular weights of PEG (2, 5 and 10 kDa) showed longer blood half-life for the AuNPs with larger PEG brush layers. In addition, the ratio between the hydrodynamic diameter of the pegylated particle to its core size was shown to affect blood half-life, showing longer circulation for particles with similar hydrodynamic size but a smaller gold core.[164] The positive effects of a larger PEG brush layer and a smaller NP core on macrophage evasion indicate a role for NP stiffness in this process. Soft poly(carboxybetaine) nanogels loaded with gold nanoparticles are shown to have up to 10 h difference in circulation half-life compared to harder NGs, i.e., 19.6 ±1.5 h and 9.1 ± 2.5 h, respectively.[28] Anselmo et al. investigated the effect of particle elasticity on blood circulation and –consequently- tissue targeting and showed that soft NPs circulated longer than hard NPs, especially at short times, which was attributed to their reduced uptake and clearance by the phagocytic system.[26] In contrast to making NPs that evade macrophages, macrophages can be exploited to bring (hard) NPs to tumor sites and improve therapeutic effect.[155, 165-169]

Here we investigated the effect of NP stiffness on the uptake and cytotoxicity in glioma cells and macrophages. To this end, poly-N-isopropylmethacrylamide (p(NIPMAM)) nanogels (NGs) with different cross-linking densities and sizes were incubated with C6 glioma cells and J774 macrophages in monoculture and co-culture. By tuning the cross-linking density of NGs the stiffness is modulated, where lower stiffness is associated with a lower elastic modulus i.e. a softer NG.

3.2 METHODS AND MATERIALS

3.2.1 Nanogel preparation and characterization

Nanogels were prepared according to procedure already reported in Chapter II, Section 2.2.1. Characterization was also performed as described in Chapter II, Section

2.2.2. For *in vitro* assays, NGs were autoclaved and resuspended in the appropriated medium with supplements.

3.2.2 Cell culture

C6 glioma cells from rat were cultivated in Dulbecco's modified Eagle medium high glucose (DMEM-HG) medium containing GlutaMAX™ and pyruvate (Gibco™, #31966021, LOT 2078361) supplemented with 7.5% FBS (v/v) and 1% penicillin-streptomycin (PenStrep; Gibco™, #15140-122). J774 cell line derived from murine reticulum cell sarcoma of *Mus musculus* was also cultivated in DMEM-HG medium supplemented with Glutamax^{TM}-I (Gibco^{TM}, #35050-038) and 10% (v/v) FBS. Coculture systems were prepared with 1:1 mixing ratio of C6 glioma cells and J774 macrophages and grow in media combination with 1:1 ratio of monoculture media.

3.2.3 Flow cytometry

Monocultures of C6 and J774 cells were prepared by seeding 1 x 10^5 cells per well in a 24 well plate and grown for 22 hours. Co-cultures were stablished by combining glioma C6 cells and macrophages J774 at a 1:1 mixing ratio. First, 4 x 10^5 macrophages per ml in cell suspension were stained with CellTracker™ Green CMFDA Dye (#C7025, Lot 461354, Invitrogen^{TM}) at 2 µmol l^{-1} in DMEM-HG supplemented with 10% (v/v) FBS and Glutamax^{TM}-I for 40 min at 37°C under moderated orbital shaking. Cells were washed twice with DMEM-HG medium by centrifugation at 500 g, 5 min. J774 cells without CellTracker were submitted to the same procedures except to the addition of CellTracker. Macrophages were seeded at 1 x 10^5 cells per well in a 24 well plate and incubated for 20 min at 37°C, 5% CO_2 in humidified incubator prior to addition of C6 glioma cells. C6 were seeded also at 1 x 10^5 cells per well in a 24 well plate in combination with the macrophages.

Following, covering medium was removed, cells were washed one time with 1X PBS and 50 µg of microgels were incubated per well at a concentration of 100 µg ml^{-1} in 1:1 ratio of C6 and J774 growth media. After 2 hours incubation (37C, 5% CO_2),

covering medium was collected in flow cytometry tubes, cells were washed twice with PBS and 200 ul of PBS containing 4 mg ml^{-1} lidocaine and 10 mM EDTA were incubated with the cells for up to 15 minutes. For uptake experiments, 200 µl of ice-cold 1x PBS supplemented with 2%(v/v) FBS and 5 mM EDTA (PFE) were added to each well, cells were detached by thoroughly pipetting and collected in the flow cytometry tubes. Wells were washed with 200 µl of PFE and also collected in the same tubes. Samples were centrifuged at 4°C, 500 g for 5 min twice and resuspended in PFE. Cells were kept on ice before being measured. NGs were detected

ROS assays were performed using live imaging solutions instead of PFE and were not kept on ice. Following centrifugation, cells were incubated with ROS indicator 2',7'-dichlorodihydrofluorescein diacetate (H_2DCFDA, Sigma-Aldrich, #D6883) at 1.1000 for 30 min. Data was analyzed using FlowJo V10 software (Tree Star, Inc.) and Origin 2020. Single-stained cocultures and monocultures were employed for compensation. Measurements were obtained using a CytoFlex S Flow Cytometer (Beckman Coulter) using the APC channel (670/30 band pass filter) and laser excitation 640 nm for NGs fluorescence detection and FITC channel (525/40 band pass filter) using laser excitation 488 nm to detect CellTracker-stained cells. Data was analyzed using FlowJo V10 software (Tree Star, Inc.) and Origin. Because different nile blue-labelled NGs do not have the same fluorescence, geometric mean was corrected according to the fluorescence of each microgel at 656 nm ($\lambda_{excitation}$ = 633 nm) at 100 µg ml^{-1} for comparison between NGs.[135]

3.2.4 Cell viability assay

C6 cells viability exposed to nanogels NG1.5, NG5, NG14 and $NG5^{large}$ was evaluated using 3-(4,5-dimethylthiazol-2-yl)-2,5-diphenyltetrazolium bromide (MTT, Sigma-Aldrich) assay. Cells were seeded into 96-wells plates at 5 x 10^3 cells per well and grown for 24 h at 37 °C, 5% CO_2 in humidified atmosphere before exposure to nanogels at concentrations at 10 to 1000 ng ml^{-1} for 24 h in DMEM-HG medium supplemented with 7.5% (v/v) FBS and 1% (v/v) Pen/Strep with 100 µl per well. After 24 h, medium containing NGs was removed and cells washed once with 1x PBS. 0.5 mg

ml^{-1} MTT solution (stock solution 5 mg ml^{-1} in 1x PBS) in DMEM-HG supplemented was incubated for 3 h at 37 °C, 5% CO_2. MTT-formazan crystals were dissolved in 100 µl dimethyl sulfoxide (DMSO) per well. Experiments were carried out in triplicate and compared to untreated cells. Absorbance was read using a Fluostar-Optima microplate reader (BMG Labtech).

3.2.5 Fluorescence microscopy

Fluorescence microscopy samples were prepared in 6-well plates with initial seeding of 1 x 10^5 cells per well for monocultures and 2 x 10^5 cells per well for coculture with the cell ratio 1:1 (C6:J774). Cells were allowed to attach and grow for 22 hours at 37°C, 5% CO_2 in humidified incubator. For coculture experiments, J774 cells were stained with CellTracker™ Green CMFDA Dye (#C7025, Lot 461354, Invitrogen^{TM}) at 2 µmol L^{-1} as previously described for flow cytometry assay. After 22 h, medium was removed and NGs incubated at 1 mg ml^{-1} with 2 ml per well for 24 h. NGs were removed, and cells were washed twice with 1x PBS and fixated with 3.7% paraformaldehyde (PFA) for 10 minutes. Following fixation, cells were incubated with 0.2% (v/v) Triton X-100 in 1x PBS for 3 minutes. Cells were washed with 1 x PBS thrice and 2 µg ml^{-1} DAPI in 1x PBS was incubated for 30 min. Again cells were washed twice with 1x PBS, samples were mounted with PBS:glycerol (50:50) and a cover slip was carefully placed over the cells for each well. Images were acquired using an inverted Leica DMI6000 B microscope (Leica Microsystems) and N PLAN 10x/0.25 DRY and HCX PL FLUOTAR L 40x/0.60 DRY objectives. Fluorescence filter cubes used were A4 for DAPI (BP 360/40; 470/40 nm), L5 for Celltracker (BP 480/40, BP 527/30) and Y5 (BP 620/60, BP 700/75) for the nanogels.

3.2.6 Confocal microscopy

Confocal microscopy was employed to assess cellular uptake of fluorescently labeled nanogels. Cells were seeded on coverslips and grown for 24 hours. Macrophages for co-culture were stained with CellTracker™ Green CMFDA Dye prior to

seeding as previously described. After 24 h, monocultures and co-cultures were exposed to NGs for 2 h and incubated with 2 µg ml^{-1} Hoechst during the last 30 min. Then, samples were fixated with 3.7% PFA, mounted with PBS:glycerol (50:50) and a cover slip was carefully placed over the samples. Images were collected using a Leica TSC SP2 confocal microscope and a 63x immersion oil objective and treated with Fiji.[134] Z slice images were collected sequentially using two or three channels and excitation lasers 488 (ArKr) and 633 nm (HeNe). Stacks were collected where each image is 512 × 512 pixels.

3.3 RESULTS AND DISCUSSION

3.3.1 Nanogel characterization

Nanogel properties and characterization are described in Chapter II.

3.3.2 Direct co-culture

Co-culturing cells helps to assess their natural behavior and even improves cultivation of certain cell types. As for nanomaterials interaction, co-cultures can more reliably mimic the natural system to evaluate nanomaterials performance under the combined influence of multiple cell types. According to the environment to be mimicked, different spatial arrangements can be employed that can be categorized in direct and indirect co-culture. In the indirect co-culture system, only the paracrine communication can be evaluated, while direct co-culture will allow to study paracrine communication and heterotypic interactions.

Concerning the presence of GAMs in the glioma TME, a direct co-culture between glioma cells and macrophages could mimic the *in vivo* conditions more accurately. To distinguish between macrophages and cancer cells, macrophages were stained with CellTracker™ Green CMFDA Dye, which is well retained by cells and can be traced through a number of generations.

Using flow cytometry, the populations were discriminated by gating fluorescence intensity (Figure 3.1) and the uptake of NGs was evaluated for each cell type. The macrophage population within the co-culture after 24 h growth and 2 h incubation with or without NGs treatment represented about 30% of the total cell population.

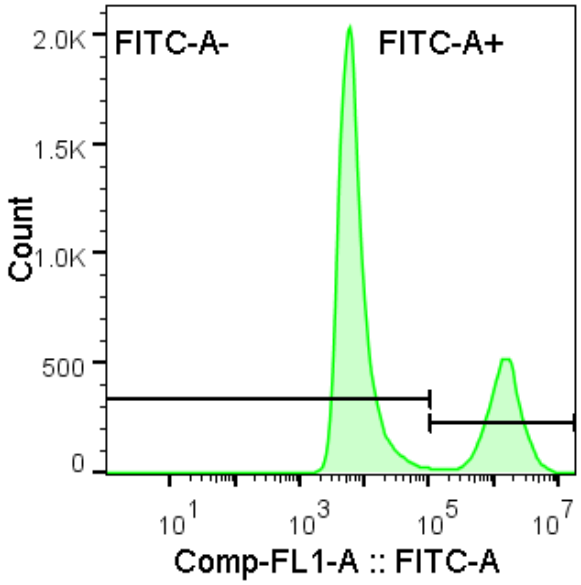

Figure 3.1 – Representation of cell population discrimination in direct co-culture of glioma cells and macrophages by gating fluorescence. C6 (glioma cells) and J774 (macrophages) populations were distinguished by staining the macrophages populations with CellTracker™ Green CMFDA Dye at 2 µmol L^{-1} in DMEM-HG supplemented with 10% (v/v) FBS and GlutamaxTM-I for 40 min at 37°C and gating fluorescence intensity. FITC-A- represents the C6 glioma cells population and FITC-A+, the J774 macrophages population.
Source: By the author

3.3.3 *In vitro* cellular uptake of nanogels in monoculture and co-culture

NG uptake was evaluated in direct co-culture of C6 glioma and J774 macrophages, as well as in monocultures using flow cytometry. Figure 3.2 shows the cellular uptake levels of p(NIPMAM) NGs of different cross-linking densities (NG1.5, NG5 and NG14) with C6 rat glioma cells (Figure 3.2A) and murine J774 macrophages (Figure 3.2B) monocultures. It is evident that the softer NGs, NG1.5 and NG5, are internalized to a lesser extent than the stiffer NG14 by both cell types. These findings are in accordance with literature reports for nanoparticles with similar properties in monocultures[26,126,129] and also with theoretical models.[39,130] Lower internalization of

softer NPs is caused by the reduction of plasma membrane bending that affects the wrapping process. However, bending variation between NG1.5 and NG5 appears not divergent enough to have an influence on NGs internalization levels. This can possibly be explained by the NGs stiffness variation, where NG1.5 elastic modulus is about 20 kPa and NG5 120 kPa, while NG14 is about 350 kPa, as reported in our earlier work.[133] The lower uptake of soft NPs by macrophages is an indication of longer blood half-life *in vivo* and often leads to increased accumulation in tissues. As reported by Anselmo *et al*., not only blood circulation was longer for soft particles, but also organ retention was enhanced, including brain accumulation. Because soft NPs remain at higher concentrations in the blood than hard NPs, even though significance was encountered only in short times, the organs with higher blood output are favored and show greater accumulation of soft particles.[26] In addition to NP clearance, NP transcytosis across the blood-brain barrier (BBB) is a great limiting factor to the treatment of central nervous system (CNS) disorders. Evasion strategies to escape the mononuclear phagocytic systems can increase the accumulation of particles at the BBB, although it does not guarantee the efficacy in transcytosis.[83,87,143]

When comparing particles of similar cross-linking densities but different sizes, NG5 and NG5^{large} (Figure 3.2C, D), the larger particles were internalized to a higher extent by macrophages (Figure 3.2D). Such behavior is consistent with literature for phagocytosis of particles, which describes maximum phagocytosis for particles between 1-3 µm. The phagocytic capability increases from smaller to larger particles up to 1-3 µm and this effect correlates with the NP propensity to attach to the cellular membrane.[170] Modeled by Derjaguin–Landau–Verwey–Overbeek (DLVO) theory, particle-membrane adhesion is dependent on surface roughness and particles in the optimal size range are able to establish more contact points than smaller or larger particles.[170-171] In addition, NP stiffness as well as size can indirectly influence NP internalization due to their influence on corona formation.[131-132, 144-145]

When the effect of stiffness and size were investigated in co-culture, the preference for uptake of the stiffer NGs and larger NGs remained (Figure 3.2C, D). However, if we compare the co-culture uptake levels with the levels in monoculture, only the uptake of softer NGs in macrophages presented significant changes (p-value <

0.05), showing higher uptake of soft NGs by macrophages under co-culture conditions. Macrophage populations are heterogeneous and traditional classification of macrophage polarization is M0, M1 and M2. In tumor microenvironments, M2 macrophages are correlated to tumor progression and M1 polarization to pro-inflammatory response. Tumor-derived factors like cytokines and growth factors can induce macrophage differentiation.[172-173] Stimulated macrophages exhibit greater phagocytic capacity than non-stimulated macrophages.[174-176]

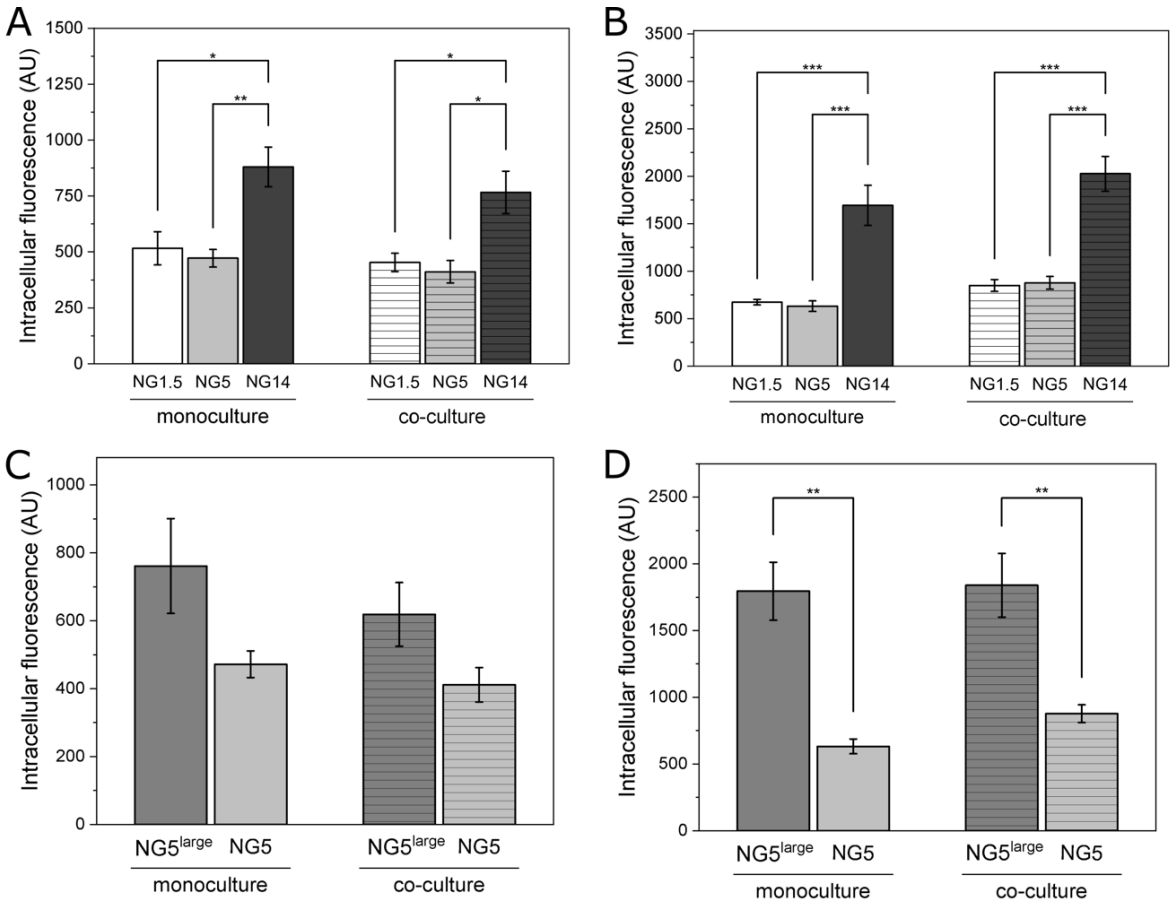

Figure 3.2 - Effect of NGs stiffness and size on the interaction with monoculture and co-culture of glioma and macrophages cells. NG1.5, NG5 and NG14 (stiffness effect) in A) C6 glioma cells in monoculture and co-culture with J774+ cells and, B) J774+ cells in monoculture and co-culture with C6 glioma cells. NG5 and NG5large (size effect) intracellular fluorescence levels evaluation in C) C6 glioma cells in monoculture and co-culture with J774+ cells and, D) NG5 and NG5large (size effect) intracellular fluorescence levels evaluation in J774+ cells in monoculture and co-culture with C6 glioma cells. C6 and J774+ cells were exposed to 50 µg (100 µg ml^{-1}) of nile-blue labelled nanogels NG1.5, NG5, NG5large and NG14 for 2 h at 37 °C, 5% CO2 and interaction was evaluated by flow cytometry. The intracellular fluorescence intensities were corrected by dividing the mean fluorescence intensity of the cells by the fluorescence intensity of the NG stock dispersions (100 µg ml^{-1}). Values are represented as mean ± SD of four independent experiments and each experiment was performed in duplicate. Data was analyzed using two-sample t-test and significances are indicated by * for p-value < 0.05, ** for p-value < 0.01 and *** for p-value < 0.001.

Source: By the author.

The evaluation of surface markers like CD163 and CD204, and cytokines like IL-10 is used for macrophage profiling and labels GAMs as M2 macrophages. However, microarray analysis of TMEs of gliomas suggests only a partial correspondence with the gene expression patterns of the M1 and M2 polarization states,[114,177] justifying the need of co-culturing cancer cells and macrophages to - at least partially - mimic the tumor environment response to therapeutics and nanomaterials.

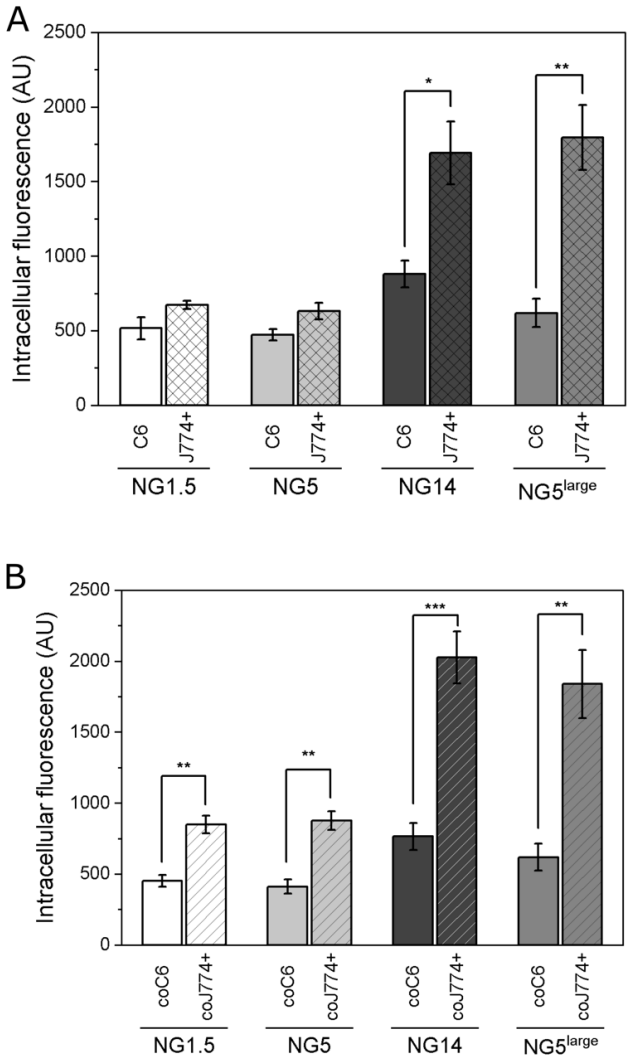

Figure 3.3 - Evaluation of NGs uptake in monoculture and co-culture of glioma cells and macrophages. Comparison between intracellular fluorescence of nanogels NG1.5, NG5, NG14 and NG5^{large} by C6 cells and J774 CellTracker™ Green CMFDA Dye-stained macrophages in A) mono (C6 and J774+) and B) co-culture (coC6 and coJ774+). 500 µl of a 100 µg ml^{-1} NGs dispersion were incubated for 2 h for uptake assessment. The intracellular fluorescence intensities were corrected by dividing the mean fluorescence intensity of the cells by the fluorescence intensity of the NG stock dispersions (100 µg ml^{-1}). Values are represented as mean ± SD of four independent experiments. Data was analyzed using two-sample t-test and significances are indicated by * for p-value < 0.05, ** for p-value < 0.01 and *** for p-value < 0.001

Source: By the author.

C6 glioma NG uptake levels were compared to NG uptake in J774 macrophages in mono- and co-culture (Figure 3.3A, B). The differences in NG uptake between the two cell types is more pronounced in co-culture with increasing differences as stiffness and size increase (1.9 (NG1.5), 2.2 (NG5), 2.7 (NG14) and 2.8-fold ($NG5^{large}$)), than in monoculture (1.3 (NG1.5), 1.3 (NG5), 1.8 (NG14) and 2.2-fold ($NG5^{large}$)). For the soft, the stiff and the large NGs the differences in uptake are statistically significant in the co-culture system, (Figure 3.3B), whereas for monocultures the differences in uptake are statistically significant only for the stiff and large NGs. (Figure 3.3A). Again, these results could be explained by a change in macrophage behavior due to the presence of glioma-derived factors that stimulate the J774 macrophages.

3.3.3 Nanogels stiffness has an impact on cell viability

Considering the uptake results for the NGs in both monoculture and co-culture conditions, we investigated the *in vitro* viability of C6 cells exposed to NGs by MTT viability assay. As shown in Figure 3.5A, B, NGs toxicity is concentration, stiffness and size-dependent. A substantial reduction in cell viability was observed at 500 and 1000 μg ml^{-1} for the softer smaller nanogels, NG1.5 and NG5, as supported by the fluorescence microscopy images in Figure 3.4C.

To compare the toxic response of C6 glioma cells and J774 macrophages (in monoculture) toward NGs, cells were exposed to 2 mg of NGs at 1 mg ml^{-1} in 6-well plates for 24 hours at 37 °C, 5% CO_2. Figure 3.5 clearly shows that NG1.5 had a toxic effect, especially on C6 glioma cells and, to a lesser extent, on J774 macrophages. NG1.5 virtually killed all the cells. It should be highlighted that although the internalization of the harder NGs was more pronounced, it did not lead to a higher cytotoxicity. The results indicate a more toxic effect of especially soft NGs towards glioma than to macrophages.

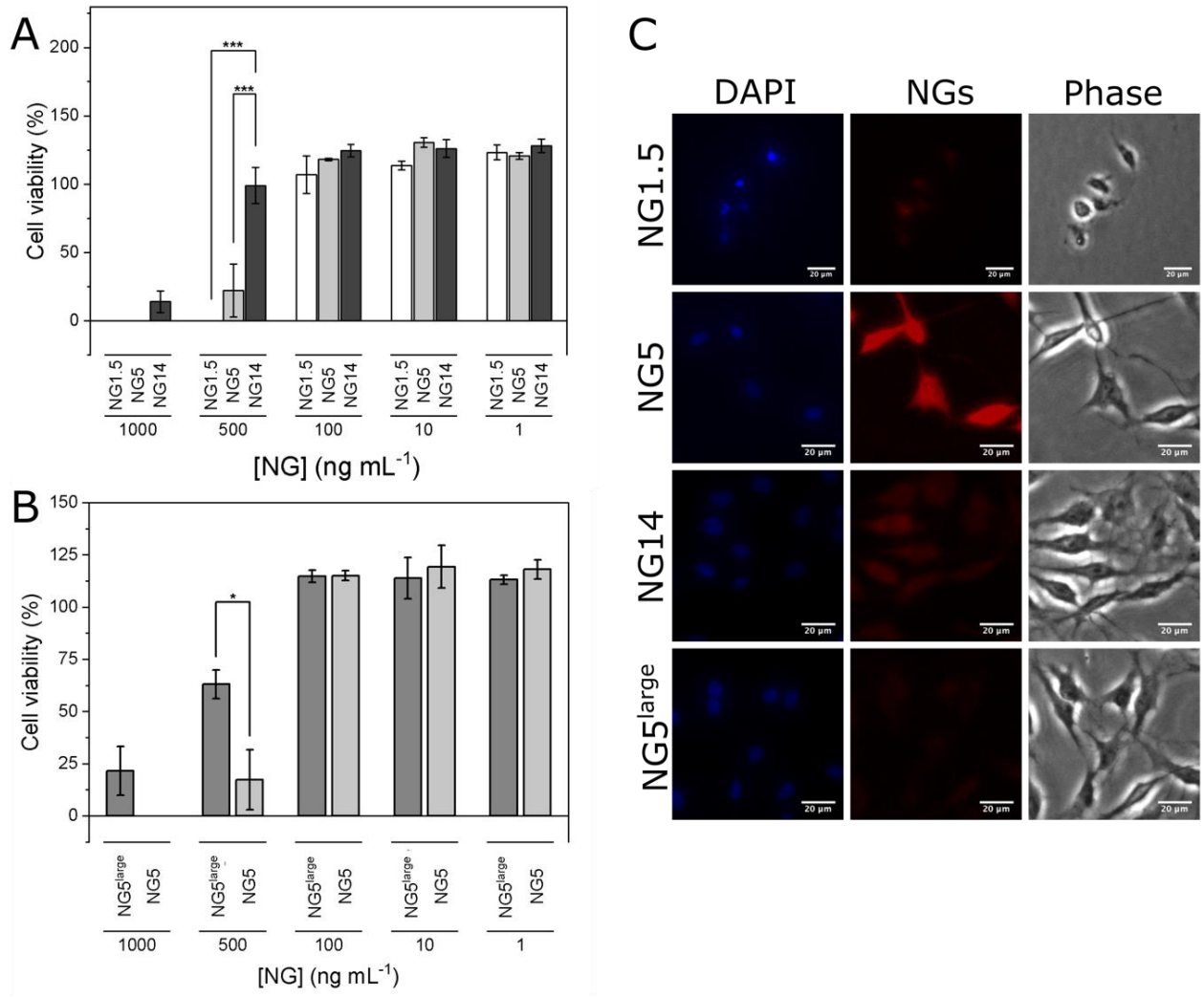

Figure 3.4 – Glioma cells response to p(NIPMAM) NGs stiffnesses and size. Cell viability evaluation by colorimetric MTT viability assay of C6 glioma cells exposed to nanogels with A) different cross-linking density, NG1.5, NG5 and NG14, and B) different sizes, NG5 $NG5^{large}$ for 24 hours at 37 °C, 5% CO_2. C) Toxicity assessment of C6 glioma cells by fluorescence microscopy exposed to 1 mg ml^{-1} of NG1.5, NG5, NG14 and $NG5^{large}$ for 24 hours at 37 °C, 5% CO_2. Nuclei were stained with 2 µg ml^{-1} DAPI for 30 min and images were acquire with and HCX PL FLUOTAR L 40x/0.60 DRY objective. Values are represented as mean ± SD of three independent experiments and each experiment was performed in triplicate. Data was analyzed using two-sample t-test and significances are indicated by * for p-value < 0.05 and *** for p-value < 0.001. Bars: 20 µm.

Source: By the author.

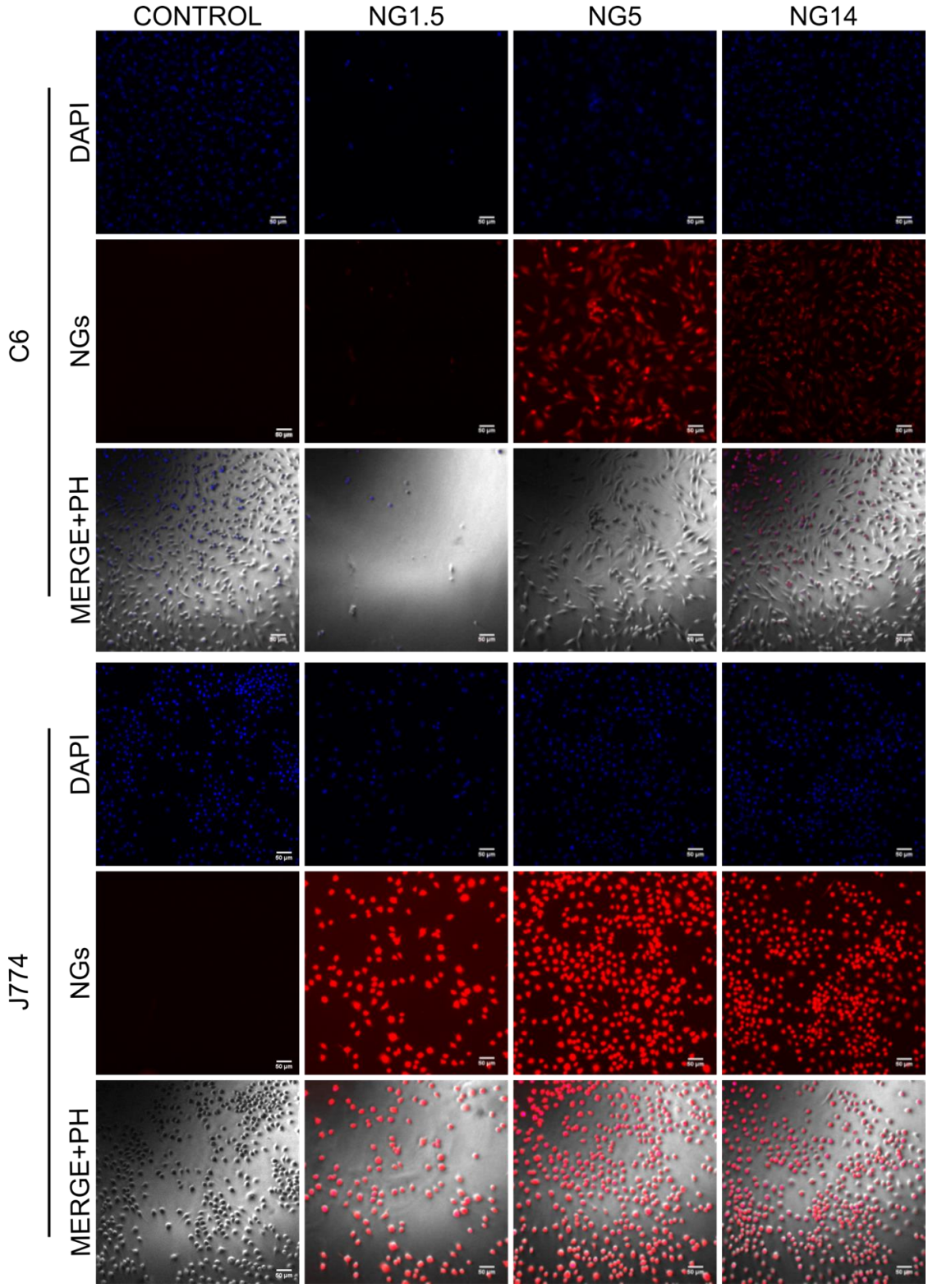

Figure 3.5 - Monocultures response to NGs stiffness. Fluorescence microscopy of monocultures of A) C6 glioma cells and B) J774 macrophages after exposed to NG1.5, NG5, NG14 and NG5^{large} for 24 hours at 1 mg ml^{-1}. Images were acquired with and N PLAN 10x/0.25 DRY objective and nuclei are stained with DAPI. Bars: 20 µm.

Source: By the author.

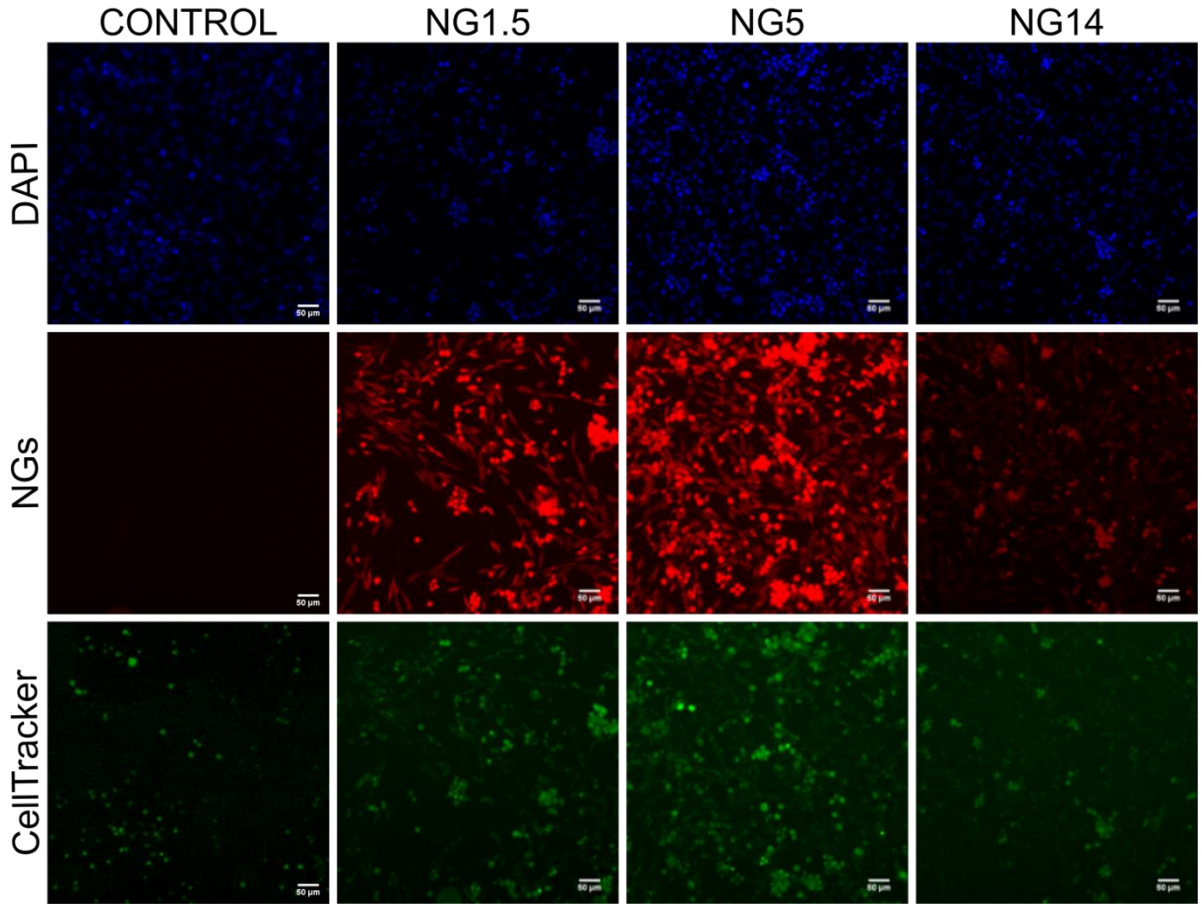

Figure 3.6 - Fluorescence microscopy of co-culture of C6 glioma cells and J774 macrophages after exposed for 24 h to NG1.5, NG5 and NG14. Nuclei are stained with DAPI and macrophages were stained with CellTracker™ Green CMFDA Dye. NGs were labelled with nile blue, although the fluorescence intensity is not the identical among them, where NG1.5 shows the higher intensity followed by NG5 and NG14. Scale bar: 20 µm.
Source: By the author.

Figure 3.6 displays the toxic response of softer NGs towards C6 glioma cells in co-culture with J774 macrophages. The uptake of NGs by C6 cells in co-culture did not show significant variations compared to the uptake in monoculture. It was therefore expected that the cytotoxic effect of the soft NGs against C6 glioma cells was also unaffected. However, the fluorescence and optical microscopy images (Figure 3.6 and Figure 3.7) reveal an improved survival of the cancer cells when they are combined in direct co-culture with the macrophages. In optical microscopy images of C6 cells as monoculture, the round-shaped bodies are injured cells that detached from the plate, and which were removed with the medium containing the nanogels upon processing the samples for investigation by fluorescence microscopy.

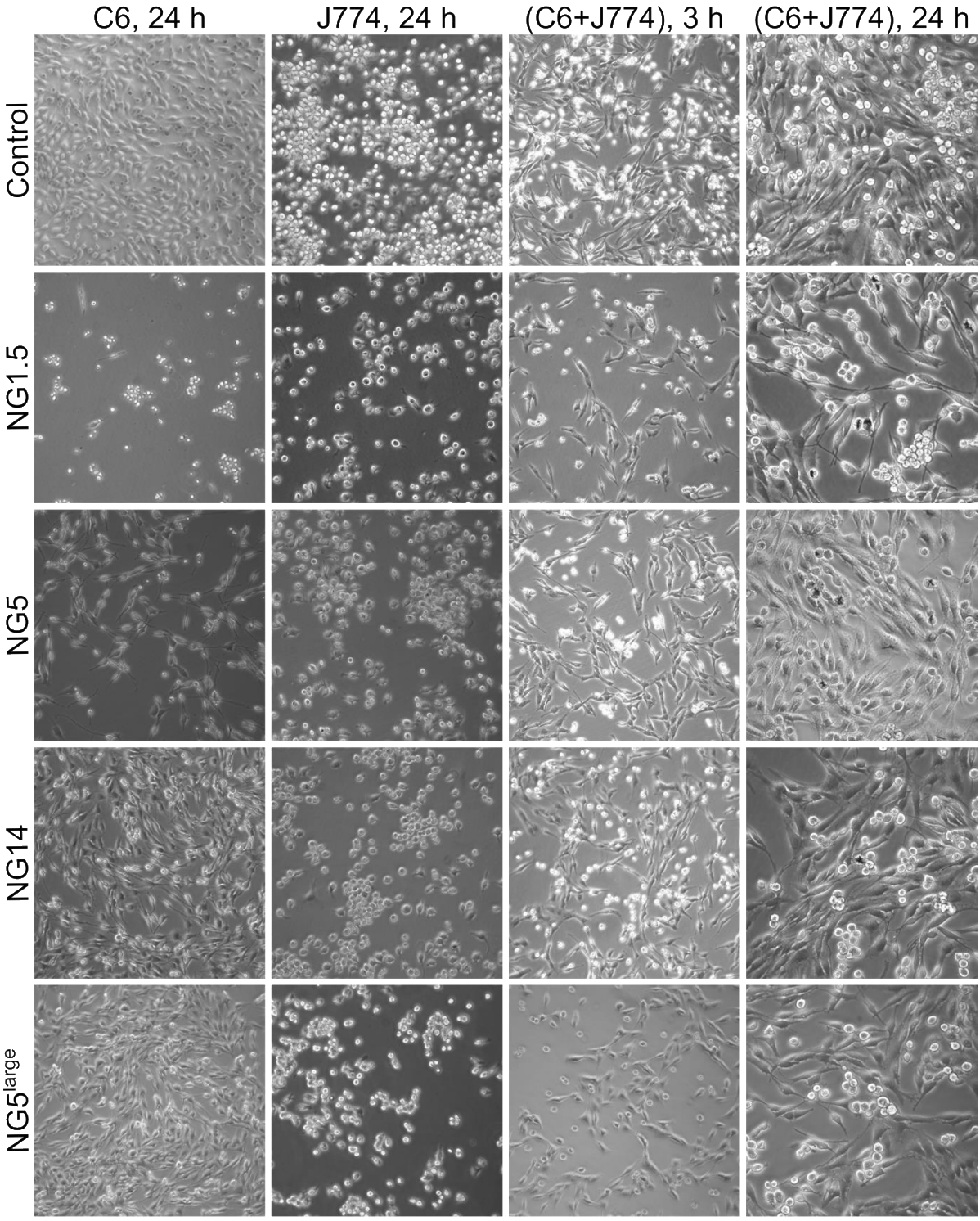

Figure 3.7 – Optical microscopy of monocultures of C6 glioma cells, J774 macrophages and co-culture of C6 and J774 cells after exposed for 24 hours to NG1.5, NG5, NG14 and $NG5^{large}$ in 6-well plates. First row are the cells without exposure to NGs.

Source: By the author.

It has been reported that tumor-associated macrophages alter the toxic activity of several compounds and nanoparticles.[156,178-181] This has been attributed to the

upregulation of scavenger receptors and ROS-scavenging enzymes in macrophages in the presence of tumor cells, which lowers the stress level in the tumor cells, thus promoting tumor progression.[182-183]

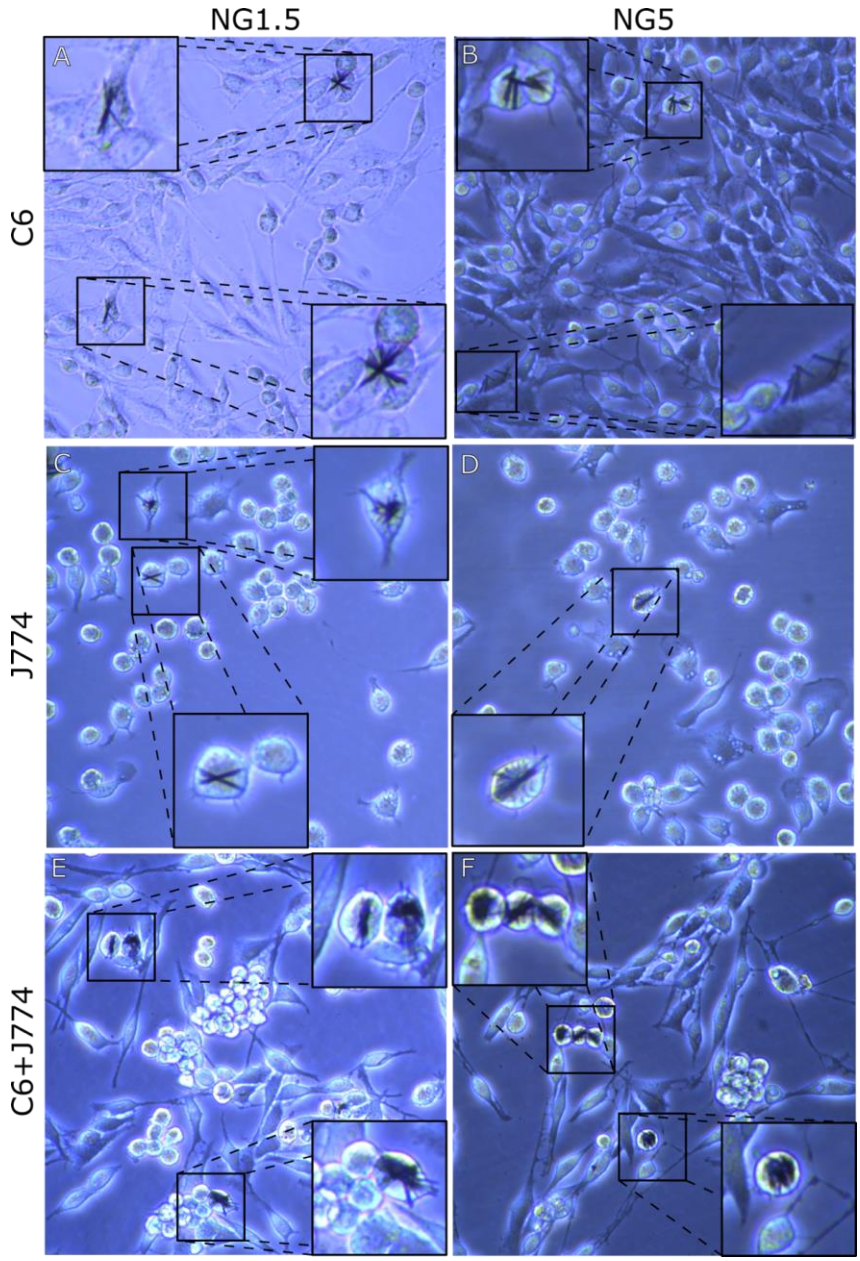

Figure 3.8 – Crystal formation in the presence of NG5 and NG1.5 nanogels. Optical microscopy of monocultures of C6 glioma cells exposed to 500 µg ml^{-1} of A) NG1.5 and B) NG5 for 24 h and of J774 macrophages 500 µg ml^{-1} of C) NG1.5 and D) NG5 for 24 h. Optical microscopy images of co-culture of C6 and J774 cells after exposed for 24 hours to 1 mg ml^{-1} E) NG1.5 and F) NG5.

Source: By the author.

Furthermore, in optical microscopy analysis, needle-shaped crystal formation was identified in mono and co-culture conditions upon incubation with soft NGs (Figure 3.8).

Crystal formation is linked to ROS induction in diverse diseases, including cancer.[184-187] Overall, after exposure of C6 glioma cells and J774 macrophages in monoculture and co-culture to soft NGs, we detected the appearance of crystals, as well as round-shaped bodies and cell debris, which might indicate apoptotic events (Figure 3.7 and 3.8).

By laser scanning confocal microscopy, we detected few multinucleated macrophages in the macrophage monocultures in response to the softer NG1.5. A representative image of a multinucleated cell is shown in Figure 3.8. The agglomeration of macrophages could be related to a well-known feature of the foreign body reaction, i.e., the formation of multinucleated giant cells (MGCs) by the fusion of macrophages.[188] MGC formation is a commonly reported reaction towards implanted 'foreign' materials and is often associated with the rejection of the material due to rigorous phagocytic activity to engulf the material for degradation.[189] Before fusion, the macrophages try to degrade the material through the production of reactive oxygen species (ROS) and enzymes.

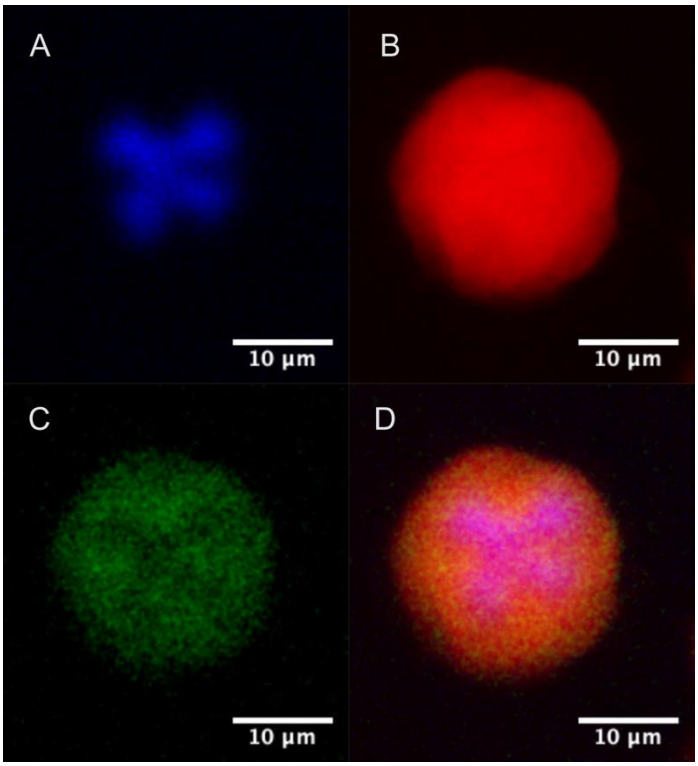

Figure 3.9 – Confocal images of multinucleated macrophage J774 cell. A) Hoechst staining, B) NGs, C) Lysotracker (lysosomes and late endosome staining) and D) Merge of A, B and C.
Source: By the author.

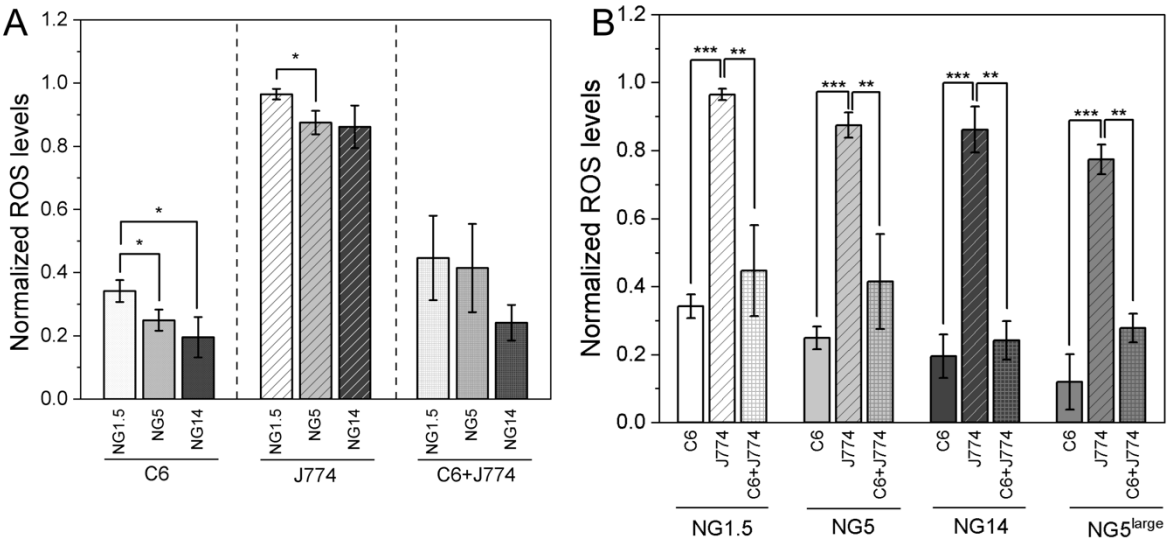

Figure 3.10 – Intracellular ROS generation by NGs in monoculture and co-culture. A) Evaluation of ROS production by NGs with different stiffness, NG1.5, NG5 and N14 in monoculture of C6 and J774 and co-culture of C6 and J774. B) ROS generation in monoculture and co-culture conditions due to NGs response. Cells were treated for 2 h with 50 µg (100 µg ml^{-1}) at 37 °C, 5% CO_2. Data was analyzed using two-sample t-test and significances are indicated by * for p-value < 0.05, ** for p-value < 0.01 and *** for p-value < 0.001.
Source: By the author.

Next, we investigated the ROS response of C6 glioma cells and J774 macrophages to incubation with NG1.5, NG5, NG14. Figure 3.10A shows that ROS production in C6 glioma cells is inversely correlated with NG stiffness, showing highest ROS production in the presence of the softest NG. ROS has quite paradoxical effects in cancer cells. Whereas an increase in ROS production stimulates cancer initiation and tumor progression, several chemotherapeutic agents are known ROS-inducers and –conversely- inhibit cancer growth. The idea is that these chemotherapeutics elevate the intracellular levels of ROS in (already stressed) cancer cells and tip the balance to the point where ROS inflicts damage to DNA, lipids, carbohydrates, and proteins causing cell death.[190-192] The ROS levels in C6 glioma cells upon incubation with the different NGs correlate with the levels of cytotoxicity, showing highest ROS generation and cytotoxicity for the softest NG. As expected, ROS production in macrophages was higher than in glioma cells, although the toxic effect was lower. This can be explained by adaptive mechanisms that allow the macrophages to survive to increased stress.[193-194]. Interestingly, the ROS levels in co-culture were severely reduced compared to the monoculture of macrophages (Figure 3.10B) This may explain for the reduced NG-

induced toxicity in C6 glioma cells in co-culture conditions, suggesting a cytoprotective effect of the presence of macrophages on C6 glioma cells incubated with NGs. Unfortunately, we could not discriminate between ROS generation in macrophages and C6 cells in the co-culture, because of an overlap in the fluorescence spectra of the CMFDA cell tracker dye, that we used to label the macrophages, and the ROS indicator H_2DCFDA.

3.4 CONCLUSION

The use of co-cultures to better mimic the interplay of different cell types in the *in vivo* tumor environment can help to predict the behavior of nanomaterials in the *in vivo* biological context, to predict treatment efficacy. Here we focused on an important cell type in the glioma microenvironment, the peripheral macrophages.[195] Using monocultures and a co-culture of glioma cells and macrophages we were able to determine differences in cell behavior in response to nanomaterials, specifically p(NIPMAM) nanogels of different stiffness and size. Stiffer NGs (NG14) were more internalized compared to the softer ones (NG5 and NG1.5) by both cell types, most likely as a response to enhanced cellular membrane bending and wrapping kinetics. In addition, distinct corona profiles on the different NGs may have influenced NG uptake kinetics, of which the possible relation with particle stiffness requires further exploration.[39-40,131-132,138,144-145] Generally, soft particles evade phagocytic cells and consequently would offer longer blood half-life, contributing to accumulation in organs with higher blood demand.[26] As soft NGs were taken-up less by the macrophages, we have an indication of lower clearance of those particles by the MPS. Additionally, higher levels of transcytosis were achieved by softer NGs in our previous work, as described in Chapter 2 of this thesis.

In addition, we found that NG-induced cytotoxicity in C6 glioma cells was dependent on the stiffness of NGs, and correlated with intracellular ROS levels. The softest NGs induced the highest ROS levels and most pronounced cytotoxicity. Moreover, we analyzed the effect of NGs with different hydrodynamic diameters and concluded that the larger NGs, $NG5^{large}$, were internalized more efficiently than the

smaller NG5 by both macrophages and glioma cells. We hypothesize that larger NGs may be advantageous for CNS disorder therapies targeting macrophages since we did not observe a significant alteration in transcytosis level between NG5 and NG^{large}.[169]

In the direct co-culture system, a significant increase in uptake of NG1.5 and NG5 by macrophages was observed compared to monoculture. Furthermore, the co-culture environment led to a reduction in toxicity towards C6 glioma cells, as determined by cell morphological investigation by fluorescence and optical microscopy. Combined ROS levels of C6 and J774 macrophages in direct co-culture were radically reduced when compared with ROS levels of J774 macrophages in the monoculture. This reduction indicates a possible effect on the macrophage phenotyping and behavior towards the presence of C6 glioma cells, which augments the importance of exploring co-culture systems to better mimic the *in vivo* condition and predict the *in vivo* fate of nanomaterials.

4 CHAPTER IV: EPITHELIAL CANCER-CELL MEMBRANE COATED PLGA NANOCARRIERS ENHANCED UPTAKE LEADS TO MORE EFFECTIVE CANCER TREATMENT

Authors: Laís Ribovski;[1,2] Paula M. P. Lins;[2] Bruna Juliana Moreira;[2] Luana Corsi Antônio;[2] Juliana Cancino-Bernardi;[2] Valtencir Zucolotto*[2]

[1]University of Groningen, University Medical Center Groningen, Department of Biomedical Engineering, Groningen, the Netherlands. A. Deusinglaan 1, 9713 AV Groningen, The Netherlands

[2]Nanomedicine and Nanotoxicology Group, Physics Institute of São Carlos, University of São Paulo, CP 369, 13560-970 São Carlos, SP, Brazil

*Corresponding author: Valtencir Zucolotto

E-mail address: zuco@ifsc.usp.br

ABSTRACT

Nanomaterials applied to medicine have been showing great potential and offer innovative strategies to the diagnosis, prevention, and treatment of several pathologies. Cancer is one of the areas explored by nanomedicine, especially by the use of nano-sized carrier systems to the delivery of therapeutics. However, targetability and efficacy still requires improvement to enhance treatments. This chapter describes the development of cancer cell membrane-coated poly lactic-co-glycolic acid (PLGA) nanocarriers (NCs) containing paclitaxel (PTX), a chemotherapeutic drug. We take advantage of the homotypic adhesion between cancer cells to improve treatment effectiveness. Membranes of breast cancer cells (MCF-7) were extracted by hypotonic treatment and coating process was performed by ultrasonication. Cellular uptake in MCF-7, lung cancer cells (A549), and non-tumorigenic breast cells (MCF-10A) was studied by flow cytometry and confocal microscopy revealing that (MCF-7)-membrane-coated PLGA NCs interaction is increased in all cell types but more significant in MCF-7. We evaluated the influence of the PLGA NCs containing paclitaxel (PLGA-PTX NCs) with and without membrane coating on cell viability and observed a considerable reduction of MCF-7 cells viability when interacting with the (MCF-7)-membrane-coated PLGA-PTX NCS (mPLGA NCs).

Keywords: nanoparticles, drug delivery, cancer cell membrane coating, cancer.

4.1 INTRODUCTION

Poly lactic-co-glycolic acid (PLGA) nanocarriers (NCs) are well known delivery systems due to their biocompatibility, biodegradability, and versatility. Even though these nanocarriers show enhanced delivery efficacy compared to free compounds, their outcome still needs to be improved. Many methodologies target enhanced specificity by using the permeability and retention effect (EPR) and adhesion between nanomaterials in which the cell membrane has been explored as a property to control nanoparticle uptake.[196-197] Particle functionalization with targeting ligands is a widely applied strategy which improves adhesion, in particular, overexpressed genes are targeted to achieve enhanced specificity.[198-199] Adhesion also plays an important role in tumor progression and metastasis. Those variations in adhesion, commonly regulated by variations in gene expression, allow for the detachment of malignant cells and attachment to a new site, generating secondary tumors.[200-201]

Cell membrane-coated NCs are an emerging platform addressing the development of specific targeted treatments. The cellular membrane material can be obtained from a range of sources such as, immune cells,[202] stem cells,[203-204] red blood cells,[205-207] and cancer cells.[6,108, 208] Each source will bring an advantage associated with their membrane properties and composition. Membrane extracts can be derived from a series of processes including hypotonic or hypotonic lysis, a treatment commonly followed by mechanical disruption and ultracentrifugation, freezing-thawing also combined with centrifugation. The methodology usually will depend on the cellular type. After extraction and isolation, the nanoparticles can be coated with cell membrane by different methodologies, in particular, ultrasonication, and membrane nanoparticles coextrusion.[209-210]

Cancer-cell-biomimetic nanocarriers benefit from the homotypic cell adhesion between cancer cells to improve nanoparticle adhesion at the cancer site and consequently, NCs internalization is favored.[108] Hu and colleagues were among the first to show that polymeric nanoparticles coated with red blood cells have a longer blood circulation time than those coated with PEG.[211] Additionally, Fang et al. showed that the coating of PLGA nanoparticles with cell membranes derived from B16–F10 melanoma

cells allows to deliver tumor associated antigens or homotypically target cancerous cells.[108]

Here we focus on breast cancer, still one of the most diagnosed cancer among women.[212] We propose the use of PLGA nanocarriers containing a chemotherapy drug paclitaxel, with MCF-7 cancer cell membranes, a cell line derived from an invasive breast ductal carcinoma. The interaction of dye-loaded PLGA, and membrane-coated dye-loaded PLGA NCs (mPLGA NCs) with cancerous and non-cancerous epithelial cells lines was studied using flow cytometry and confocal laser scanning microscopy (CLSM). Our study revealed higher levels of interaction of mPLGA NCs for all cell types showing not only homotypic adhesion with the source cancer cell but also with non-cancerous breast cells and lung cancer cells. To assess the mPLGA NCs potential as a treatment for cancer, cell viability was tested for those same cells with systems containing paclitaxel. We anticipate that the mPLGA-PTX NCs improve NCs specificity and efficacy against the breast cancer cell, but not against lung cancer and non-tumorigenic breast cell lines.

4.2 MATERIALS AND METHODS

4.2.1 Preparation of PTX-loaded and dye-loaded PLGA nanocarriers

PLGA nanocarriers were prepared by the nanoprecipitation method with solvent evaporation as described in literature by Fessi et al. with some modifications.[46] Briefly, 160 µl of 5 mg ml^{-1} PTX (0.8 mg) in acetonitrile were added to 2 ml of a 10 mg ml^{-1} PLGA (Resomer 503H 50:50 MW 24000-38000, acid terminated, #719870, Sigma-Aldrich) solution prepared in acetone and it was kept under magnetic stirring at room temperature. 6 ml of a 10 mg ml^{-1} Pluronic®-F127 (#P2443, Sigma-Aldrich) were added at once to the organic phase still under magnetic stirring (700 rpm). Following up to 5 minutes of magnetic stirring, acetone was evaporated under reduced pressure. NCs were centrifuged prior use and resuspended in the appropriated solvent according to use.

Nile red (NLR, #N3013, Sigma-Aldrich), fluorescein (#F2456, Sigma-Aldrich) or curcumin-loaded NCs were similarly prepared but instead PTX, 500 µg of nile red or 1 mg of fluorescein dissolved in acetone were added to the organic phase containing the polymer. As for curcumin-loaded NCs, 2 mg of curcumin dissolved in DMSO were mixed with the organic phase. After evaporation under reduced pressure, the NLR and curcumin-loaded NCs were centrifuged (10000 g, 20 min, 15 °C), resuspended in ddH_2O and placed in dialysis for 2 days, also in ddH_2O, using a dialysis membrane (14kDa cutoff, #D9277, Sigma-Aldrich). Following dialysis, the dispersion was collected, centrifuged and resuspended in 1 x PBS. These particles were employed to obtain the confocal images and flow cytometry experiments. Blank nanocarriers (PLGA NCs) were prepared by the same procedure as described above except by the addition of the drug or dye to the organic phase. Any variations of the procedure are clearly described.

4.2.2 Cell lines and cell culture

Breast cancer (MCF-7) and adenocarcinomic human alveolar basal epithelial (A549) cells were culture in Dulbecco's Modified Eagle Medium (DMEM, Vitrocell or Gibco #21885025) with 10 %(v/v) FBS. MCF-10A cells, a non-tumorigenic epithelial cell line, were cultivated in MEBM^{TM} Mammary Epithelial Cell Growth Basal Medium (MEBM, Lonza, #CC3151) supplemented with 100 ng ml^{-1} cholera toxin (#C8052, Sigma-Aldrich) and MEGMTM Mammary Epithelial Cell Growth Medium SingleQuotsTM Kit (Lonza, #CC4136) at 37 °C in a humidified atmosphere with 5% CO_2. For confocal samples MCF-10A cells were cultivated in DMEM/F12 (#11330-032, Thermo Fisher) supplemented with 5 %(v/v) horse serum (HS, #16050122, Thermo Fisher), 20 ng ml^{-1} epidermal growth factor (EGF, Peprotech), 0.5 mg ml^{-1} hydrocortisone (#H0888, Sigma-Aldrich), 100 ng ml^{-1} cholera toxin (#C8052, Sigma-Aldrich), 10 µg ml^{-1} insulin (#I1882, Sigma-Aldrich) and 1 %(v/v) penicillin/ streptomycin.

4.2.3 Cell membrane isolation

Cell membranes were isolated from MCF-7 breast cancer cell line cultivated in DMEM low glucose medium supplemented with 10% (v/v) FBS and 1% (v/v) Penicillin-

streptomycin. At confluence, the cells were detached from the flask by trypsinization and 0.5-1x10^7 cells were collected and washed twice with PBS (300 g, 5 min). Then, the pellet was resuspended in hypotonic buffer (10 mM Trisbase, 10 mM NaCl, 1.5 mM $MgCl_2$, pH 6.8) and incubated for 5 min at 4 °C followed by centrifugation at 300 g for 5 min. Supernatant was discarded and lysis buffer (0.255 M sucrose, 20 mM HEPES, 1 mM ethylenediaminetetraacetic acid disodium salt (EDTA), pH 7.4) was added to the cells. To separate cell debris from membrane, the extract was centrifuged at 10000 g for 20 min at 4 °C. Pellet was discarded and supernatant was spun down at 100000 g for 130 min at 4 °C using an ultracentrifuge Optima MAX-XP (Beckman Coulter, USA) or a in TLA100.3 rotor at 4 ºC. Cell membrane was suspended in 1x PBS containing 1:100 protease inhibitor cocktail (Sigma-Aldrich #8340) or SIGMAFAST™ protease inhibitor cocktail tablets according to product specifications (Sigma-Aldrich #S8830). For short-term storage, membrane extract was kept at 4 °C and for long-term storage at -80 °C.

4.2.4 PLGA-PTX and PLGA-dye NCs coating with MCF-7 cells membrane extract

Nanocarriers coating was performed by sonication. First, PLGA NCs were centrifuged (10000 g, 20 min, 15 °C), resuspended in 1x PBS followed by 15 min sonication. Cell membrane extract was also sonicated for 15 minutes. Thereafter, cell membranes and PLGA NCs were mixed to dilute the NCs 10 times from the stock and sonicated for more 15 min (See Table 4.1). Size, distribution and zeta potential (ζ-potential) of all NCs and membrane extract were evaluated using Zetasizer Nano ZS, Malvern. To estimate the number of particles per ml as well as particle size distribution, Nanoparticle Tracking Analysis (NTA) was performed using a Nanosight NS300, Malvern.

4.2.5 Transmission electron microscopy and cryogenic transmission electron microscopy

For transmission electronic microscopy (TEM), 3 µl of each sample was deposited on copper grids for 60 s and dried with filter paper. Samples were stained with

3 µl of 2% uranyl acetate for 30 seconds and again dried with filter paper. Cryogenic transmission electron microscopy CryoTEM samples were prepared by depositing 3 µl of the sample on a copper grid, the excess was dried for 3 s with filter paper and the grid was dipped in liquid ethane. The procedure was performed by Vitrobot Mark, Thermo Fischer. The images were obtained in JEOL 1400, in LNNano/CNPEM facilities, and JEM-2100 Transmission Electron Microscopes.

4.2.6 Scanning electron microscopy (SEM)

Field-emission Scanning Electron Microscopy (FE-SEM) was employed to observe NCs size distribution and morphology. Samples were prepared by drop-casting PLGA-PTX NCs diluted in ddH_2O onto clean silicon substrates and dried under reduced atmosphere. Images were collected using a ZEISS SIGMA VP field emission scanning electron microscope (FE-SEM).

4.2.7 Fourier-transform infrared spectroscopy (FTIR)

Fourier-transform infrared spectroscopy (FTIR) was used to analyze the differences in functional groups present in NC coated and non-coated with cell membrane extract. Samples were prepared by drop-casting copolymer PLGA, nonionic surfactant Pluronic®-F127, blank PLGA NCs, PLGA-PTX NCs and MCF-7 membrane coated PLGA-PTX NCs diluted in PBS 1x and ddH_2O onto clean silicon substrates and dried under reduced atmosphere. 128 scans were collected per sample with 4 cm^{-1} resolution from 4000 to 400 cm^{-1} using an Infrared spectrometer Nicolet 6700/GRAMS Suite.

4.2.8 High-performance liquid chromatography (HPLC) for paclitaxel quantification

Encapsulation efficiency (EE) was determined by HPLC. Samples were analyzed in a Waters® e2695 HPLC system equipped with the 2489 UV-Visible detector using a Brownlee Analytical C8 (150 x 4.6 mm, 5 µm) and precolumn Brownlee Analytical C8

(10 x 4 mm, 5 µm) from PerkinElmer. Mobile phase was composed of (50:50, v/v) acetonitrile and ddH_2O and flow rate was 1 ml min^{-1}. Quantification was performed by UV detection at 227 nm at 30 °C. Method validation was performed according to the International Council for Harmonisation of Technical Requirements for Pharmaceuticals for Human Use (ICH) Q2(R1) guidelines by the European Medicines Agency (EMEA) analyzing linear range, quantification limit (LOQ), precision, accuracy, selectivity and robustness.

Linear range and limit of quantification

Calibration curves were acquired using 5 concentrations of the reference standard (#Y0000698, Sigma-Aldrich) obtained by plotting the integrated peak area vs paclitaxel concentration from 0.5 to 25 µg ml^{-1}. The limit of quantification (LOQ) was determined by equation (Equation 4.1)

$$LOQ = \frac{10\sigma}{a} \tag{4.1}$$

where σ is the standard deviation of linear coefficient and a is the slope from 3 analytical curves.

Precision, accuracy and system suitability test

Precision and accuracy were evaluated for the same day (repeatability, intra-day) and for 3 distinct days (inter-day). Precision is determined by the percent coefficient of variation (CV%) (Equation 4.2)

$$CV\% = \frac{SD}{Mean} \tag{4.2}$$

SD is the standard deviation and $Mean$ is the average values of the calculated concentrations from standard curve.

Accuracy was calculated by the error's percentage to the nominal concentration by Equation 4.3

$$ER\% = \frac{Experimental\ concentration - nominal\ concentration}{nominal\ concentration}\ x\ 100 \qquad (4.3)$$

As for the system suitability, 10 injections were performed for a 10 µg ml^{-1} samples under the previously describe conditions evaluating retention time and integrated-peak area. Additionally, the method robustness was tested by changing temperature, flow rate and mobile phase composition.

PLGA NCs and PLGA-PTX NCs sample preparation for paclitaxel quantification and HPLC method validation

A volume of NCs dispersion was ultracentrifuged (100000 g, 120 min, 4 C) in a Beckman Coulter Optima L-90k, rotor SW32. Supernatant was carefully removed from the tube, the pellet was resuspended in the same volume of acetonitrile. 100 µl was transferred to a new tube and acetonitrile was evaporated under dry nitrogen stream. The sample was resuspended in 1 ml of starting mobile phase (50:50 acetonitrile:ddH_2O) and filtered with 0.22 µm pore-size nylon filter. Three batches (n=3) were used to determine encapsulation efficiency in quadruplicate as follows

$$EE(\%) = \frac{amount\ of\ PTX\ in\ NCs}{(amount\ of\ PTX\ in\ NCs + amount\ of\ free\ PTX)}\ x\ 100 \qquad (4.4)$$

Selectivity and stability in matrix

To assess method selectivity, samples of PLGA NCs, PLGA-PTX NCs and PTX were prepared as previously described and their chromatograms compared to investigate the effect of the presence of interferents, in this case the NCs composition besides PTX. Those samples were also used to analyze the stability of the method in

matrix by comparing the slope of standard curves obtained from samples containing only PTX and samples containing processed PLGA-PTX NCs.

4.2.9 Cellular uptake studies by flow cytometry

Non-coated PLGA NCs and MCF-7 cell-membrane coated PLGA NCs containing curcumin as probe were used to study the effect of the membrane coating in the NCs interaction with MCF-7, A549 and MCF-10A cells. In 24-well plates, $2x10^5$ cells were seeded and grown for 20-24 hours. Medium was removed and cells washed one time with 1X PBS followed by the incubation of $5x10^{10}$ NCs containing curcumin. Incubation times were 2, 4 and 24 h for MCF-7 cells, 2 h and 4 h for A549 cells and 4 h for MCF-10A cells. After incubation, medium was removed, and cells washed twice with 1X PBS and detached by trypsinization. Samples were collected and centrifuged (500 g, 5 min). Finally, cells were resuspended in Sheath Fluid (#342003 BD FACSFlow™, BD Bioscience) supplemented with 0.5% (w/v) bovine serum albumin (BSA, Fluka #05411) and kept on ice prior flow cytometry measurements. All measurements were performed in a BD FACSCalibur™ equipped with one laser (488 nm) and excitation measured using channel FL1 (530/30). Data analysis was performed using FlowJo V10 software (Tree Star, Inc.) and Origin 2020.

4.2.10 Confocal laser scanning microscopy

MCF-7 and MCF-10A interaction with coated and non-coated NCs was observed using a confocal laser scanning microscopy (CLSM). Cells were incubated in eight-well LabTek® chamber slide (Nalgene Nunc International) at initial seeding of $1x10^4$ cells per chamber and grown for 20 hours at 37 °C, 5% CO_2. Prior to incubation, cells were washed once with 1X PBS and $5x10^{10}$ NCs were incubated per well. LysoTracker™ Red DND-99 (Thermo Fisher #L7528) was incubated at 75 mol L^{-1} for one hour with the NCs as well as Hoechst for 30 min at 1 µg ml^{-1}. PLGA-Fluorescein and mPLGA-Fluorescein NCs were incubated for 4 hours at 37 °C, 5% CO_2 in a humidified incubator. After removed, cells were washed with 1X PBS twice, fixed with 3.7% paraformaldehyde

(PFA) for 10 minutes and washed again with 1X PBS. Slides were mounted with PBS:glycerol (50:50) and a cover slip was carefully placed over the samples. Image acquisition was performed on a Leica TSC SP2 confocal microscope using a 63x/1.32 immersion oil objective. Z-stacks were obtained with 0.2 µm intervals for PLGA-Fluorescein and mPLGA-Fluorescein NCs treated samples and 0.4 µm intervals for PLGA-NLR and mPLGA-NLR NCs treated samples. Each acquired image is composed of 512 x 512 pixels from one single frame. Samples were excited using 405 nm UV diode and excitation lasers at 488 nm (ArKr) and 543 nm (GreNe). Images were prepared using Fiji.[134]

4.2.11 Cell viability

To evaluate if the coated NCs would be a potential and more advantageous cancer treatment compared to the non-coated NCs, paclitaxel-encapsulated PLGA NCs were prepared and cell viability was investigated by MTT viability assay after 48 h incubation. Breast and breast cancer cells from mammary gland (MCF-10A and MCF-7), as well as adenocarcinoma lung cancer cells (A549) were seeded at 2 x 10^3 cells per well in 96-well plates and grown for 24 hours. Prior incubation, media was removed and 200 µl of mPLGA-PTX and PLGA-PTX NCs suspension in DMEM medium supplemented with 10% (v/v) FBS were added to each well. For MCF-10A cells, NCs were in MEBM medium without horse serum as recommended by the manufacturer. After 48 h, PLGA-PTX NCs were removed, cells washed twice with 1xPBS and 3-(4,5-dimethylthiazol-2-yl)-2,5-diphenyltetrazolium bromide (MTT) was incubate at 0.5 mg ml^{-1} for 4 h. Further, formazan crystals were dissolved in 100 µl of dimethyl sulfoxide (DMSO) per well and left under orbital agitation for at least 15 min. Measurements were performed at 570 and 630 nm using a microplate reader SpectraMax M3 (Molecular Devices). Cell viability was calculated compared to controls without treatment as described in Equation 3.5

$$cell\ viability\ (\%) = \frac{\left(A_{570sample} - A_{630sample}\right)}{A_{570control} - A_{630control}}\ x\ 100 \qquad (3.5)$$

where $A_{570sample}$ is the absorbance at 570 nm and $A_{630sample}$ at 630 nm of treated samples, while $A_{570control}$ and $A_{630control}$ represent the absorbance of non-treated samples or controls. Data analysis was performed using Origin 2020.

4.3 RESULTS

4.3.1 PLGA-PTX NCS and mPLGA-PTX NCs characterization

PLGA NCs and membrane-coated PLGA NCs size distribution was analyzed by dynamic light scattering (DLS) and Nanoparticle Tracking Analysis (NTA). NTA was also employed to estimate the number of particles per ml.

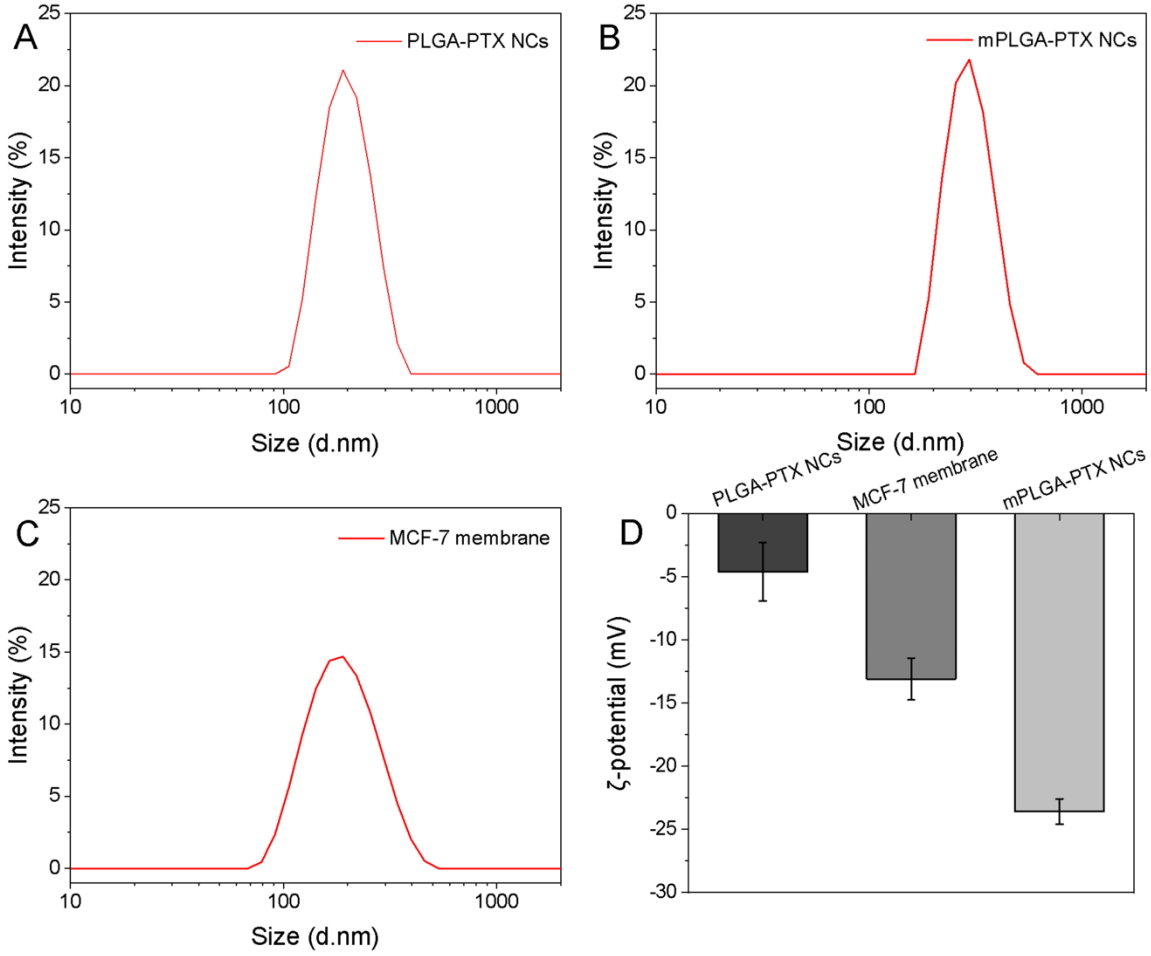

Figure 4.1 - Representative size distributions of A) PLGA-PTX NCs, B) MCF-7 membrane-coated PLGA-PTX NCs and C) MCF-7 membrane extract. D) PLGA-PTX, mPLGA-PTX and MCF-7 membrane extract zeta potential in 0.1 x PBS (pH 7.4). PLGA-PTX and mPLGA-PTX zeta potential values are represented as mean ± SD of three batches, MCF-7 membrane is representative of one extraction.
Source: By the author.

MCF-7 membrane extracts were obtained by hypotonic lysis followed by mechanical membrane disruption using a homogenizer (Dounce glass homogeneizer or

Glass homogenizer VIRTUS PII), and ultracentrifugation. A change in ζ-potential is observed, as well a shift in the hydrodynamic diameter, when the PLGA NCs are combined with MCF-7 membrane sonication (Figure 4.1, Table 4.1) which indicates the NCs coating with MCF-7 membranes.

Table 4.1 - Z-average, PdI (polydispersity index) and ζ-potential of PLGA-PTX (n=3), mPLGA-PTX (n=3) and MCF-7 (n=1) membrane extract were measured in 0.1x PBS. NTA size values are the mean of 2 different batches for PLGA-PTX and mPLGA-PTX NCs as well as particles concentration. MCF-7 membrane is representative of one extraction.

	Z-average (nm)	**PdI**	**NTA Size (nm)**	**Particles concentration (NCs ml^{-1})**	**ζ-potential (mV)**
PLGA-PTX	195	0.125	170	8.3×10^{12}	-5 ± 2
MCF-7 membrane	181	0.228	212	1.5×10^{11}	-13 ± 2
mPLGA-PTX	293	0.235	216	8.1×10^{11}	-24 ± 1

Source: By the author.

NCs morphology was observed by transmission electron microscopy, cryogenic transmission electron microscopy and scanning electron microscopy.

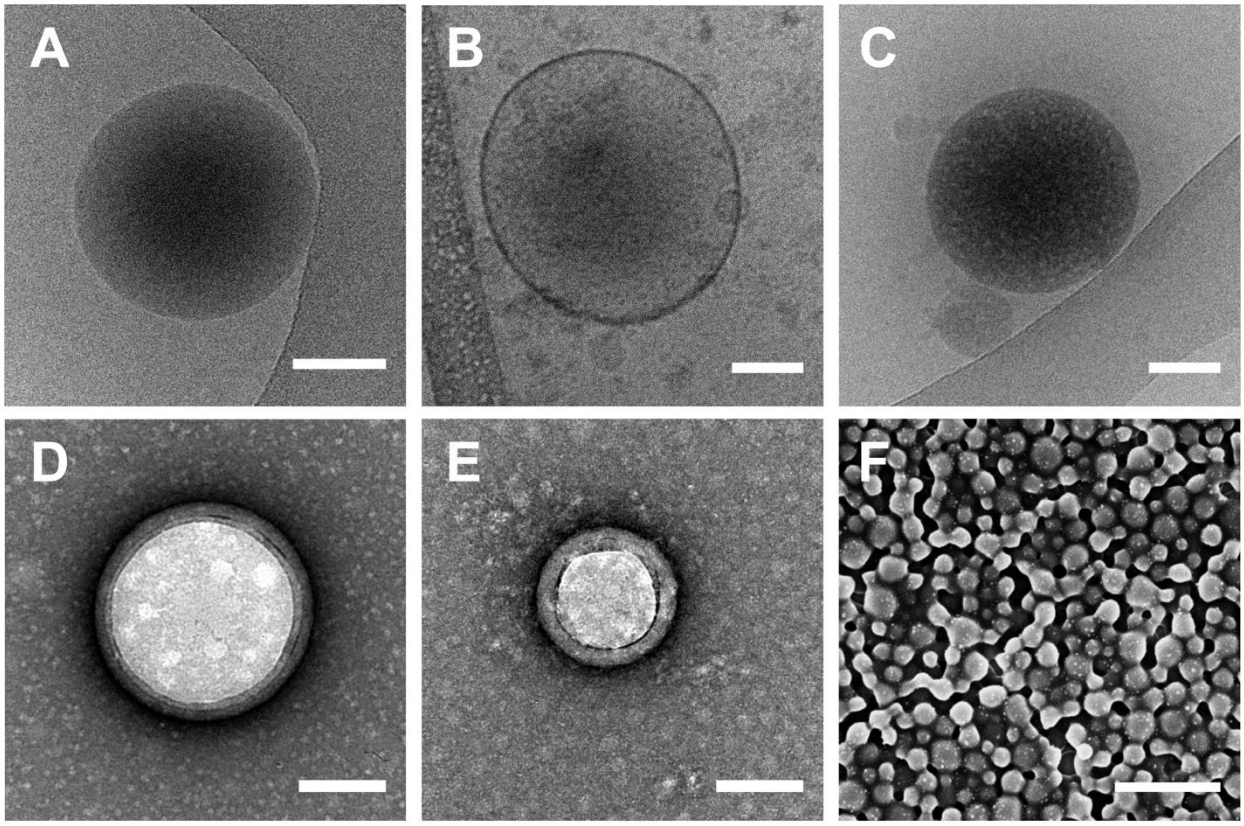

Figure 4.2 - CryoTEM images of A) PLGA-PTX, B) MCF-7 extracted membranes and C) (MCF-7)-membrane-coated PLGA-PTX measured in 0.1 x PBS (pH 7.4) where scale bars represent 100 nm. Negative staining transmission electron microscopy (TEM) of D) PLGA-PTX NCs and E) mPLGA-PTX NCs where scale bars represent 100 nm. F) Scanning electron microscopy (SEM) image of PLGA-PTX NCs imaged at 2 kV at high vacuum with Inlens detector where scale bar represents 500 nm.
Source: By the author.

Negative-stain transmission electron microscopy images (Figure 4.2D and 4.2E) illustrate the NCs spherical nature, although it was not possible to observe the membrane coating, as negative staining effects can lead to misinterpreted assumptions. CryoTEM analysis (Figure 4.2A, 2B and 2C) did not enable the membrane visualization with the NCs since contrast between membranes and NCs was not distinguishable. Although, it was noticeable the lack of overspread membranes in samples of mPLGA-PTX NCs when compared to MCF-7 membrane samples and PLGA-PTX NCs, which indicates the coating of the NCs with the membranes. Scanning electron microscopy images support the monodisperse nature of PLGA-PTX NCs as represented in Figure 4.2F.

Additionally, Fourier Transform-Infrared Spectroscopy (FTIR) of copolymer PLGA, nonionic surfactant Pluronic®-F127, blank PLGA NCs, PLGA-PTX NCs and MCF-7 membrane coated PLGA-PTX NCs was performed. Figure 4.3 displays FTIR spectra and permits to discriminate the mPLGA-PTX spectrum distinctive bands. Membranes are mainly composed of lipids, proteins and carbohydrates and the presence of few characteristic bands of these components can be observed like amide I (1650 cm^{-1}) band related to C=O stretching of peptide bonds, indicatives of proteins. The presence of carbohydrates and phosphate could be evidenced in the spectral range from 1250 to 1000 cm^{-1}, lipid phosphate head groups were not take into consideration because phosphate groups from PBS can lead to misreading of the spectrum.[213]

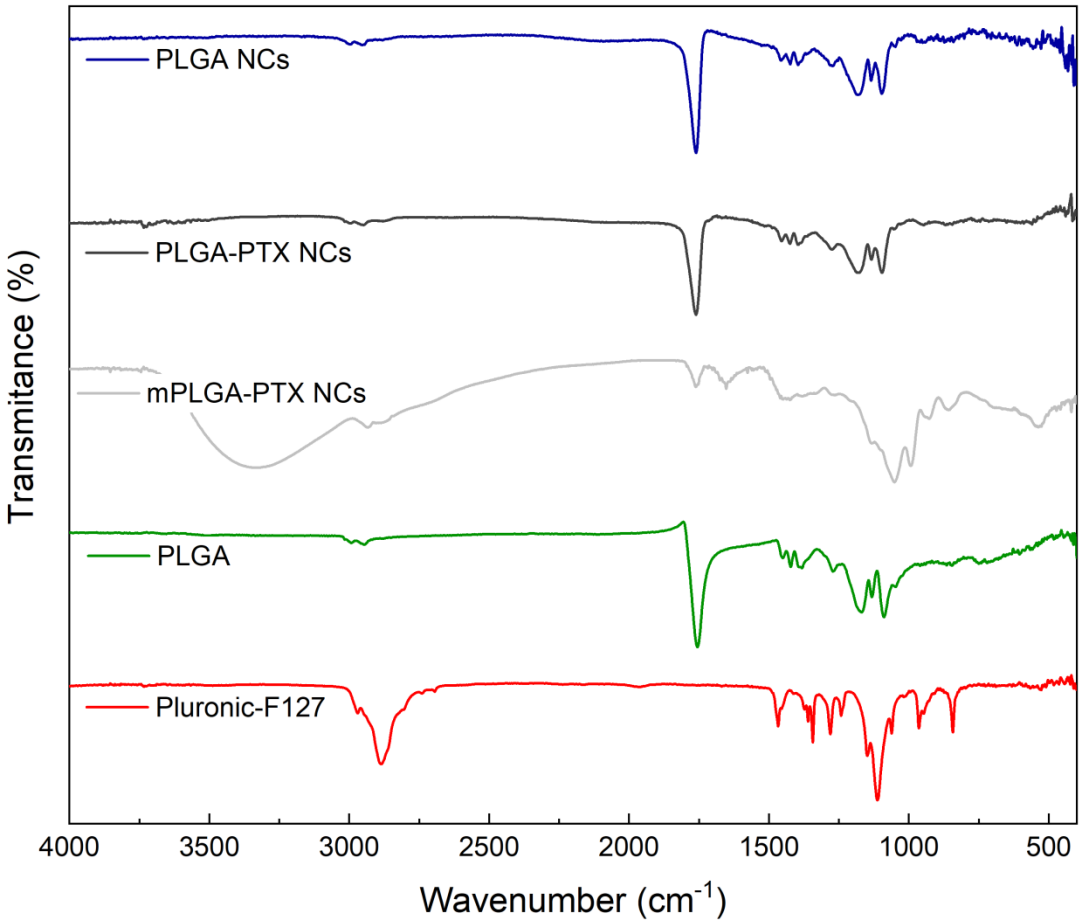

Figure 4.3 - FITR spectra of PLGA nanocarriers variations, PLGA and Pluronic®-F127 with 4 cm^{-1} resolution over 128 scans from 4000 to 400 cm^{-1}.
Source: By the author.

4.4.2 Encapsulation efficiency of paclitaxel in PLGA NCs

A HPLC method was developed and validated to estimate the encapsulation efficiency (EE%) of PLGA-PTX NCs. Briefly, the method consists of a mobile phase composed of acetonitrile and ddH_2O (50:50, (v/v)), an analytical C8 column (150 x 4.6 mm, 5 µm) and a precolumn analytical C8 (10 x 4 mm, 5 µm) as stationary phase. Detection wavelength was 227 nm and columns were kept at 30 °C. The retention time of paclitaxel was about 6.7 minutes and a symmetrical peak shape was observed (Figure 4.4).

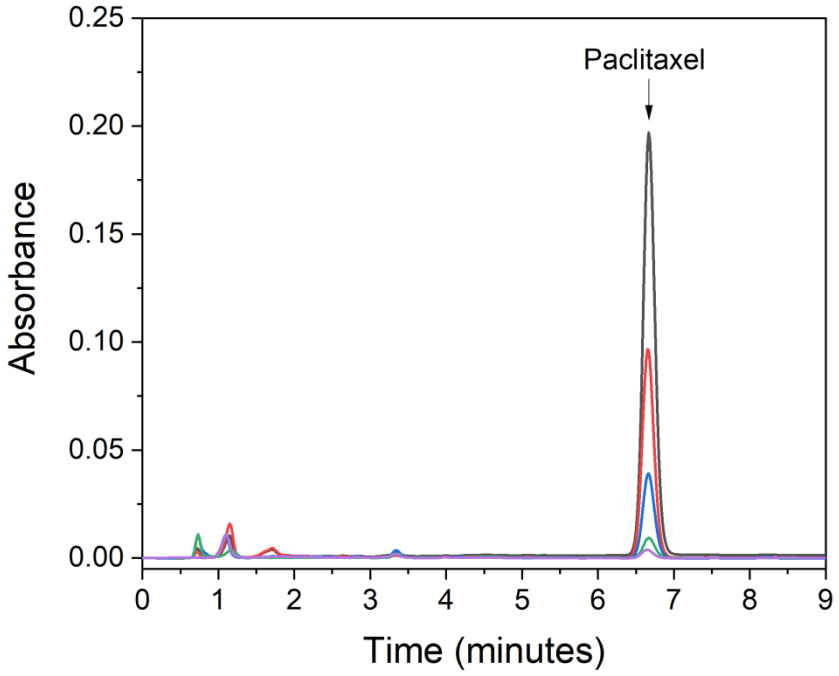

Figure 4.4 - Representative HPLC chromatograms of pure paclitaxel at 227 nm in the concentration range from 0.5 to 25 µg ml^{-1}.
Source: By the author.

The assumption of homoscedasticity was not met for the data and a weighted least squares linear regression (Table 4.2) was employed to compensate the effect of higher concentrations as reported by Almeida *et al*.[214]

Table 4.2 - Regression parameters for weighted regressions of the analytical curve ($y = ax + b$) where ω_i is the weight tested for the calibration with ω_i = 1 representing the unweighted regression and ΣER(%) respective sums of the relative errors (n=4).

ω_i	Linear coefficient	Slope	R^2	Σ ER (%)
1	10540	102146	1	-103
1/x	1008	103229	1	0
$1/x^2$	-214	103757	1	0
1/y	1063	103155	1	0.7
$1/y^2$	286	103631	1	1.5

Source: By the author.

Models $1/x$ and $1/x^2$ presented the lowest values of ΣER and $1/x$ was chosen to evaluate PTX concentrations in the linear range from 0.5 to 25 µg ml^{-1}. Table 4.3 displays the analytical parameters for the method.

Table 4.3 - Analytical parameters for the HPLC method using UV/ Vis detector at 227 nm and 30 °C.

Parameter	Paclitaxel
Analytical curve	y = 107035.91x - 1963.10
Linear range (µg ml^{-1})	0.5 - 25
LOQ (µg ml^{-1})	0.1
Accuracy (ER%)	$\leq$ 3.4
Precision (CV%)	0.5-3.3

Source: By the author.

No coeluting peaks were detected at the retention time of PTX when NCs components were present in the sample (Appendix B Figure S1) exhibiting good stability on matrix. System suitability tests revealed that time retention of PTX shows a coefficient of variation of 0.3% and, for the peak integrated area, the coefficient was 0.1%. In addition, the method did not remain unaffected by changes in temperature, flow rate and mobile phase composition, implying lack of robustness. However, all those parameters are controlled by the analytical system and the method was suitable for paclitaxel quantification.

Employing the validated method, three batches of paclitaxel-containing PLGA NCs were analyzed, regarding their encapsulation efficiency (EE). Samples were prepared as described in the Materials and method section and EE for the three batches was (98 ± 1) % (Mean ± SD) (See in Figure S1, Appendix B).

4.4.3 (MCF-7)-membrane-coated PLGA NCs preferential cellular uptake

Flow cytometry experiments were performed to evaluate the cellular uptake of cell (MCF-7)-membrane-coated and non-coated PLGA NCs. Curcumin was used as fluorescent probe.

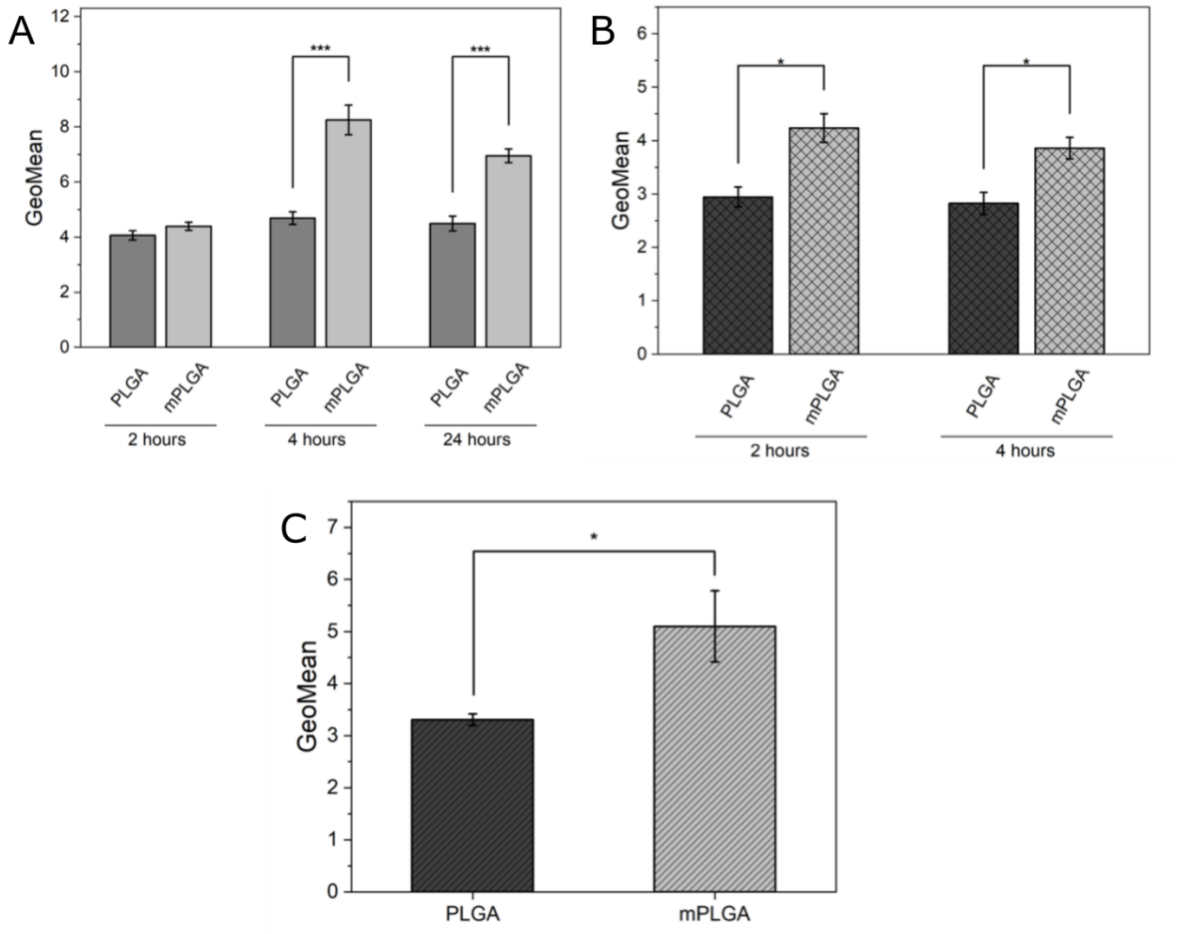

Figure 4.5 - Cellular uptake comparison between PLGA-Curcumin NCs and mPLGA-Curcumin NCs by A) MCF-7 breast cancer cells incubated for 2, 4 and 24 hours B) A549 lung cancer cells incubated for 2 and 4 hours and C) MCF-10A non-tumorigenic breast cells incubated for 4 hours. Measurements are average ± SE of three independent experiments. Data was analyzed by analysis of variance (ANOVA) and Tukey's test. Significances are indicated with * for p-value < 0.05, ** for p-value < 0.01 and *** for p-value < 0.001.

Source: By the author.

An increase in internalization is observed when the membrane-coated NCs are incubated with cancer (Figure 4.5A and 4.5B) and non-cancer cells (Figure 4.5C), however mPLGA NCs show a superior effect on MCF-7 breast cancer cells (Figure 4.6), same cell type as the membrane covering the NCs. Increased interaction in the presence of membrane coating with MCF-7 relates to the capability of homologous binding between cancer cells which reflects as a better targetability. Nevertheless, heterotypic adhesion seems to play a role in the interaction between A549 and MCF-10A cell types, since interaction levels of membrane-coated NCs are superior to the ones observed for non-coated NCs, suggesting the involvement of common cell adhesion molecules, e.g. epithelial cell adhesion molecule (EpCAM). [215]

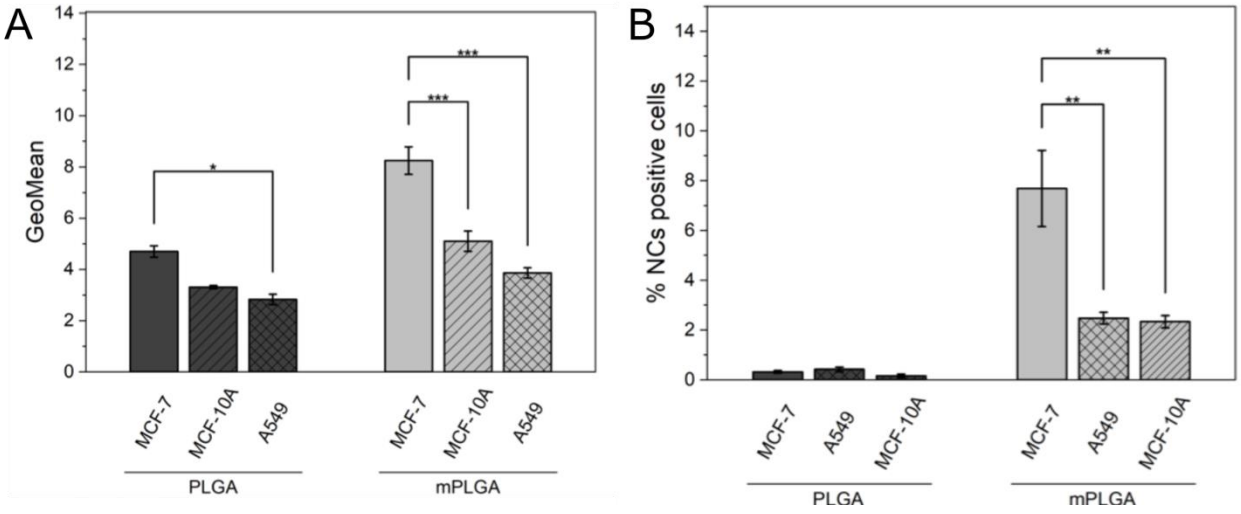

Figure 4.6 - Effect of MCF-7 membrane coating of PLGA NCs in cellular uptake. A) Cellular uptake and B) percentage of cells positive for curcumin-loaded PLGA NCs coated with MCF-7 membrane (mPLGA) and non-coated (PLGA) after 4 hours incubation with MCF-7, A549 and MCF-10A cells at 37 °C in atmosphere with 5% CO_2. Measurements are average ± SE of three independent experiments. Data was analyzed by ANOVA and Tukey's test. Significances are indicated with * for p-value < 0.05, ** for p-value < 0.01 and *** for p-value < 0.001.
Source: By the author.

MCF-7 membrane coated and non-coated PLGA-Fluorescein and PLGA-NLR NCs were incubated with MCF-7 and MCF-10A cells at $5x10^{10}$ NCs per chamber for confocal microscopy analysis. Figure 4.7 shows the cellular uptake of PLGA-Fluorescein and mPLGA-Fluorescein NCs by MCF-7 and MCF-10A after 4 h incubation. The images evidence that the presence of MCF-7 cells membrane coating affects the internalization

of PLGA NCs by both cancerous and non-cancerous cell types, being more pronounced in MCF-7 cells, corroborating the results obtained by flow cytometry.

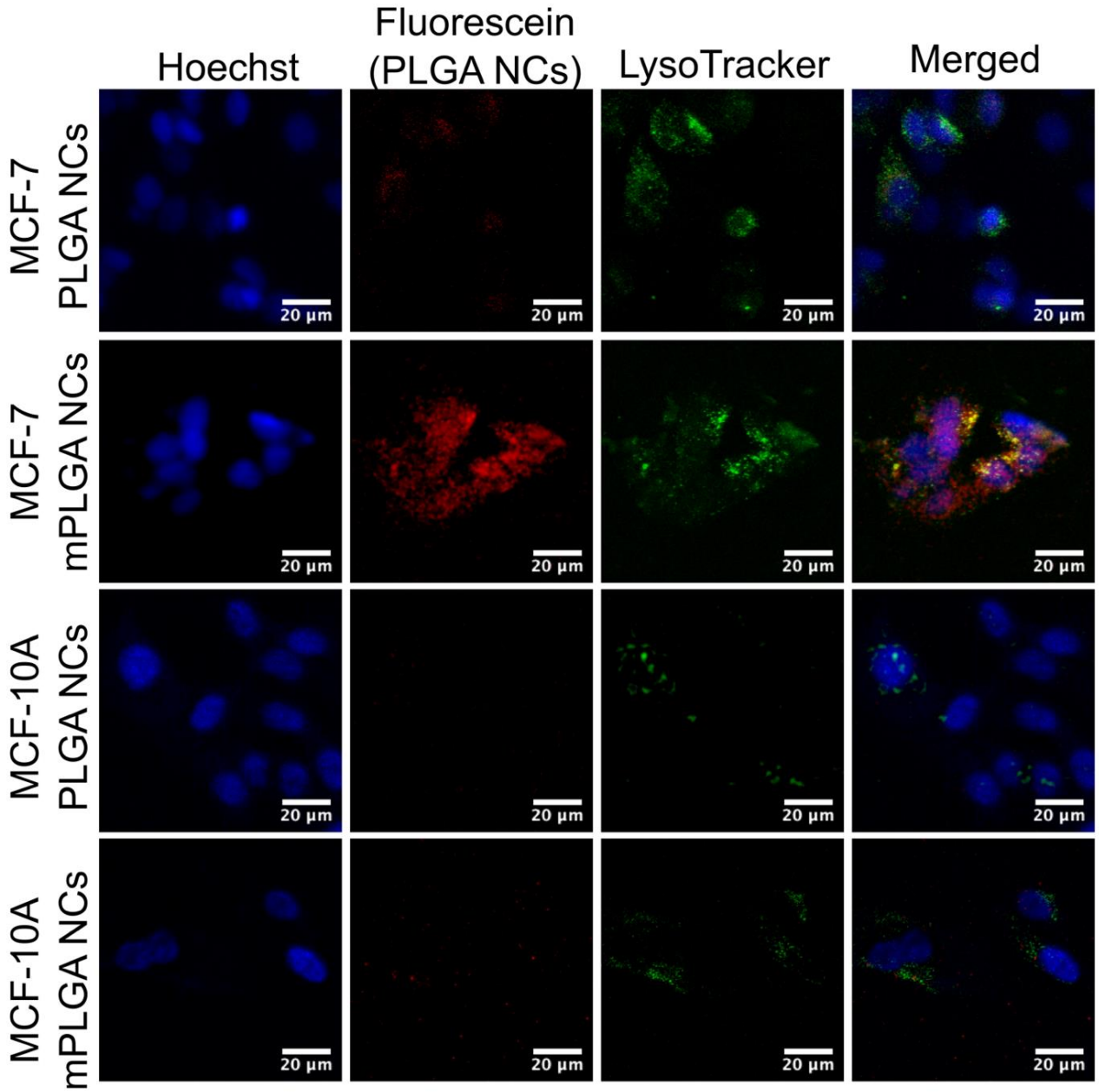

Figure 4.7 - Confocal laser scanning images of MCF-7 and MCF-10A cells treated with coated and non-coated PLGA-Fluorescein NCs for 4 hours. Cell were imaged with a 63x oil-immersion objective and acquired in z-stacks at 0.2 µm intervals. Images were acquired with the same system and laser settings.
Source By the author.

Because PLGA-Fluorescein NCs did not provide a strong fluorescent signal, PLGA-NLR NCs were employed to observe the interaction with both cells lines and to

verify if the NCs signal was truthful or a possible effect of microscopy settings. PLGA-NLR NCs were incubated for 1 h and other staining procedures were kept the same as previously described. Representative acquired images are in Appendix B, Figure S2.

4.3.4 In vitro evaluation of (MCF-7)-membrane coated PLGA-PTX NCs against epithelial cell types

Based on the previous results, it is important to evaluate the potential of coated NCs for clinical application. For this purpose, paclitaxel, a chemotherapy agent, was entrapped in PLGA NCs and cell viability was assessed for MCF-7 (Figure 4.8A) and A549 (Figure 4.8B) epithelial cancer cells, and MCF-10A (Figure 4.8C) non-tumorigenic breast cells. NCs concentration was estimated using NTA and concentrations from 1 x 10^8 to 1x10^{10} NCs per ml were tested, with 200 µl per well, meaning paclitaxel concentration was in the range of few to hundreds of ng per ml. NCs were incubated for 48 h and cell viability tested using MTT assay.

In Figure 4.8A, the anti-cancer improved ability of cell-membrane coated PLGA-PTX NCs is evidenced by the significantly lower viability of MCF-7 cells treated with MCF-7-membrane coated PLGA-PTX NCs, compared to non-coated PLGA-PTX NCs. Likewise, the viability of MCF-10A and A549 cells was investigated and no significant changes were observed between cells treated with membrane-coated or non-coated PLGA-PTX NCs.

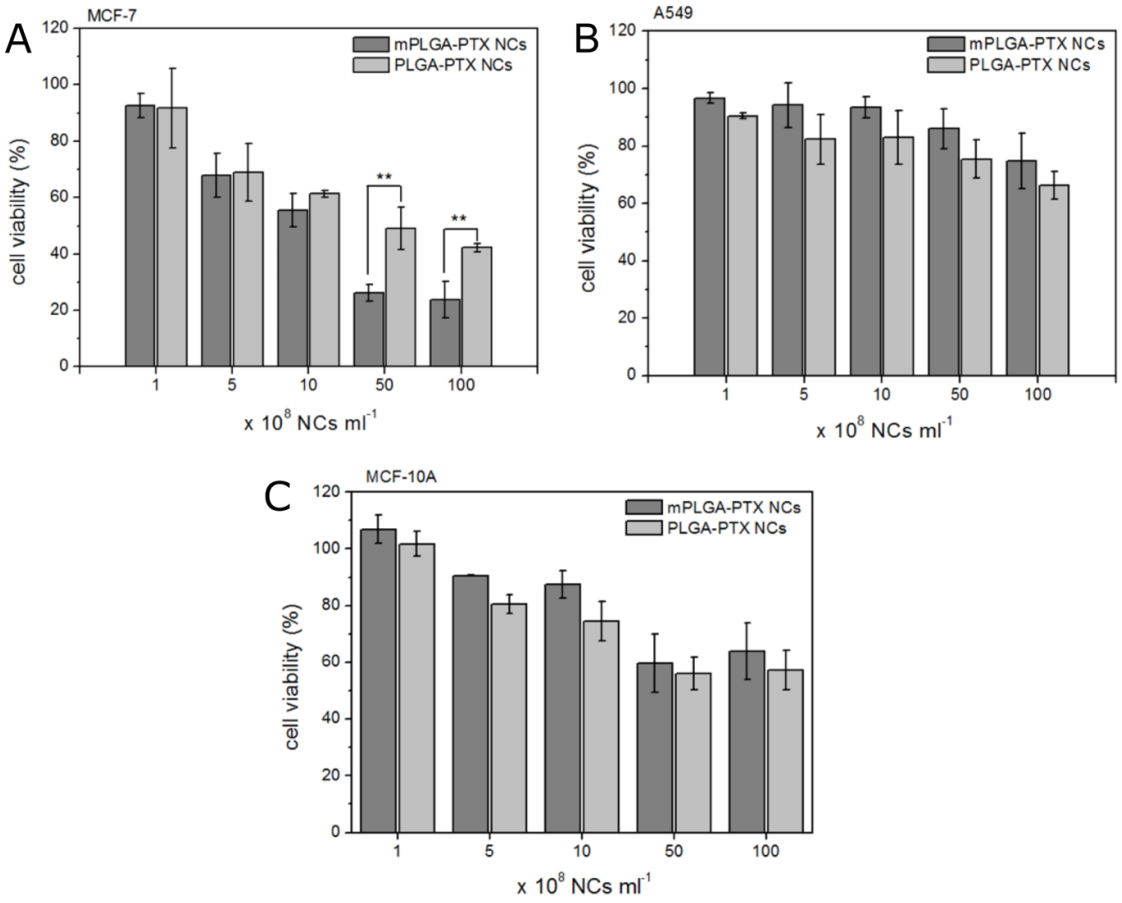

Figure 4.8 - Cellular viability of A) MCF-7, B) A549 and C) MCF-10A after 48 h incubation with different concentrations of mPLGA-PTX and PLGA-PTX NCs evaluated by MTT viability assay. Data was analyzed using using two-sample t-test and significances are indicated. Significances are indicated by ** for p-value < 0.01.
Source: By the author.

4.5 DISCUSSION

This chapter focusses on the development of cancer cell membrane-coated PLGA NCs containing paclitaxel, a chemotherapeutic drug, to explore the homotypic adhesion between cancer cells to improve treatment effectiveness.

After the extraction of MCF-7 membranes by hypotonic lysis, PLGA NCs were coated by sonication and characterized according to their size, ζ-potential, and concentration. An increase in size and surface charge were observed, which are indications that NCs functionalization with membranes extract was successful (Figure 4.1).[108,211] Microscopy analysis showed a distinctive vesicular characteristic in the membranes confirming the extraction without structural modification. For the coated

NCs, transmission electron microscopy images revealed a lack of spare membrane in the images, evidencing the interaction and colocalization of the membrane on PLGA surface (Figure 4.2).[216] Additionally, FTIR analysis exhibited bands characteristic of lipids (Figure 4.3). Paclitaxel encapsulation efficiency in PLGA-PTX NCs was 98 ± 1% according to the described HPLC method. The encapsulation of the drug by nanoprecipitation obtained a high encapsulation yield, given the hydrophobic characteristic of the agent.

The interaction analysis between the membrane-coated NCs and non-coated NCs by flow cytometry revealed an increase in cell-nanocarrier interaction with MCF-7, A549 and MCF-10A, indicating the occurrence of homotypic and heterotypic adhesion (Figures 4.5, 4.6 and 4.7) with higher interaction for the cell line which membrane was extracted (Figure 3.5). These results suggest the presence of common membrane antigens, e.g. EpCAM, expressed in normal epithelia, and often overexpressed in epithelial tumor.[215, 217] The increase in the percentage of positive cells shows clearly the influence of the cell membrane coating on particle adhesion to the cancer cells. An increase of more than 26-fold for the source cells is observed, in contrast to about 13 and 6-fold for MCF-10A and A549, respectively, when (MCF-7) cell membrane-coated PLGA NCs are incubated with those cells compared to the non-coated PLGA NCs. The variations in uptake levels between non-coated NCs and membrane-coated NCs were of 1.8, 1.5 and 1.4-fold for MCF-7, MCF-10A and A549, respectively. The preferential cancer cell self-recognition is also substantiated by the confocal microscopy images in Figure 4.7. Reported cancer cell membrane-coated systems showed an increase in interaction with other cell types that not the source of the membrane extract. However, the increase is often reported as a minor variation which can be associated to the low similarities between the cellular types and many fail to evaluate the effect on normal cells from the same tissue as the cancer. Fang et al.[108] coated PLGA nanoparticles with B16–F10 mouse melanoma cells membrane and evaluate their interaction with MDA-MB-435, also a human melanoma cell line,[218] and HFF-1, a human foreskin fibroblast cell line. They describe the homotypical interaction between the NCs and the MDA-MB-435 melanoma cells, but not from the source melanoma cell line. This already indicates

the homotypical interaction with different cancer cells. Although, normal cell interaction is assessed for skin fibroblast and only a minor variation is observed, as expected.

It should be notice that the occurrence of increased interaction with normal cells does not invalidate the technology. Tissue invasion is one of the classical hallmarks of cancer development together with uncontrolled division, that combined with tumor heterogeneity humper tumor treatment and is a major issue to homogenous distribution of chemotherapeutics.[219-220] The technology efficacy was also tested in *in vivo* systems and presented interesting results. Rao and colleagues[221] used head and neck squamous cell carcinoma patient-derived tumor cells to coat gelatin nanoparticles loaded with cisplatin. They demonstrate not only almost complete tumor elimination by treatment with the membrane-coated gelatin particles loaded with cisplatin, but also a good response against tumor recurrence in postsurgery model.

To substantiate the effectiveness of the MCF-7 cells membrane-coated PLGA NCs, cell viability studies with mPLGA-PTX and PLGA-PTX NCs (Figure 4.8) were performed. The results confirmed that the coating of NCs with cell membranes can be beneficial to the cancer treatment where at higher concentrations of mPLGA-PTX NCs the viability of MCF-7 cells was reduced in 25% when comparing to PLGA-PTX NCs. The cell viability of A549 and MCF10A cells exposed to the coated and non-coated NCs were not significantly different with lowest viability about 60% for MCF-10A at the highest tested concentration, while viability was between 20 and 25% for MCF-7 cells exposed to mPLGA-PTX NCs for 48h.

4.6 CONCLUSIONS

Here we successfully functionalized PLGA NCs with MCF-7 cells membrane extracts which led to preferential interaction of MCF-7 cells with mPLGA NCs and improved treatment efficacy against the breast cancer cell line. The increased interactions between MCF-7 membrane-coated NCs compared to non-coated counterparts combined with their improved efficacy against MCF-7 breast cancer cells make them suitable and an attracting improvement from traditional cancer treatments. Although this work contributes to elucidate how coated-nanocarriers interact with

different cell types and highlights the versatility of PLGA systems and easily transferable coating employing other cell types, further work is required to prove the efficacy *in vivo* and in personalized clinical applications, based on primary cells isolated from tumorigenic-tissue.

5 CHAPTER V: LIGHT-INDUCED MOLECULAR ROTATION TRIGGERS ON-DEMAND RELEASE IN LIPOSOMES

Authors: Laís Ribovski;[1,2] Qihui Zhou;[3] Jiawen Chen;[4] Ben L. Feringa;[4] Patrick van Rijn;*[1] Inge Zuhorn.*[1]

[1]University of Groningen, University Medical Center Groningen, Department of Biomedical Engineering, Groningen, the Netherlands. A. Deusinglaan 1, 9713 AV Groningen, The Netherlands

[2]Nanomedicine and Nanotoxicology Group, Physics Institute of São Carlos, University of São Paulo, CP 369, 13560-970 São Carlos, SP, Brazil

[3]Institute for Translational Medicine, Department of Periodontology, The Affiliated Hospital of Qingdao University, Qingdao University, Qingdao 266021, China.

[4]Center for Systems Chemistry, Stratingh Institute for Chemistry, University of Groningen, Nijenborgh 4, 9747AG Groningen, Netherlands

*Corresponding authors: Patrick van Rijn; Inge Zuhorn

E-mail address: p.van.rijn@umcg.nl; i.zuhorn@umcg.nl

ABSTRACT

Controllable release of therapeutic compounds from delivery vehicles is essential to successfully reduce drug toxicity and improve therapeutic efficacy. Many new nanomaterials that display responsive character to external stimuli are being developed in order to achieve such controlled release. However, introducing on demand release in established and approved drug delivery systems would better facilitate their clinical translation. Light-induced rotating hydrophobic molecular motors were therefore incorporated in the lipid bilayer of established phospholipid vesicles (liposomes) with the aim of using molecular rotation to destabilize the bilayer and facilitate on-demand release of liposomal content. To evaluate the phospholipid bilayer response to the molecular motion we investigated the release of a model hydrophilic molecule, calcein, from liposomes composed of the unsaturated lipid 1,2-dioleoyl-sn-glycero-3-phosphocholine ((Δ9-cis)PC). The presence of molecular motors in liposomes together with irradiation triggered calcein release, which did not occur from liposomes with molecular motors without irradiation, nor from liposomes without motors with irradiation. Additionally, an increase in calcein release was obtained upon prolonged irradiation. The integration of sophisticated molecular components with well-established clinically relevant nanocarrier systems provides the possibility to enhance nanomedical treatments without the need to redesign completely new carrier systems that would be a long way from clinical use.

Keywords: liposomes, molecular motors, light-triggered release, on-demand release.

5.1 INTRODUCTION

Within the field of nanomedicine, specialized approaches to transport pharmaceutically active compounds to target sites by means of nanostructures is one of the main goals.[222] The use of specialized nanocarriers (NCs) are considered to be highly promising in treating various diseases including combating infections, inflammation, fibrosis, and cancer.[223-224] Many nanoparticle systems have been developed over the years for diagnosis and therapy of diseases, which includes solid inorganic nanoparticles, polymeric nanoparticles such as micelles and polymersomes, protein nanoparticles, and lipid-based nanoparticles such as liposomes and lipid nanoparticles (LNPs).[223-229] A key aspect of NCs is not only to accommodate the drugs that need to be delivered but particularly to release them on demand in order to increase local drug concentrations to achieve therapeutic effectiveness, while preventing side effects.[227]

For on demand drug release from NCs, external triggers or local factors are often envisioned. Local factors that can be exploited are e.g. a change (drop) in pH (such as in tumor tissues)[230] or alterations in temperature and pH due to inflammation of the tissue[231]. Many stimuli-responsive systems that have been developed are often polymer-based, because of the ease of polymer synthesis that allows for good control over their composition, which is necessary to fine-tune their response to specific stimuli.[232-234] In light of the possibilities using polymers as responsive structures to deliver pharmaceutical cargo, highly interesting drug delivery systems have been developed. Small micellar structures that respond to redox conditions have been designed to release the anti-cancer drug camptothecin in the presence of high glutathione concentration and reactive oxygen species inside tumors. Similarly, thermo-sensitive (e.g. poly(N-alkylacrylamide)s) and pH-responsive polymers (ionizable polymers containing e.g. amines or carboxylates) are used to trigger release in response to an environmental stimulus.[235] These polymers have been used to develop systems that mediate immunogenic cell death[236], and deliver anti-inflammatory as well as anti-cancer drugs such as doxorubicin to tumors.[231,237] Lipid-based systems are also extremely attractive as triggered release systems. Easy to prepare, they also present flexibility of design, low immune response and are capable of containing large payloads which

facilitate clinical translation.[238-239] LNPs are often employed to delivery genetic material,[239-240] but they are also used for drug delivery in cancer therapy,[241-243] delivery of hormones[244] and imagining.[245-247] Liposomes applications in medicine are also broad, including drug and genetic material delivery.[248-249] The lipid-delivery systems can also rely on controlled/triggered-release. Relying on local factors of the microenvironment in diseased tissue is not desirable in case of inter-patient and intra-patient heterogeneity. Hence, other triggers that are not purely related to the local environment are being used in the development of nanocarriers, including magnetic fields,[250] ultrasound,[251] and light.[252] Temperature-sensitive liposomes are a well-known system described long ago.[253] The temperature input relies on other compounds or materials, e.g. inorganic nanoparticles that can produce heat with light or magnetic field input. Particularly the use of photo-responsive particles and delivery approaches are interesting as these will allow on demand release. Photo- responsive polymersomes have been developed to release molecular payloads,[254] including light-triggered nitric oxide release for corneal wound healing.[255] Light-dependent release has the disadvantage of presenting phototoxicity,[256] where if the systems allows short exposure, phototoxicity can be prevented or reduced. Another disadvantage is that most release mechanisms induce membrane destabilization or permeabilization and membrane stability cannot be recuperated.

We propose as an alternative MM liposomes that show light-triggered release through mechanical action without inducing phototoxicity, and allow for controlled step-wise release through reversibility of molecular motion. It is clear that polymers and lipids have a great potential future within the clinic concerning nanomedicine. However, most formulations that have been approved in the clinic and are historically much longer investigated, are phospholipid-based structures.[225-226] Liposomes have since long times been used in drug formulations, imaging, and delivery.[257-259] Light-triggered release using amphiphilic phthalocyanine in conventional liposomes have been designed to release payload using near-infra red[260] irradiation but also adding gold to the liposome surface to utilize the plasmon-resonance effect facilitate release,[261] or embedding graphene-oxide inside liposomes as the light-responsive moiety.[262] In most cases, light is being transformed into heat that in turn locally increases the temperature and

facilitates release from the liposomes. An alternative approach would be not to rely on heat transfer properties but directly influence the local structural features of e.g. a selective channel [263] in a lipid bilayer without the need for chemical alterations or heat induced phase changes.

We hypothesized that small unidirectional molecular motors that are hydrophobic in nature and reside inside the lipid bilayer would open up the membrane upon irradiation. Recently, such unidirectional molecular motors have been used to direct stem cell fate as well as interacting with cell membranes in order to permeabilize it and facilitate cellular uptake.[264-265] These unidirectional molecular motors are tunable in chemistry and rotation speed and offer direct mechanical interaction with their surrounding mediated by light.[75, 266-267]

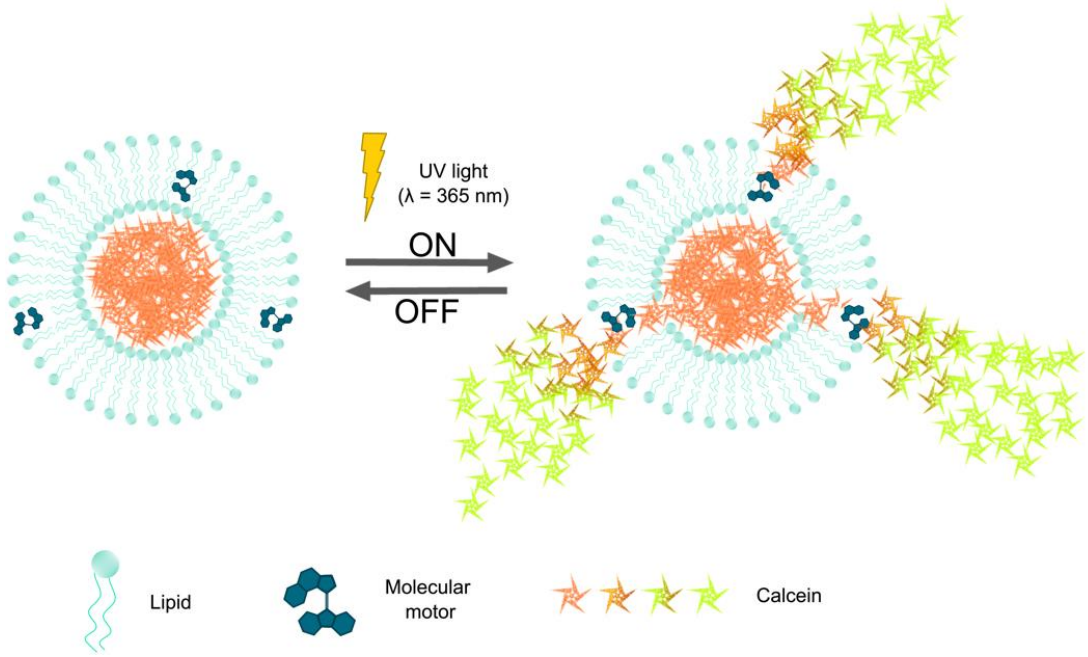

Figure 5.1 - Schematic representation of the mode of operation of on demand release from liposome loaded with molecular motors inside by bilayer. The unidirectional molecular rotation disturbs the bilayer and thereby facilitates release of stored molecular components, here calcein as a model compound.
Source: By the author.

The molecular motor was embedded inside a phospholipid-based nanocarrier, a liposome, and the hydrophobic nature of the molecular motor enables it to reside in the hydrophobic interior of the membrane. It was found that calcein-loaded liposomes displayed enhanced release upon irradiation. This release was only triggered when both

the molecular motor was present and when irradiation was applied offering control and on demand release capabilities. By increasing the irradiation time, the amount of calcein released from the liposome was controlled. The proposed system opens up possibilities of adding sophisticated small molecular components via simple mixing and self-assembly to interfere in a direct fashion with the local structural features and thereby allowing on demand events to occur such as controlled delivery as depicted in Scheme 5.1.

5.2 MATERIALS AND METHODS

5.2.1 Liposome preparation

Liposomes with 10 mM 1,2-dioleoyl-sn-glycero-3-phosphocholine (#850375P, 18:1 (Δ9-Cis) PC (DOPC)), Avanti Polar Lipids, Inc.) were prepared by hydration method followed by extrusion through polycarbonate 100 nm pore membrane. Lipid was dissolved in chloroform and mixed with pure methanol (#1060092511, Emsure® Merck) or methanol containing molecular motors in a ratio 1:1. The mixtures were dried under a stream of N_2 followed by evaporation under reduced pressure. The dry lipid films were hydrated with 100 mmol L^{-1} solution of calcein (#C0875, Sigma-Aldrich) in HEPES (10 mM, pH 7.4). Liposomes containing MM (synthesis of MM described in [267])were prepared at two different mixing ratios with 4-fold difference, 1:50 (MM1) and 2:25 (MM2) of MM to lipid (MM:lipid). Liposomes were mixed thoroughly for 2-3 hours and extruded 17 times using an Avestin LiposoFast - Basic extruder with two gas tight glass syringes and assembled with two filter supports (#610014, Avanti) and one 100-nm pore polycarbonate membrane (Avestin) prewetted in HEPES buffer. Liposome purification was performed using a gel filtration resin Sephadex® G-100 (#17006001, GE Healthcare) eluted in the preparation buffer HEPES (10 mM, 7.4). The purification setup was protected from light during purification.

5.2.2 Liposomes characterization

Liposomes size and zeta potential (ζ-potential) were determined by a Zetasizer Nano ZS (Malvern Instruments) after purification in 10 mM HEPES, pH 7.4. Release experiments fluorescence measurements were performed in a Synergy HTX Multi-mode plate reader (BioTek Instruments Inc.) with excitation 485/20 nm and emission 528/20 nm using 96-well black flat bottom plates. Number of flashes was set at 3 flashes per well to reduce photobleaching.

Ultraviolet-visible spectroscopy characterization of molecular motors in HEPES was carried out in a PerkimElmer Lambda 2 UV-Vis spectrophotometer using a Hellma® Analytics quartz cuvette with 10 mm light path (# 100-10-46).

Samples UV light irradiation (λ_{max} = 365 nm) was performed with a Spectroline lamp model ENB-280C/FE kept ≈10 cm from the 96-well plate containing the samples with delivery intensity of ≈ 0.2 mW cm^{-2}.

5.3 RESULTS

The molecular motor (MM) is water-insoluble and similar as other small molecular components; they can be stored inside the hydrophobic domain of the phospholipid membrane. The MMs and the lipids were initially mixed in a chloroform/methanol mixture to create a mixed film. Two ratios of phospholipids:MM were chosen, a 1:50 and a 2:25. The phospholipid films without and with different amounts of MMs were hydrated and extruded through a polycarbonate filter to obtain small unilamellar vesicles. From dynamic light scattering analysis, it was observed that the control liposomes without MM and the liposomes with MM in a ratio of 1:50 has similar size of 120nm and 110nm, respectively (Figure 5.2). The higher loading of MM into the liposome resulted in larger diameters than the control and the low loaded liposome. It is known that incorporation of molecular components may be associated with destabilization of the bilayer structure resulting in an altered morphology. This altered morphology would greatly affect the overall release and would not pose as a correct comparison between the control and the low loaded liposomes.

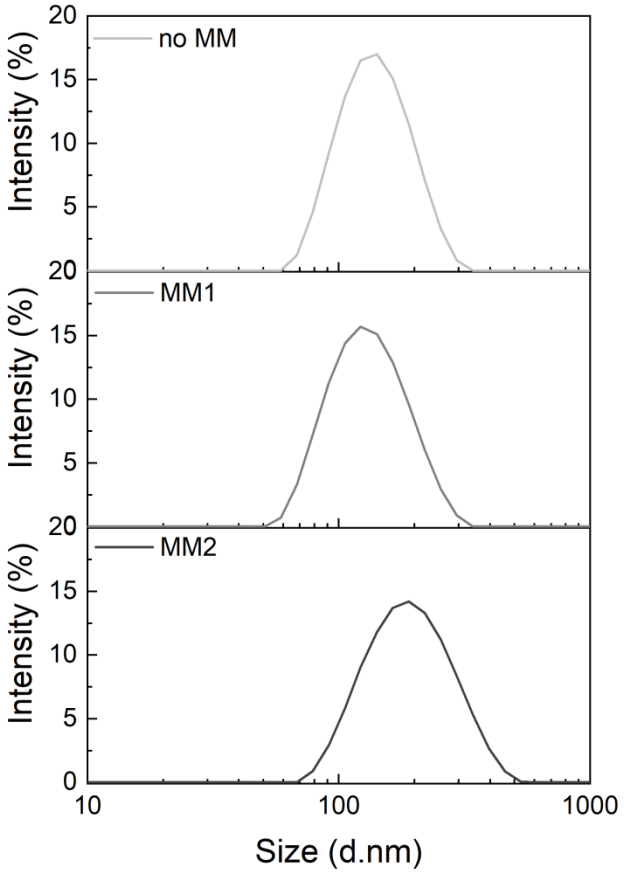

Figure 5.2 - Dynamic Light Scattering of (Δ9-cis)PC liposomes without MM (no MM), and with MM at mixing ratio 1:50 (MM1) and 2:25 (MM2) after purification with Sephadex® G100. Size control was induced via extrusion through a polycarbonate filter (pore-size 100 nm) and the measurements were performed at 20°C.
Source: By the author.

The zeta-potential (surface charge) of the liposomes displayed similar characteristics comparing the non-loaded liposome and the liposome/MM (50:1) with a significantly reduced surface charge for the higher MM-loading (25:2) (Figure 5.3). These observations indicated that indeed the higher loading does not maintain the liposomal structure and was therefore not chosen to be included into the light-triggered release studies.

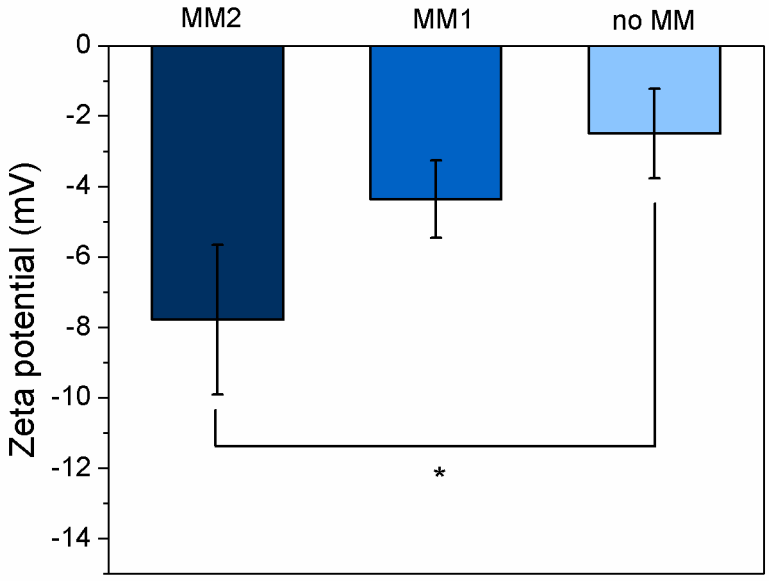

Figure 5.3 - The zeta (ζ)-potential of (Δ9-cis)PC liposomes without MM (no MM), and with MM at mixing ratio 1:50 (MM1) and 2:25 (MM2) after purification with Sephadex® G100. ζ-potential values are mean ± SD of three measurements of the same batch. Data was analyzed using two-sample t-test and significance is indicated by * for p-value < 0.05.
Source: By the author.

The liposomes were loaded with calcein as a model compound as it is very suitable to analyze the release due to the fluorescent properties of calcein. Liposomes, formed upon hydration of the lipid film with and without MM, was performed with a calcein solution with the concentration above the self-quenching concentration. Above the self-quenching concentration, calcein displays a substantially reduced fluorescence intensity. This concentration is maintained inside the liposome and upon release of calcein into its environment after purification of the loaded liposomes, the concentration will decrease and associated with it, the fluorescence will increase. Therefore, any released calcein will become clearly measurable and distinguishable from the non-released calcein. Analysis of the fluorescence over time and correcting it for the state where liposomes are fully destroyed (full release), the percentage release (%) over time can be determined.

Both the liposome control and the MM-loaded liposome (1:50) were subjected to the same treatments and the fluorescence intensity determined and corrected for the

final 100% release (Figure 5.4). The release time was assessed both without and with irradiation to identify the overall stability of the liposomes over time (Figure 5.4A) and the influence of UV-irradiation on both the liposome without MM and with MM in the bilayer. Figure 4A shows the release over time for the duration of the analysis up to 70 minutes, no significant release was detected in both the liposomes without and with MM. These results indicate that the low amount of MM inside the lipid bilayer does not cause enhanced leakiness of the membrane. The calcein loaded liposomes were irradiated using UV-light for 30 seconds with a wavelength of 365 nm. The irradiation causes the molecular motor to rotate and induce molecular motion. It was envisioned that this would disrupt the bilayer making it more permeable. Interactions between molecular motors and cell membrane was very recently identified and facilitates cellular uptake. Here the method was used to facilitated triggered and controlled release which is pertinent in the field of nanomedicine.

The liposome containing MM, irradiated for 30 seconds with 365 nm UV-light of which subsequently the release was studied, displayed enhanced release. The 30-second irradiation induced a steady release up to 10% until 60-70 minutes after which the release seized. During this release period, no irradiation was applied and therefore molecular motion is no longer destabilizing the membrane. The seized release indicates that moderate release can occur rather than all content. The molecular motion of the motor inside the lipid bilayer does not result in destruction of the membrane. Homeostasis of the membrane resets and restoration of the membrane integrity allows the liposome to regain its initial stability. Alternatively, the liposome without MM loaded into the bilayer did not display any release (Figure 5.4B) and therefore it is not UV-irradiation that may cause a local increase in temperature or irradiation induced molecular alterations to the lipid membrane that induces the release and indicates that the unidirectional rotating molecular motor is the key feature.

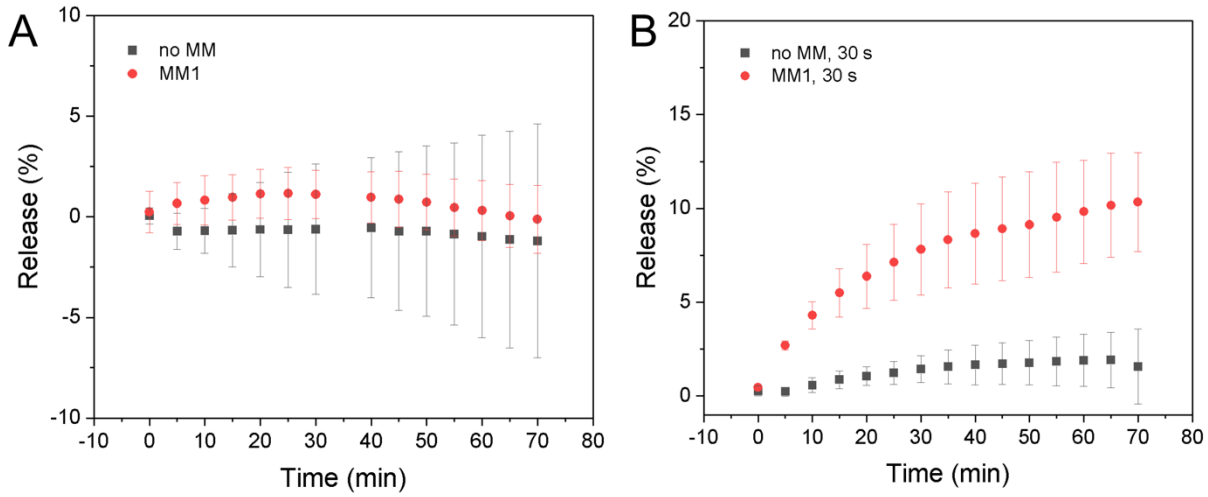

Figure 5.4 - Liposomes without and with MM (1:50) without irradiation (A) and with irradiation for 30 seconds (B) of which the calcein release was studied using fluorescence spectroscopy. Measurements are average ± SD of three independent experiments.
Source: By the author.

Figure 5.5 shows the quantified release at intermediate time points to further exemplify the difference between MM-loaded liposomes and non-loaded lipsomes. It is clearly distinguishable that most of the release occurs shortly after the irradiation-step and only for the liposomes that have the molecular motor incorporated into the lipid membrane. A small amount of release is detected for the liposomes without the MM inside the membrane and a release of up to 1% was found. This indicate that there is a very minor amount of unspecific release that was not detected in the samples without irradiation. It indicates that the UV-irradiation influences the system to some degree, most likely due to (local) heating of the system that faciliates slight permialization of the membrane of the liposomes.

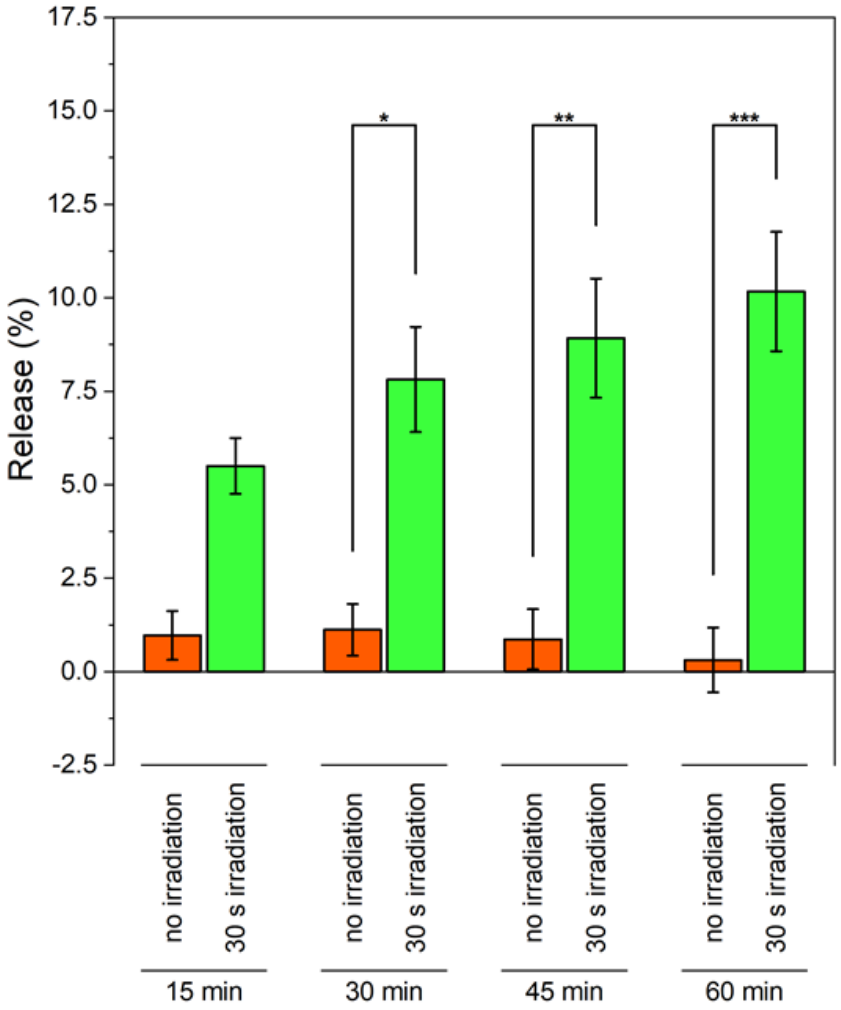

Figure 5.5 - Liposomes without and with MM (1:50) with irradiation for 30 seconds of which the calcein release was studied at fixed time-points using fluorescence spectroscopy. Measurements are average ± SE of three independent experiments. Data was analyzed by analysis of variance (ANOVA) and Tukey's test. Significances are indicated with * for p-value < 0.05, ** for p-value < 0.01 and *** for p-value < 0.001.
Source: By the author.

To identify the amount of control on the release, a higher irradiation time was investigated. By increasing the amount of irradiation, dosage, either by time or intensity, the molecular motors would provide more molecular rotatory motion. Liposomes from the same batch prepared with a lipid to MM ratio of 50:1 was subjected to 0, 30, and 60 seconds of UV-irradiation and the fluorescence was analyzed over time (Figure 5.6). It is clearly visible that upon increasing the irradiation time, the release of calcein is increased. This difference in the release profile simply by adjusting the dosing of UV-irradiation illustrates the ease of control over such a system. It enables us to

appropriately tailor the amount of molecular components to meet either the required dosing for an active compound to function, or to control the release over several events. It has to be noted that longer irradiation times were avoided as well as repetitive irradiation as it inflicted photo-bleaching on calcein. For future studies, other non-bleaching moieties should be used, as well as molecular motors that respond to visible light rather than UV-light should be used, which do not inflict oxidative alterations to the molecular structure.

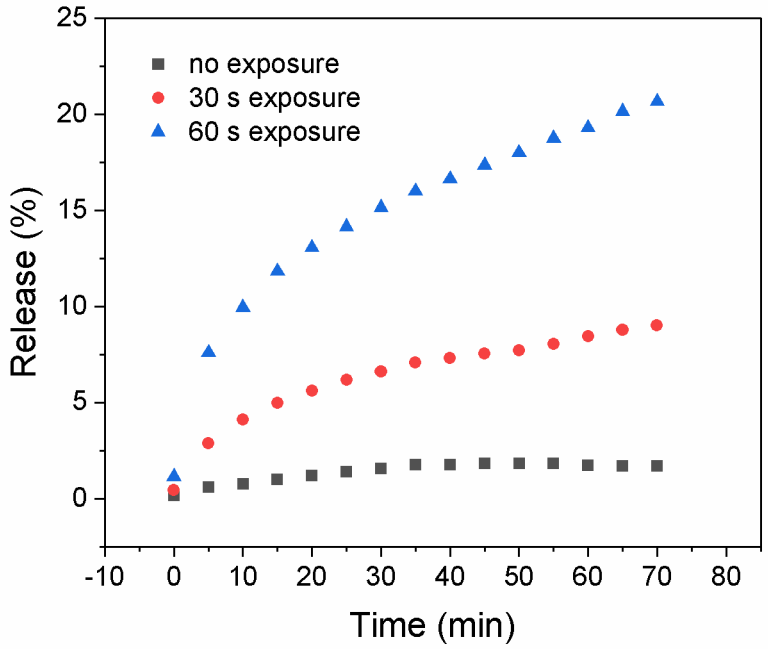

Figure 5.6 - Liposomes with MM (1:50) without irradiation and with irradiation for 30 and 60 seconds of which the calcein release was studied using fluorescence spectroscopy.
Source: By the author.

5.4 CONCLUSION

Redesigning new NCs may be a challenge, but it is important to advance the field of nanomedicine and facilitate controlled active, on-demand delivery at the right location at the right time. However, while still many new materials are under development and far from the clinical application, novel, straightforward approaches will provide the opportunity to impact the nanomedicine and controlled release field in an immediate fashion. By bringing together the well-established and clinically relevant liposomal nanocarrier system with the sophisticated responsive small molecular rotating motor,

new innovative approaches for controlled release are possible. Here we show that the UV-induced rotation of a hydrophobic molecular motor, stored inside the lipid membrane, disrupts the membrane to such extent that small molecules (calcein) are released. This release only occurs in the presence of the molecular motor and combined with UV-irradiation. Without either the molecular motor or the UV-irradiation no significant release was found. By increasing the irradiation dosing or time, higher release occurred and indicated that with this relative simple approach a high degree of control can be obtained. The incorporation of such approach is not limited to phospholipid systems but is also envisioned to be compatible with novel responsive polymer-based NCs. Therefore, our approach does not only impact the immediate biomedical nanocarrier systems but also those that will become clinically relevant in the future. By further tuning the system by using visible light, it is possible to reduce potential oxidative damages due to irradiation, allowing biocompatibility with biological systems that generally poorly tolerate UV-irradiation.

REFERENCES

1 TORCHILIN, V. P. Multifunctional nanocarriers. **Advanced Drug Delivery Reviews**, v. 58, n. 14, p. 1532–1555, 2006.

2 LE DROUMAGUET, B. *et al*. Versatile and efficient targeting using a single nanoparticulate platform: application to cancer and Alzheimer's disease. **ACS Nano**, v. 6, n. 7, p. 5866–5879, 2012.

3 SOBOT, D. *et al*. Conjugation of squalene to gemcitabine as unique approach exploiting endogenous lipoproteins for drug delivery. **Nature Communications**, v. 8, n. 1, p. 15678, 2017.

4 LAM, F. C. *et al*. Enhanced efficacy of combined temozolomide and bromodomain inhibitor therapy for gliomas using targeted nanoparticles. **Nature Communications**, v. 9, n. 1, p. 1991, 2018.

5 PAPACHRISTODOULOU, A. *et al*. Chemotherapy sensitization of glioblastoma by focused ultrasound-mediated delivery of therapeutic liposomes. **Journal of Controlled Release**, v. 295, p. 130–139, 2019.

6 MARANGONI, V. S. *et al*. Photothermia and activated drug release of natural cell membrane coated plasmonic gold nanorods and β-Lapachone. **ACS Applied Bio Materials**, v. 2, n. 2, p. 728–736, 2019.

7 LI, Y. *et al*. A smart and versatile theranostic nanomedicine platform based on nanoporphyrin. **Nature Communications**, v. 5, n. 1, p. 4712, 2014.

8 ANDERSON, C. F.; CUI, H. Protease-sensitive nanomaterials for cancer therapeutics and imaging. **Industrial & Engineering Chemistry Research**, v. 56, n. 20, p. 5761–5777, 2017.

9 MOKABBER, T. *et al*. Antimicrobial electrodeposited silver-containing calcium phosphate coatings. **ACS Applied Materials & Interfaces**, v. 12, n. 5, p. 5531–5541, 2020.

10 SONDI, I.; SALOPEK-SONDI, B. Silver nanoparticles as antimicrobial agent: a case study on E. coli as a model for Gram-negative bacteria. **Journal of Colloid and Interface Science**, v. 275, n. 1, p. 177–182, 2004.

11 ROZENBAUM, R. T. *et al*. Antimicrobial synergy of monolaurin lipid nanocapsules with adsorbed antimicrobial peptides against Staphylococcus aureus biofilms in vitro is absent in vivo. **Journal of Controlled Release**, v. 293, p. 73–83, 2019. DOI: 10.1016/j.jconrel.2018.11.018.

12 BALLESTEROS, C. A. S. *et al*. Controlled release of silver nanoparticles contained in photoresponsive nanogels. **ACS Applied Bio Materials**, v. 2, n. 2, p. 644–653, 2019.

13 HEMELAAR, S. R. *et al*. The response of HeLa Cells to fluorescent nanodiamond uptake. **Sensors (Basel, Switzerland)**, v. 18, n. 2, p. 355, 2018.

14 MARANGONI, V. S. *et al*. Enhancing T₁ magnetic resonance imaging contrast with internalized gadolinium(III) in a multilayer nanoparticle. **Proceedings of the National Academy of Sciences**, v. 114, n. 27, p. 6960 LP – 6965, 2017.

15 REUL, R. *et al*. Near infrared labeling of PLGA for in vivo imaging of nanoparticles. **Polymer Chemistry**, v. 3, n. 3, p. 694–702, 2012.

16 JANEGITZ, B. C. *et al.* The application of graphene for in vitro and in vivo electrochemical biosensing. **Biosensors and Bioelectronics**, 2015.

17 BROSEL-OLIU, S. *et al*. 3D impedimetric sensors as a tool for monitoring bacterial response to antibiotics. **Lab on a Chip**, v. 19, n. 8, p. 1436–1447, 2019.

18 BACCARIN, M. *et al*. Electrochemical sensor based on reduced graphene oxide/carbon black/chitosan composite for the simultaneous determination of dopamine and paracetamol concentrations in urine samples. **Journal of Electroanalytical Chemistry**, v. 799, p. 436–443, 2017.

19 DEGORS, I. M. S. *et al*. Carriers break Barriers in drug delivery: endocytosis and endosomal escape of gene delivery vectors. **Accounts of Chemical Research**, v. 52, n. 7, p. 1750–1760, 2019.

20 GEORGIEVA, J. V; HOEKSTRA, D.; ZUHORN, I. S. Smuggling drugs into the Brain: an overview of ligands targeting transcytosis for drug delivery across the blood-Brain Barrier. **Pharmaceutics**, v. 6, n. 4, p. 557–583, 2014.

21 CURTIS, L. T.; FRIEBOES, H. B. The tumor microenvironment as a Barrier to cancer nanotherapy. *In*: REJNIAK, K. A. (ed.). **Systems biology of tumor microenvironment**: quantitative modeling and simulations. Cham: Springer International Publishing, 2016. p. 165–190.

22 SADOWSKI, G.; RICHTERING, W. **Intelligent hydrogels**. Cham: Springer International Publishing, 2014.

23 PLAMPER, F. A.; RICHTERING, W. Functional microgels and microgel systems. **Accounts of Chemical Research**, v. 50, n. 2, p. 131–140, 2017.

24 CORS, M. *et al*. Deuteration-induced volume phase transition temperature shift of PNIPMAM microgels**. Polymers**, 2019. DOI: 10.3390/polym11040620.

25 WEDEL, B. *et al*. Role of surfactants anionic in the synthesis of smart microgels based on different acrylamides. **ACS Omega**, v. 2, n. 1, p. 84–90, 2017.

26 ANSELMO, A. C. *et al.* Elasticity of nanoparticles influences their blood circulation, phagocytosis, endocytosis, and targeting. **ACS Nano**, v. 9, n. 3, p. 3169–3177, 2015.

27 ZHANG, L. *et al.* Microfluidic synthesis of hybrid nanoparticles with controlled lipid layers: understanding flexibility-regulated cell-nanoparticle interaction. **ACS Nano**, v.9, n.10, p. 9912–9921, 2015.

28 ZHANG, L. *et al*. Softer Zwitterionic nanogels for longer circulation and lower splenic accumulation. **ACS Nano**, v. 6, n. 8, p. 6681–6686, 2012.

29 SUN, J. *et al*. Tunable rigidity of (polymeric core)-(lipid shell) nanoparticles for regulated cellular uptake. **Advanced Materials**, v. 27, n. 8, p. 1402–1407, 2015.

30 SUN, H. *et al*. The role of capsule stiffness on cellular processing. **Chemical Science**, v. 6, n. 6, p. 3505–3514, 2015.

31 HARTMANN, R. *et al*. Stiffness-dependent in vitro uptake and lysosomal acidification of colloidal particles. **Angewandte Chemie International Edition**, v. 54, n. 4, p. 1365–1368, 2015.

32 LIU, W. *et al*. Uptake of hydrogel particles with different stiffness and its influence on HepG2 cell functions. **Soft Matter**, v. 8, n. 35, p. 9235–9245, 2012.

33 ALEXANDER, J. F. *et al*. Cubical shape enhances the interaction of layer-by-layer polymeric particles with breast cancer cells. **Advanced Healthcare Materials**, v. 4, n. 17, p. 2657–2666, 2015.

34 BENINGO, K. A.; WANG, Y. L. Fc-receptor-mediated phagocytosis is regulated by mechanical properties of the target. **Journal of Cell Science**, v. 115, Pt, 4, p. 849, 2002.

35 CUI, J. *et al*. Mechanically tunable, self-adjuvanting nanoengineered polypeptide particles. **Advanced Materials**, v. 25, n. 25, p. 3468–3472, 2013.

36 YU, M. *et al*. Rapid transport of deformation-tuned nanoparticles across biological hydrogels and cellular barriers. **Nature Communications**, v. 9, n. 1, p. 2607, 2018.

37 BANQUY, X. *et al*. Effect of mechanical properties of hydrogel nanoparticles on macrophage cell uptake. **Soft Matter**, v. 5, n. 20, p. 3984–3991, 2009.

38 GUO, P. *et al*. Nanoparticle elasticity directs tumor uptake. **Nature Communications**, v. 9, n. 1, p. 130, 2018.

39 YI, X.; GAO, H. Cell membrane wrapping of a spherical thin elastic shell. **Soft Matter**, v. 11, n. 6, p. 1107–1115, 2015.

40 YI, X.; GAO, H. Kinetics of receptor-mediated endocytosis of elastic nanoparticles. **Nanoscale**, v. 9, n. 1, p. 454–463, 2017.

41 VERNEREY, F. J.; FARSAD, M. An Eulerian/XFEM formulation for the large deformation of cortical cell membrane. **Computer Methods in Biomechanics and Biomedical Engineering**, v. 14, n. 5, p. 433–445, 2011.

42 MORA-HUERTAS, C. E.; FESSI, H.; ELAISSARI, A. Polymer-based nanocapsules for drug delivery. **International Journal of Pharmaceutics**, v. 385, n. 1, p. 113–142, 2010.

43 ZOLNIK, B. S.; BURGESS, D. J. Effect of acidic pH on PLGA microsphere degradation and release. **Journal of Controlled Release**, v. 122, n. 3, p. 338–344, 2007.

44 PASSERINI, N.; CRAIG, D. Q. M. An investigation into the effects of residual water on the glass transition temperature of polylactide microspheres using modulated temperature DSC. **Journal of Controlled Release**, v. 73, n. 1, p. 111–115, 2001.

45 CHUNG, T.-W. *et al*. Different ratios of lactide and glycolide in PLGA affect the surface property and protein delivery characteristics of the PLGA microspheres with hydrophobic additives. **Journal of Microencapsulation**, v. 23, n. 1, p. 15–27, 2006.

46 FESSI, H. *et al*. Nanocapsule formation by interfacial polymer deposition following solvent displacement. **International Journal of Pharmaceutics**, v. 55, n. 1, p. R1–R4, 1989.

47 MILADI, K. *et al*. Nanoprecipitation process: from particle preparation to in vivo applications. *In*: VAUTHIER, C.; PONCHEL, G. (ed.). **Polymer nanoparticles for nanomedicines**: a guide for their design, preparation and development. Cham: Springer International Publishing, 2016. p. 17–53.

48 SCRIVEN, L. E.; STERNLING, C. V. The Marangoni effects. **Nature**, v. 187, n. 4733, p. 186–188, 1960.

49 TORCHILIN, V. P. *et al*. Amphiphilic poly-N-vinylpyrrolidones: synthesis, properties and liposome surface modification. **Biomaterials**, v. 22, n. 22, p. 3035–3044, 2001.

50 MALAM, Y.; LOIZIDOU, M.; SEIFALIAN, A. M. Liposomes and nanoparticles: nanosized vehicles for drug delivery in cancer. **Trends in Pharmacological Sciences**, v. 30, n. 11, p. 592–599, 2009.

51 NEMOTO, R. et al. Liposomes with temperature-responsive reversible surface properties. **Colloids and Surfaces B:** biointerfaces, v. 176, p. 309–316, 2019.

52 TA, T.; PORTER, T. M. Thermosensitive liposomes for localized delivery and triggered release of chemotherapy. **Journal of Controlled Release:** official journal of the controlled release society, v. 169, n. 1–2, p. 112–125, 2013.

53 KNEIDL, B. *et al*. Thermosensitive liposomal drug delivery systems: state of the art review. **International Journal of Nanomedicine**, v. 9, p. 4387–4398, 2014.

54 SCHROEDER, A. *et al.* Controlling liposomal drug release with low frequency ultrasound: mechanism and feasibility. **Langmuir**, v. 23, n. 7, p. 4019–4025, 2007.

55 CHANDAN, R.; BANERJEE, R. Pro-apoptotic liposomes-nanobubble conjugate synergistic with paclitaxel: a platform for ultrasound responsive image-guided drug delivery. **Scientific Reports**, v. 8, n. 1, p. 2624, 2018.

56 DE MATOS, M. B. C. *et al*. Ultrasound-sensitive liposomes for triggered macromolecular drug delivery: formulation and in vitro characterization. **Frontiers in Pharmacology**, 2019. DOI: 10.3389/fphar.2019.01463.

57 MIRANDA, D. *et al.* Detection of sunlight exposure with solar-sensitive liposomes that capture and release food dyes. **ACS Applied Nano Materials**, v. 1, n. 6, p. 2739–2747, 2018.

58 LEUNG, S. J.; ROMANOWSKI, M. Light-activated content release from liposomes. **Theranostics**, v. 2, n. 10, p. 1020–1036, 2012.

59 MATHIYAZHAKAN, M.; WIRAJA, C.; XU, C. A concise review of gold nanoparticles-based photo-responsive liposomes for controlled drug delivery. **Nano-Micro Letters**, v. 10, n. 1, p. 10, 2017.

60 FAN, Y. *et al*. Study of the pH-sensitive mechanism of tumor-targeting liposomes. **Colloids and Surfaces B:** biointerfaces, v. 151, p. 19–25, 2017.

61 SIMÕES, S. *et al*. On the formulation of pH-sensitive liposomes with long circulation times. **Advanced Drug Delivery Reviews**, v. 56, n. 7, p. 947–965, 2004.

62 ONG, W. *et al*. Redox-triggered contents release from liposomes. **Journal of the American Chemical Society**, v. 130, n. 44, p. 14739–14744, 2008.

63 LI, J. *et al*. Dual redox/pH-responsive hybrid polymer-lipid composites: synthesis, preparation, characterization and application in drug delivery with enhanced therapeutic efficacy. **Chemical Engineering Journal**, v. 341, p. 450–461, 2018.

64 LEE, Y.; THOMPSON, D. H. Stimuli-responsive liposomes for drug delivery. **Wiley interdisciplinary Reviews Nanomedicine and Nanobiotechnology**, v. 9, n. 5, p. 10.1002/wnan.1450, 2017.

65 AN, X.; ZHAN, F.; ZHU, Y. Smart photothermal-triggered bilayer phase transition in AuNPs–liposomes to release drug. **Langmuir**, v. 29, n. 4, p. 1061–1068, 2013.

66 KWON, H. J. *et al*. Gold cluster-labeled thermosensitive liposmes enhance triggered drug release in the tumor microenvironment by a photothermal effect. **Journal of Controlled Release**, v. 216, p. 132–139, 2015.

67 YAVLOVICH, A. *et al*. A novel class of photo-triggerable liposomes containing DPPC:DC8,9PC as vehicles for delivery of doxorubcin to cells. **Biochimica et Biophysica Acta (BBA) -** biomembranes, v. 1808, n. 1, p. 117–126, 2011.

68 CHANDRA, B.; MALLIK, S.; SRIVASTAVA, D. K. Design of photocleavable lipids and their application in liposomal “uncorking”. **Chemical Communications**, n. 24, p. 3021–3023, 2005.

69 BAYER, A. M. *et al.* Triggered liposomal release through a synthetic phosphatidylcholine analogue bearing a photocleavable moiety embedded within the sn-2 Acyl chain. **Chemistry – A European Journal**, v. 20, n. 12, p. 3350–3357, 2014.

70 YAO, C. *et al*. Near-infrared-triggered azobenzene-liposome/upconversion nanoparticle hybrid vesicles for remotely controlled drug delivery to overcome cancer multidrug resistance. **Advanced Materials**, v. 28, n. 42, p. 9341–9348, 2016.

71 SCHIMKA, S. *et al*. Photo-isomerization of azobenzene containing surfactants induced by near-infrared light using upconversion nanoparticles as mediator. **Journal of Physics:** condensed matter, v. 31, n. 12, p. 125201, 2019.

72 KOÇER, A. *et al*. A light-actuated nanovalve derived from a channel protein. **Science**, v. 309, n. 5735, p. 755 LP – 758, 2005.

73 CUI, Z.-K. *et al*. Nonphospholipid fluid liposomes with switchable photocontrolled release. **Langmuir**, v. 30, n. 36, p. 10818–10825, 2014.

74 YAVLOVICH, A. *et al*. Light-sensitive lipid-based nanoparticles for drug delivery: design principles and future considerations for biological applications. **Molecular Membrane Biology**, v. 27, n. 7, p. 364–381, 2010.

75 LUBBE, A. S. *et al*. Molecular motors in aqueous environment. **Journal of Organic Chemistry**, v. 83, n. 18, p. 11008–11018, 2018.

76 FERINGA, B. L. The art of building small: from molecular switches to motors (Nobel Lecture). **Angewandte Chemie International Edition**, v. 56, n. 37, p. 11060–11078, 2017.

77 CHENG, Y. *et al.* Blood-Brain Barrier permeable gold nanoparticles: an efficient delivery platform for enhanced malignant glioma therapy and imaging. **Small**, v. 10, n. 24, p. 5137–5150, 2014.

78 SELA, H. *et al*. Spontaneous penetration of gold nanoparticles through the blood brain barrier (BBB). **Journal of Nanobiotechnology**, v. 13, n. 1, p. 71, 2015.

79 VORBRODT, A. W. Ultracytochemical characterization of anionic sites in the wall of brain capillaries. **Journal of Neurocytology**, v. 18, n. 3, p. 359–368, 1989.

80 GEORGIEVA, J. V. *et al*. Surface characteristics of nanoparticles determine their intracellular fate in and processing by human blood–brain Barrier endothelial cells in vitro. **Molecular Therapy**, v. 19, n. 2, p. 318–325, 2011.

81 CHANG, J. *et al*. Characterization of endocytosis of transferrin-coated PLGA nanoparticles by the blood–brain barrier. **International Journal of Pharmaceutics**, v. 379, n. 2, p. 285–292, 2009.

82 JIANG, X. *et al*. Nanoparticles of 2-deoxy-d-glucose functionalized poly(ethylene glycol)-co-poly(trimethylene carbonate) for dual-targeted drug delivery in glioma treatment. **Biomaterials**, v. 35, n. 1, p. 518–529, 2014.

83 WILEY, D. T. *et al*. Transcytosis and brain uptake of transferrin-containing nanoparticles by tuning avidity to transferrin receptor. **Proceedings of the National Academy of Sciences**, v. 110, n. 21, p. 8662 LP – 8667, 2013.

84 DE JONG, E. *et al*. A filter-free blood-brain barrier model to quantitatively study transendothelial delivery of nanoparticles by fluorescence spectroscopy. **Journal of Controlled Release**, v. 289, p. 14–22, 2018.

85 STOJANOV, K. *et al*. In Vivo Biodistribution of prion- and GM1-targeted polymersomes following intravenous administration in Mice. **Molecular Pharmaceutics**, v. 9, n. 6, p. 1620–1627, 2012.

86 GEORGIEVA, J. V. *et al.* Peptide-mediated blood–brain barrier transport of polymersomes. **Angewandte Chemie International Edition**, v. 51, n. 33, p. 8339–8342, 2012.

87 YU, Y. J. *et al*. Boosting brain uptake of a therapeutic antibody by reducing its affinity for a transcytosis target. **Science Translational Medicine**, v. 3, n. 84, p. 84ra44 LP-84ra44, 2011.

88 GRIFNO, G. N. *et al.* Tissue-engineered blood-brain barrier models via directed differentiation of human induced pluripotent stem cells. **Scientific Reports**, v. 9, n. 1, p. 13957, 2019.

89 BOOTH, R.; KIM, H. Characterization of a microfluidic in vitro model of the blood-brain barrier (μBBB). **Lab on a Chip**, v. 12, n. 10, p. 1784–1792, 2012.

90 GRIEP, L. M. *et al*. BBB ON CHIP: microfluidic platform to mechanically and biochemically modulate blood-brain barrier function. **Biomedical Microdevices**, v. 15, n. 1, p. 145–150, 2013.

91 HERLAND, A. *et al.* Distinct contributions of astrocytes and pericytes to neuroinflammation identified in a 3D human blood-brain barrier on a chip. **PloS ONE**, v. 11, n. 3, p. e0150360–e0150360, 2016.

92 BERGMANN, S. *et al*. Blood–brain-barrier organoids for investigating the permeability of CNS therapeutics. **Nature Protocols**, v. 13, n. 12, p. 2827–2843, 2018.

93 DESTEFANO, J. G. *et al*. Benchmarking in vitro tissue-engineered blood–brain barrier models. **Fluids and Barriers of the CNS**, v. 15, n. 1, p. 32, 2018.

94 SIVANDZADE, F.; CUCULLO, L. In-vitro blood–brain barrier modeling: A review of modern and fast-advancing technologies. **Journal of Cerebral Blood Flow & Metabolism**, v. 38, n. 10, p. 1667–1681, 2018.

95 CECCHELLI, R. *et al.* Modelling of the blood–brain barrier in drug discovery and development. **Nature Reviews Drug Discovery**, v. 6, n. 8, p. 650–661, 2007.

96 HELMS, H. C. *et al*. In vitro models of the blood–brain barrier: An overview of commonly used brain endothelial cell culture models and guidelines for their use. **Journal of Cerebral Blood Flow & Metabolism**, v. 36, n. 5, p. 862–890, 2016.

97 YE, D. *et al.* Nanoparticle accumulation and transcytosis in brain endothelial cell layers. **Nanoscale**, v. 5, n. 22, p. 11153–11165, 2013.

98 PEER, D. *et al.* Nanocarriers as an emerging platform for cancer therapy. **Nature Nanotechnology**, v. 2, n. 12, p. 751–760, 2007.

99 FAROKHZAD, O. C.; LANGER, R. Impact of Nanotechnology on Drug Delivery. **ACS Nano**, v. 3, n. 1, p. 16–20, 2009.

100 SHI, J. et al. Nanotechnology in drug delivery and tissue engineering: from discovery to applications. **Nano Letters**, v. 10, n. 9, p. 3223–3230, 2010.

101 WANG, A. Z.; LANGER, R.; FAROKHZAD, O. C. Nanoparticle delivery of cancer drugs. **Annual Review of Medicine**, v. 63, n. 1, p. 185–198, 2012.

102 FERNANDES, C.; SUARES, D.; YERGERI, M. C. Tumor microenvironment targeted nanotherapy, **Frontiers in Pharmacology**, 2018. DOI: 10.3389/fphar.2018.01230

103 EDIRIWICKREMA, A.; SALTZMAN, W. M. Nanotherapy for Cancer: targeting and multifunctionality in the future of cancer therapies. **ACS Biomaterials Science & Engineering**, v. 1, n. 2, p. 64–78, 2015.

104 KIM, G. J.; NIE, S. Targeted cancer nanotherapy. **Materials Today**, v. 8, n. 8, Supplement, p. 28–33, 2005.

105 GARNIS, C.; BUYS, T. P. H.; LAM, W. L. Genetic alteration and gene expression modulation during cancer progression. **Molecular cancer**, v. 3, p. 9, 2004.

106 TESTA, U.; CASTELLI, G.; PELOSI, E. Genetic abnormalities, clonal evolution, and cancer stem cells of brain tumors. **Medical sciences (Basel, Switzerland)**, v. 6, n. 4, p. 85, 2018.

107 RUSCIANO, D.; WELCH, D. R.; BURGER, M. M. Homotypic and heterotypic cell adhesion in metastasis. *In:* RUSCIANO, D.; WELCH, D. R.; BURGER, M. M (ed.). **Cancer metastasis:** in vitro and in vivo experimental approaches. Berlin: Elsevier, 2000. p. 9–64. (Laboratory techniques in biochemistry and molecular biology, v. 29)

108 FANG, R. H. *et al*. Cancer cell membrane-coated nanoparticles for anticancer vaccination and drug delivery. **Nano Letters**, v. 14, n. 4, p. 2181–2188, 2014.

109 LIU, Y. *et al.* Cell membrane coating technology: a promising strategy for biomedical applications. **Nano-Micro Letters**, v. 11, n. 1, p. 100, 2019.

110 QIAN, B.-Z.; POLLARD, J. W. Macrophage diversity enhances tumor progression and metastasis. **Cell**, v. 141, n. 1, p. 39–51, 2010.

111 MARTINEZ, F. O.; GORDON, S. The M1 and M2 paradigm of macrophage activation: time for reassessment. **F1000prime Reports**, v. 6, p. 13, 2014.

112 PRIONISTI, I. *et al.* Harnessing microglia and macrophages for the treatment of glioblastoma. **Frontiers in Pharmacology**, 2019. DOI: 10.3389/fphar.2019.00506

113 HAMBARDZUMYAN, D.; GUTMANN, D. H.; KETTENMANN, H. The role of microglia and macrophages in glioma maintenance and progression. **Nature Neuroscience**, v. 19, n. 1, p. 20–27, 2016.

114 GABRUSIEWICZ, K. *et al*. Glioblastoma-infiltrated innate immune cells resemble M0 macrophage phenotype. **JCI insight**, v. 1, n. 2, p. e85841, 2016.

115 LIN, A. *et al*. Shear-regulated uptake of nanoparticles by endothelial cells and development of endothelial-targeting nanoparticles. **Journal of biomedical materials research. Part A**, v. 93, n. 3, p. 833–842, 2010.

116 HO, Y. T.; KAMM, R. D.; KAH, J. C. Y. Influence of protein corona and caveolae-mediated endocytosis on nanoparticle uptake and transcytosis. **Nanoscale**, v. 10, n. 26, p. 12386–12397, 2018.

117 SHILO, M. *et al*. The effect of nanoparticle size on the probability to cross the blood-brain barrier: an in-vitro endothelial cell model. **Journal of nanobiotechnology**, v. 13, p. 19, 2015.

118 BETZER, O. *et al.* The effect of nanoparticle size on the ability to cross the blood–brain barrier: an in vivo study. **Nanomedicine**, v. 12, n. 13, p. 1533–1546, 2017.

119 SUN, W. *et al.* Specific role of polysorbate 80 coating on the targeting of nanoparticles to the brain. **Biomaterials**, v. 25, n. 15, p. 3065–3071, 2004.

120 DAL MAGRO, R. *et al*. ApoE-modified solid lipid nanoparticles: a feasible strategy to cross the blood-brain barrier. **Journal of Controlled Release**, v. 249, p. 103–110, 2017.

121 OHTSUKI, S.; TERASAKI, T. Contribution of carrier-mediated transport systems to the blood–brain barrier as a supporting and protecting interface for the brain; importance for CNS drug discovery and development. **Pharmaceutical Research**, v. 24, n. 9, p. 1745–1758, 2007.

122 NEVES, A. R. *et al*. Apo E-functionalization of solid lipid nanoparticles enhances brain drug

delivery: uptake mechanism and transport pathways. **Bioconjugate Chemistry**, v. 28, n. 4, p. 995–1004, 2017.

123 ZENSI, A. *et al*. Albumin nanoparticles targeted with Apo E enter the CNS by transcytosis and are delivered to neurones. **Journal of Controlled Release:** official journal of the controlled release society, v. 137, n. 1, p. 78–86, 2009.

124 HUI, Y. *et al*. Understanding the effects of nanocapsular mechanical property on passive and active tumor targeting. **ACS Nano**, v. 12, n. 3, p. 2846–2857, 2018.

125 ZHAO, J. *et al*. Length vs. stiffness: which plays a dominant role in the cellular uptake of fructose-based rod-like micelles by breast cancer cells in 2D and 3D cell culture models? **Journal of Materials Chemistry B**, v. 6, n. 25, p. 4223–4231, 2018.

126 ANSELMO, A. C.; MITRAGOTRI, S. Impact of particle elasticity on particle-based drug delivery systems. **Advanced Drug Delivery Reviews**, v. 108, p. 51–67, 2017.

127 HUI, Y. *et al*. Role of Nanoparticle Mechanical Properties in Cancer Drug Delivery. **ACS Nano**, v. 13, n. 7, p. 7410–7424, 2019.

128 WANG, S. *et al*. Penetration of nanoparticles across a lipid bilayer: effects of particle stiffness and surface hydrophobicity. **Nanoscale**, v. 11, n. 9, p. 4025–4034, 2019.

129 MERKEL, T. J. *et al*. Using mechanobiological mimicry of red blood cells to extend circulation times of hydrogel microparticles. **Proceedings of the National Academy of Sciences**, v. 108, n. 2, p. 586 LP – 591, 2011.

130 YI, X.; SHI, X.; GAO, H. Cellular uptake of elastic nanoparticles. **Physical Review Letters**, v. 107, n. 9, p. 98101, 2011.

131 OBST, K. *et al*. Protein corona formation on colloidal polymeric nanoparticles and polymeric nanogels: impact on cellular uptake, toxicity, immunogenicity, and drug release properties. **Biomacromolecules**, v. 18, n. 6, p. 1762–1771, 2017.

132 MICELI, E. *et al*. Understanding the elusive protein corona of thermoresponsive nanogels. **Nanomedicine**, v. 13, n. 20, p. 2657–2668, 2018.

133 KESKIN, D. *et al.* Inhibiting bacterial adhesion by mechanically modulated microgel coatings. **Biomacromolecules**, v. 20, n. 1, p. 243–253, 2019.

134 SCHINDELIN, J. *et al*. Fiji: an open-source platform for biological-image analysis. **Nature Methods**, v. 9, n. 7, p. 676–682, 2012.

135 DOS SANTOS, T. *et al.* Quantitative assessment of the comparative nanoparticle-uptake efficiency of a range of cell lines. **Small**, v. 7, n. 23, p. 3341–3349, 2011.

136 WEDEL, B. *et al*. geSmart Homopolymer Microgels: Influence of the Monomer Structure on the Particle Properties, **Polymers**, 2016.

137 NOWAK, M. *et al*. Size, shape, and flexibility influence nanoparticle transport across brain endothelium under flow. **Bioengineering & Translational Medicine**, v. n/a, n. n/a, p. e10153, 2019.

138 SHEN, Z. *et al*. Membrane wrapping efficiency of elastic nanoparticles during endocytosis: size and shape matter. **ACS Nano**, v. 13, n. 1, p. 215–228, 2019.

139 FREESE, C. *et al.* Uptake of poly(2-hydroxypropylmethacrylamide)-coated gold nanoparticles in microvascular endothelial cells and transport across the blood–brain barrier. **Biomaterials Science**, v. 1, n. 8, p. 824–833, 2013.

140 HAQQANI, A. S. *et al*. Intracellular sorting and transcytosis of the rat transferrin receptor antibody OX26 across the blood–brain barrier in vitro is dependent on its binding affinity. **Journal of Neurochemistry**, v. 146, n. 6, p. 735–752, 2018.

141 COOPER, P. R. *et al*. Efflux of monoclonal antibodies from rat brain by neonatal Fc receptor, FcRn. **Brain Research**, v. 1534, p. 13–21, 2013.

142 DEMEULE, M. *et al*. High transcytosis of melanotransferrin (P97) across the blood–brain barrier. **Journal of Neurochemistry**, v. 83, n. 4, p. 924–933, 1 nov. 2002.

143 CLARK, A. J.; DAVIS, M. E. Increased brain uptake of targeted nanoparticles by adding an acid-cleavable linkage between transferrin and the nanoparticle core. **Proceedings of the National Academy of Sciences**, v. 112, n. 40, p. 12486 LP – 12491, 2015.

144 MICELI, E.; KAR, M.; CALDERÓN, M. Interactions of organic nanoparticles with proteins in physiological conditions. **Journal of Materials Chemistry B**, v. 5, n. 23, p. 4393–4405, 2017.

145 LINDMAN, S. *et al.* Systematic investigation of the thermodynamics of HSA adsorption to N-iso-Propylacrylamide/N-tert-Butylacrylamide copolymer nanoparticles. effects of particle size and hydrophobicity. **Nano Letters**, v. 7, n. 4, p. 914–920, 2007.

146 PEREIRA, P. *et al.* Biocompatibility of a self-assembled glycol chitosan nanogel. **Toxicology in Vitro**, v. 29, n. 3, p. 638–646, 2015.

147 BEWERSDORFF, T. *et al*. Amphiphilic nanogels: influence of surface hydrophobicity on protein corona, biocompatibility and cellular uptake. **International journal of nanomedicine**, v. 14, p. 7861–7878, 2019.

148 GUTMANN, D. H.; KETTENMANN, H. Microglia/Brain macrophages as central drivers of brain tumor pathobiology. **Neuron**, v. 104, n. 3, p. 442–449, 2019.

149 HUTTER, G. *et al*. Microglia are effector cells of CD47-SIRPα antiphagocytic axis disruption against glioblastoma. **Proceedings of the National Academy of Sciences**, v. 116, n. 3, p. 997 LP – 1006, 2019.

150 MURDOCH, C. *et al.* The role of myeloid cells in the promotion of tumour angiogenesis. **Nature Reviews Cancer**, v. 8, n. 8, p. 618–631, 2008.

151 LIN, E. Y. *et al*. Macrophages regulate the angiogenic switch in a mouse model of breast cancer. **Cancer Research**, v. 66, n. 23, p. 11238 LP – 11246, 2006.

152 BRANDENBURG, S. *et al*. Resident microglia rather than peripheral macrophages promote vascularization in brain tumors and are source of alternative pro-angiogenic factors. **Acta Neuropathologica**, v. 131, n. 3, p. 365–378, 2016.

153 GUADAGNO, E. *et al*. Role of macrophages in brain tumor growth and progression. **International Journal of Molecular Sciences**, v. 19, n. 4, p. 1005, 2018.

154 ROGGENDORF, W.; STRUPP, S.; PAULUS, W. Distribution and characterization of microglia/macrophages in human brain tumors. **Acta Neuropathologica**, v. 92, n. 3, p. 288–293, 1996.

155 DUHAMEL, M. *et al.* Paclitaxel treatment and PC1/3 knockdown in macrophages is a promising anti-glioma strategy as revealed by proteomics and cytotoxicity studies. **Molecular & Cellular Proteomics**, p. mcp.RA117.000443, 2018. DOI: 10.1074/mcp.RA117.000443.

156 SOMA, C. E. *et al*. Investigation of the role of macrophages on the cytotoxicity of doxorubicin and doxorubicin-loaded nanoparticles on M5076 cells in vitro. **Journal of Controlled Release**, v. 68, n. 2, p. 283–289, 2000.

157 HSU, Y.-C. *et al*. Reduced phagocytosis of colloidal carriers using soluble CD47. **Pharmaceutical Research**, v. 20, n. 10, p. 1539–1542, 2003.

158 HU, C.-M. J. *et al.* 'Marker-of-self' functionalization of nanoscale particles through a top-down cellular membrane coating approach. **Nanoscale**, v. 5, n. 7, p. 2664–2668, 2013.

159 BROWN, E. J.; FRAZIER, W. A. Integrin-associated protein (CD47) and its ligands. **Trends in Cell Biology**, v. 11, n. 3, p. 130–135, 2001.

160 LIU, X. *et al.* Is CD47 an innate immune checkpoint for tumor evasion? **Journal of Hematology & Oncology**, v. 10, n. 1, p. 12, 2017.

161 TAKIMOTO, C. H. *et al*. The Macrophage 'Do not eat me' signal, CD47, is a clinically validated cancer immunotherapy target. **Annals of Oncology**, v. 30, n. 3, p. 486–489, 2019.

162 BAZILE, D. et al. Stealth Me. PEG-PLA Nanoparticles Avoid Uptake by the Mononuclear Phagocytes System. **Journal of Pharmaceutical Sciences**, v. 84, n. 4, p. 493–498, 1995.

163 PERRY, J. L. *et al*. PEGylated PRINT nanoparticles: the impact of PEG density on protein binding, macrophage association, biodistribution, and pharmacokinetics. **Nano Letters**, v. 12, n. 10, p. 5304–5310, 2012.

164 PERRAULT, S. D. *et al*. Mediating tumor targeting efficiency of nanoparticles through design. **Nano Letters**, v. 9, n. 5, p. 1909–1915, 2009.

165 HU, G. *et al*. Nanoparticles targeting macrophages as potential clinical therapeutic agents against cancer and inflammation. **Frontiers in Immunology**, 2019. DOI: 10.3389/fimmu.2019.01998

166 LI, S. *et al*. Nanomedicine engulfed by macrophages for targeted tumor therapy. **International Journal of Nanomedicine**, v. 11, p. 4107–4124, 2016.

167 AIZIK, G. *et al.* Liposomes of quantum dots configured for passive and active delivery to tumor tissue. **Nano Letters**, v. 19, n. 9, p. 5844–5852, 2019.

168 PANG, L. *et al*. Exploiting macrophages as targeted carrier to guide nanoparticles into glioma. **Oncotarget**, v. 7, n. 24, p. 37081–37091, 2016.

169 KWON, D. *et al*. Extra-large pore mesoporous silica nanoparticles for directing in vivo M2 macrophage polarization by delivering IL-4. **Nano Letters**, v. 17, n. 5, p. 2747–2756, 2017.

170 CHAMPION, J. A.; WALKER, A.; MITRAGOTRI, S. Role of particle size in phagocytosis of polymeric microspheres. **Pharmaceutical Research**, v. 25, n. 8, p. 1815–1821,2008.

171 HOEK, E. M. V; BHATTACHARJEE, S.; ELIMELECH, M. Effect of membrane surface roughness on colloid−membrane DLVO interactions. **Langmuir**, v. 19, n. 11, p. 4836–4847, 2003.

172 KOMOHARA, Y. *et al*. Possible involvement of the M2 anti-inflammatory macrophage phenotype in growth of human gliomas. **Journal of Pathology**, v. 216, n. 1, p. 15–24, 2008.

173 LARIONOVA, I. *et al.* Interaction of tumor-associated macrophages and cancer chemotherapy. **Oncoimmunology**, v. 8, n. 7, p. 1596004, 2019.

174 QIE, Y. *et al.* Surface modification of nanoparticles enables selective evasion of phagocytic clearance by distinct macrophage phenotypes. **Scientific Reports**, v. 6, n. 1, p. 26269, 2016.

175 BINNEMARS-POSTMA, K. A. *et al*. Differential uptake of nanoparticles by human M1 and M2 polarized macrophages: protein corona as a critical determinant. **Nanomedicine**, v. 11, n. 22, p. 2889–2902, 2016.

176 WALKEY, C. D. *et al.* Nanoparticle Size and surface chemistry determine serum protein adsorption and macrophage uptake. **Journal of the American Chemical Society**, v. 134, n. 4, p. 2139–2147, 2012.

177 SZULZEWSKY, F. *et al*. Glioma-associated microglia/macrophages display an expression profile different from M1 and M2 polarization and highly express Gpnmb and Spp1. **PloS ONE**, v. 10, n. 2, p. e0116644–e0116644,2015.

178 OLSON, O. C. *et al*. Tumor-associated macrophages suppress the cytotoxic activity of antimitotic agents. **Cell Reports**, v. 19, n. 1, p. 101–113, 2017.

179 DENARDO, D. G. *et al*. Leukocyte complexity predicts breast cancer survival and functionally regulates response to chemotherapy. **Cancer Discovery**, v. 1, n. 1, p. 54 LP – 67, 1 jun. 2011.

180 ORTH, J. D. *et al*. Analysis of mitosis and antimitotic drug responses in tumors by in vivo microscopy and single-cell pharmacodynamics. **Cancer Research**, v. 71, n. 13, p. 4608 LP – 4616, 2011.

181 BRACCI, L. *et al*. Immune-based mechanisms of cytotoxic chemotherapy: implications for the design of novel and rationale-based combined treatments against cancer. **Cell Death & Differentiation**, v. 21, n. 1, p. 15–25, 2014.

182 WEINBERG, F.; RAMNATH, N.; NAGRATH, D. Reactive oxygen species in the tumor microenvironment: an overview. **Cancers**, v. 11, n. 8, p. 1191, 2019.

183 ZHANG, H. *et al*. Class A1 scavenger receptor modulates glioma progression by regulating M2-like tumor-associated macrophage polarization. **Oncotarget**, v. 7, n. 31, p. 50099–50116, 2016.

184 ZAMUDIO-CUEVAS, Y. *et al*. Monosodium urate crystals induce oxidative stress in human synoviocytes. **Arthritis Research & Therapy**, v. 18, n. 1, p. 117, 2016.

185 FINI, M. A. *et al*. Contribution of uric acid to cancer risk, recurrence, and mortality. **Clinical and translational medicine**, v. 1, n. 1, p. 16, 2012.

186 KOTLA, S.; SINGH, N. K.; RAO, G. N. ROS via BTK-p300-STAT1-PPARγ signaling activation mediates cholesterol crystals-induced CD36 expression and foam cell formation. **Redox biology**, v. 11, p. 350–364, 2017.

187 DUEWELL, P. *et al*. NLRP3 inflammasomes are required for atherogenesis and activated by cholesterol crystals. **Nature**, v. 464, n. 7293, p. 1357–1361, 2010.

188 MIRON, R. J.; BOSSHARDT, D. D. Multinucleated giant cells: good guys or bad guys? **Tissue Engineering Part B:** reviews, v. 24, n. 1, p. 53–65, 2017.

189 MARIANI, E. *et al*. Biomaterials: foreign bodies or tuners for the immune response? **International Journal of Molecular Sciences**, v. 20, n. 3, p. 636, 2019.

190 SCHUMACKER, P. T. Reactive oxygen species in cancer cells: live by the sword, die by the sword. **Cancer Cell**, v. 10, n. 3, p. 175–176, 2006.

191 ACHARYA, A. *et al.* Redox regulation in cancer: a double-edged sword with therapeutic potential. **Oxidative Medicine and Cellular Longevity**, v. 3, p. 702528, 2010.

192 BENEDETTI, S. *et al*. Reactive oxygen species a double-edged sword for mesothelioma. **Oncotarget**, v. 6, n. 19, p. 16848–16865, 2015.

193 ESSLER, S.; DEHNE, N.; BRÜNE, B. Role of sestrin2 in peroxide signaling in macrophages. **FEBS Letters**, v. 583, n. 21, p. 3531–3535, 2009.

194 BAUER, M. *et al.* Human monocytes are severely impaired in base and DNA double-strand break repair that renders them vulnerable to oxidative stress. **Proceedings of the National Academy of Sciences**, v. 108, n. 52, p. 21105 LP – 21110, 2011.

195 CHEN, Z. *et al*. Cellular and molecular identity of tumor-associated macrophages in glioblastoma. **Cancer Research**, v. 77, n. 9, p. 2266 LP – 2278, 2017.

196 LESNIAK, A. *et al*. Nanoparticle adhesion to the cell membrane and its effect on nanoparticle uptake efficiency. **Journal of the American Chemical Society**, v. 135, n. 4, p. 1438–1444, 2013.

197 WIEGAND, T. *et al*. Forces during cellular uptake of viruses and nanoparticles at the ventral side. **Nature Communications**, v. 11, n. 1, p. 32, 2020.

198 CHENG, J. *et al*. Formulation of functionalized PLGA–PEG nanoparticles for in vivo targeted drug delivery. **Biomaterials**, v. 28, n. 5, p. 869–876, 2007.

199 CHANG, J. *et al*. Transferrin adsorption onto PLGA nanoparticles governs their interaction with biological systems from blood circulation to brain cancer cells. **Pharmaceutical Research**, v. 29, n. 6, p. 1495–1505, 2012.

200 FUHRMANN, A. *et al*. Metastatic state of cancer cells may be indicated by adhesion strength. **Biophysical Journal**, v. 112, n. 4, p. 736–745, 2017.

201 GASSMANN, P.; HAIER, J.; NICOLSON, G. L. Cell adhesion and invasion during secondary tumor formation: interactions between tumor cells and host organs. *In*: KAISER, H. E.; NASIR, A. (ed.). **Selected aspects of cancer progression**: metastasis, apoptosis and immune response. Dordrecht: Springer Netherlands, 2008. p. 21–32.

202 ZHANG, Y. *et al*. Macrophage-membrane-coated nanoparticles for tumor-targeted chemotherapy. **Nano Letters**, v. 18, n. 3, p. 1908–1915, 2018.

203 GAO, C. *et al*. Stem-cell-membrane camouflaging on near-infrared photoactivated upconversion nanoarchitectures for in vivo remote-controlled photodynamic therapy. **ACS Applied Materials & Interfaces**, v. 8, n. 50, p. 34252–34260, 2016.

204 LAI, P.-Y. *et al*. Biomimetic stem cell membrane-camouflaged iron oxide nanoparticles for theranostic applications. **RSC Advances**, v. 5, n. 119, p. 98222–98230, 2015.

205 GAO, W. *et al*. Surface functionalization of gold nanoparticles with red blood cell membranes. **Advanced Materials**, v. 25, n. 26, p. 3549–3553, 2013.

206 ROSSI, L. *et al*. Red blood cell membrane processing for biomedical applications. **Frontiers in Physiology** , 2019. DOI: 10.3389/fphys.2019.01070

207 ZHU, D.-M. *et al*. Erythrocyte membrane-coated gold nanocages for targeted photothermal and chemical cancer therapy. **Nanotechnology**, v. 29, n. 8, p. 84002, 2018.

208 PASTO, A. *et al*. Cell membrane protein functionalization of nanoparticles as a new tumor-targeting strategy. **Clinical and Translational Medicine**, v. 8, n. 1, p. 8, 2019.

209 ZHANG, H. *et al*. Biointerface engineering nanoplatforms for cancer-targeted drug delivery. **Asian Journal of Pharmaceutical Sciences**, 2019. DOI: 10.1016/j.ajps.2019.11.004

210 ZHAI, Y. *et al*. Preparation and application of cell membrane-camouflaged nanoparticles for cancer therapy. **Theranostics**, v. 7, n. 10, p. 2575–2592, 2017.

211 HU, C.-M. J. *et al*. Erythrocyte membrane-camouflaged polymeric nanoparticles as a biomimetic delivery platform. **Proceedings of the National Academy of Sciences**, v. 108, n. 27, p. 10980–10985, 2011.

212 SIEGEL, R. L.; MILLER, K. D.; JEMAL, A. Cancer statistics, 2019. **CA:** a cancer journal for clinicians, v. 69, n. 1, p. 7–34, 2019.

213 MEREGHETTI, P. *et al*. A Fourier transform infrared spectroscopy study of cell membrane domain modifications induced by docosahexaenoic acid. **Biochimica et Biophysica Acta (BBA)** - general subjects, v. 1840, n. 10, p. 3115–3122, 2014.

214 ALMEIDA, A. M.; CASTEL-BRANCO, M. M.; FALCÃO, A. C. Linear regression for calibration lines revisited: weighting schemes for bioanalytical methods. **Journal of Chromatography B**, v. 774, n. 2, p. 215–222, 2002.

215 SPIZZO, G. *et al.* EpCAM expression in primary tumour tissues and metastases: An

immunohistochemical analysis. **Journal of Clinical Pathology**, v. 64, n. 5, p. 415, 2011.

216 LUK, B. T. *et al*. Interfacial interactions between natural RBC membranes and synthetic polymeric nanoparticles. **Nanoscale**, v. 6, n. 5, p. 2730, 2014.

217 TRZPIS, M. *et al.* Epithelial cell adhesion molecule: more than a carcinoma marker and adhesion molecule. **American Journal of Pathology**, v. 171, n. 2, p. 386–395, 2007.

218 PRASAD, V. V. T. S.; GOPALAN, R. O. G. Continued use of MDA-MB-435, a melanoma cell line, as a model for human breast cancer, even in year, 2014. **npj Breast Cancer**, v. 1, n. 1, p. 15002, 2015.

219 HUME, R. D. *et al*. Tumour cell invasiveness and response to chemotherapeutics in adipocyte invested 3D engineered anisotropic collagen scaffolds. **Scientific Reports**, v. 8, n. 1, p. 12658, 2018.

220 BISSELL, M. J. *et al*. The organizing principle: microenvironmental influences in the normal and malignant breast. **Differentiation**, v. 70, n. 9-10, p. 537–546, 2002.

221 RAO, L. *et al.* Cancer cell membrane-coated nanoparticles for personalized therapy in patient-derived xenograft models. **Advanced Functional Materials**, v. 29, n. 51, p. 1905671, 2019.

222 WAGNER, V. *et al*. The emerging nanomedicine landscape. **Nature Biotechnology**, v. 24, n. 10, p. 1211–1217, 2006.

223 MIN, Y. *et al*. Clinical translation of nanomedicine. **Chemical Reviews**, v. 115, n. 19, p. 11147–11190, 2015.

224 VAN DER MEEL, R. *et al*. Smart cancer nanomedicine. **Nature Nanotechnology**, v. 14, n. 11, p. 1007–1017, 2019.

225 NAMIKI, Y. *et al*. Nanomedicine for cancer: Lipid-based nanostructures for drug delivery and monitoring. **Accounts of Chemical Research**, v. 44, n. 10, p. 1080–1093, 2011.

226 BELTRÁN-GRACIA, E. *et al.* **Nanomedicine review:** clinical developments in liposomal applications. Vienna: Springer, 2019. v. 10

227 PATRA, J. K. *et al*. Nano based drug delivery systems: recent developments and future prospects. **Journal of Nanobiotechnology**, v. 16, n. 1, p. 1–33, 2018.

228 DE JESUS, M. B.; ZUHORN, I. S. Solid lipid nanoparticles as nucleic acid delivery system: properties and molecular mechanisms. **Journal of Controlled Release**, v. 201, p. 1–13, 2015.

229 CULLIS, P. R.; HOPE, M. J. Lipid nanoparticle systems for enabling gene therapies. **Molecular Therapy**, v. 25, n. 7, p. 1467–1475, 2017.

230 HAO, G.; XU, Z. P.; LI, L. Manipulating extracellular tumour pH: an effective target for cancer therapy. **RSC Advances**, v. 8, n. 39, p. 22182–22192, 2018.

231 WANG, W. J. *et al*. Multi-functional drug carrier micelles with anti-inflammatory drug. **Frontiers in Chemistry**, v. 7, n. FEB, p. 1–11, 2019.

232 STUART, M. A C. *et al*. Emerging applications of stimuli-responsive polymer materials. **Nature Materials**, v. 9, n. 2, p. 101–13, 2010.

233 CABANE, E. *et al.* Stimuli-responsive polymers and their applications in nanomedicine**. Biointerphases**, 2012. DOI: 10.1007/s13758-011-0009-3

234 HAJEBI, S. *et al*. Stimulus-responsive polymeric nanogels as smart drug delivery systems. **Acta Biomaterialia**, v. 92, p. 1–18, 2019.

235 SCHMALJOHANN, D. Thermo- and pH-responsive polymers in drug delivery**. Advanced Drug Delivery Reviews**, v. 58, n. 15, p. 1655, 2006.

236 YANG, W. *et al*. Smart nanovesicle-mediated immunogenic cell death through tumor microenvironment modulation for effective photodynamic immunotherapy. **ACS Nano**, v. 14, p. 620–631, 2020.

237 OROOJALIAN, F. *et al*. Encapsulation of thermo-responsive gel in pH-sensitive polymersomes as dual-responsive smart carriers for controlled release of doxorubicin. **Journal of Controlled Release**, v. 288, n. August, p. 45–61, 2018.

238 RADAIC, A.; DE PAULA, E.; DE JESUS, M. Factorial design and development of solid lipid nanoparticles (SLN) for gene delivery. **Journal of Nanoscience and Nanotechnology**, v. 14, p. 1–8, 4 abr. 2014.

239 KULKARNI, J. A.; CULLIS, P. R.; VAN DER MEEL, R. Lipid nanoparticles enabling gene therapies: from concepts to clinical utility. **Nucleic Acid Therapeutics**, v. 28, n. 3, p. 146–157, 2018.

240 KULKARNI, J. A. *et al*. Lipid nanoparticle technology for clinical translation of siRNA therapeutics. **Accounts of Chemical Research**, v. 52, n. 9, p. 2435–2444, 2019.

241 AFFRAM, K. O. *et al.* Cytotoxic effects of gemcitabine-loaded solid lipid nanoparticles in pancreatic cancer cells. **Journal of Drug Delivery Science and Technology**, v. 55, p. 101374, 2020.

242 GARCÍA-PINEL, B. *et al*. Lipid-based nanoparticles: application and recent advances in cancer treatment. **Nanomaterials,** v. 9, n. 4, p. 638, 2019.

243 MATHUR, V. *et al*. Solid lipid nanoparticles in cancer therapy. **International Journal of Drug Delivery**, v. 2, n. 3, 2010. DOI: 10.5138/ijdd.2010.0975.0215.02029.

244 SARMENTO, B. *et al*. Oral insulin delivery by means of solid lipid nanoparticles. **International Journal of Nanomedicine**, v. 2, n. 4, p. 743–749, 2007.

245 ANDREOZZI, E. *et al*. Novel method to label solid lipid nanoparticles with Cu-64 for positron emission tomography imaging. **Bioconjugate chemistry**, v. 22, p. 808–818, 2011.

246 AYAN, A. K.; YENILMEZ, A.; EROGLU, H. Evaluation of radiolabeled curcumin-loaded solid lipid nanoparticles usage as an imaging agent in liver-spleen scintigraphy. **Materials Science & Engineering C:** materials for biological applications, v. 75, p. 663–670, 2017.

247 OUMZIL, K. *et al.* Solid lipid nanoparticles for image-guided therapy of atherosclerosis.

Bioconjugate Chemistry, v. 27, n. 3, p. 569–575, 2016.

248 BARENHOLZ, Y. (CHEZY). Doxil® — The first FDA-approved nano-drug: lessons learned. **Journal of Controlled Release**, v. 160, n. 2, p. 117–134, 2012.

249 FELGNER, P. L. *et al*. Lipofection: a highly efficient, lipid-mediated DNA-transfection procedure. **Proceedings of the National Academy of Sciences**, v. 84, n. 21, p. 7413 LP – 7417, 1987.

250 JINHAO, G. A. O.; HONGWEI, G. U.; BING, X. U. Multifunctional magnetic nanoparticles: design, synthesis, and biomedical applications. **Accounts of Chemical Research**, v. 42, n. 8, p. 1097, 2009.

251 DASGUPTA, A. *et al.* Ultrasound-mediated drug delivery to the brain: principles, progress and prospects**. Drug Discovery Today:** technologies, v. 20, 2016. DOI: 10.1016/j.ddtec.2016.07.007.

252 BEAUTÉ, L.; MCCLENAGHAN, N.; LECOMMANDOUX, S. Photo-triggered polymer nanomedicines: From molecular mechanisms to therapeutic applications. **Advanced Drug Delivery Reviews**, v. 138, p. 148–166, 2019.

253 YATVIN, M. B. *et al.* Design of liposomes for enhanced local release of drugs by hyperthermia. **Science**, v. 202, n. 4374, p. 1290 LP – 1293, 1978.

254 SUN, Z. *et al.* Photo- and reduction-responsive polymersomes for programmed release of small and macromolecular payloads. **Biomacromolecules**, v. 19, n. 6, p. 2071–2081, 2018.

255 DUAN, Y. *et al*. Light-triggered nitric oxide (NO) release from photoresponsive polymersomes for corneal wound healing. **Chemical Science**, v. 11, n. 1, p. 186–194, 2019.

256 IOELE, G. *et al.* Photosensitive drugs: a review on their photoprotection by liposomes and cyclodextrins. **Drug Delivery**, v. 24, n. 2, p. 33–44, 2017.

257 BUNKER, A.; MAGARKAR, A.; VIITALA, T. Rational design of liposomal drug delivery systems, a review: combined experimental and computational studies of lipid membranes, liposomes and their PEGylation. **Biochimica et Biophysica Acta (BBA) -** biomembranes, v. 1858, n. 10, p. 2334–2352, 2016.

258 IMMORDINO, M. L.; DOSIO, F.; CATTEL, L. Stealth liposomes: review of the basic science, rationale, and clinical applications, existing and potential**. International Journal of Nanomedicine**, v. 1, n. 3, p. 297, 2006.

259 SCHÜHLE, D. T. *et al*. Liposomes with conjugates of a calix[4]arene and a Gd-DOTA derivative on the outside surface; an efficient potential contrast agent for MRI. **Chemical Communications**, v. 46, n. 24, p. 4399–43401, 2010.

260 MACHÁČEK, M. *et al*. Binding of an amphiphilic phthalocyanine to pre-formed liposomes confers light-triggered cargo release. **Journal of Materials Chemistry B**, v. 6, n. 44, p. 7298–7305, 2018.

261 TROUTMAN, T. S.; LEUNG, S. J.; ROMANOWSKI, M. Light-induced content release from plasmon-resonant liposomes. **Advanced Materials**, v. 21, n. 22, p. 2334–2338, 2009.

262 SAHU, A. *et al*. Nanographene oxide as a switch for CW/pulsed NIR laser triggered drug release from liposomes. **Materials Science and Engineering C**, v. 82, n. July 2017, p. 19–24, 2018.

263 KOÇER, A. *et al.* A light-actuated nanovalve derived from a channel protein. **Science**, v. 309, n. 5735, p. 755–8, 2005.

264 ZHOU, Q. *et al*. Unidirectional rotating molecular motors dynamically interact with adsorbed proteins to direct the fate of mesenchymal stem cells. **Science Advances**, v. 6, n. 5, p. eaay2756, 2020.

265 GARCÍA-LÓPEZ, V. *et al*. Molecular machines open cell membranes. **Nature**, v. 548, n. 7669, p. 567–572, 2017.

266 KISTEMAKER, J. C. M. *et al*. Third-generation light-driven symmetric molecular motors. **Journal of the American Chemical Society**, v. 139, n. 28, p. 9650–9661, 2017.

267 CHEN, J. *et al*. Facile assembly of light-driven molecular motors onto a solid surface. **Chemical Communications**, v. 50, n. 84, p. 12641–12644, 2014.

268 VON NESSEN, K.; KARG, M.; HELLWEG, T. Thermoresponsive poly-(N-isopropylmethacrylamide) microgels: Tailoring particle size by interfacial tension control. **Polymer**, v. 54, n. 21, p. 5499–5510, 2013.

APPENDICES

Appendix A – Supporting Information: Low nanogel stiffness favors nanogel transcytosis across the blood-brain barrier

Nanogels size dependence of sodium dodecyl sulfate (SDS) concentration and polymerization time.

The presence of surfactants in the synthesis of nanogels affects size and monodispersity.[25, 268] To obtain nanogels in the range of 200 and 400 nm, we study the polymerization time and SDS concentration effect on 5 mol% BIS nanogels. SDS concentration effect on nanogels size and dispersity was studied by preparing a solution containing 604 mg of NIPMAM, 39 mg of BIS (5 mol%), 10 mg of NLB and different concentrations of SDS from a 0.25 M SDS solution, at a final volume of 45 ml of ddH_2O in a round flask. This solution was left stirring under a N_2 flux for 30 min. After 30 min, the solution was placed in an oil bath at 70ºC still under stirring (400 rpm) for 30 min to reach temperature equilibration. In parallel, 11 mg of APS in 5 ml of ddH_2O was also under N_2 flux for 60 min. The initiator was added to the round flask containing NIPMAM, BIS, NLB and SDS using a syringe with a needle and the reaction has occurred for at least 6 hours.

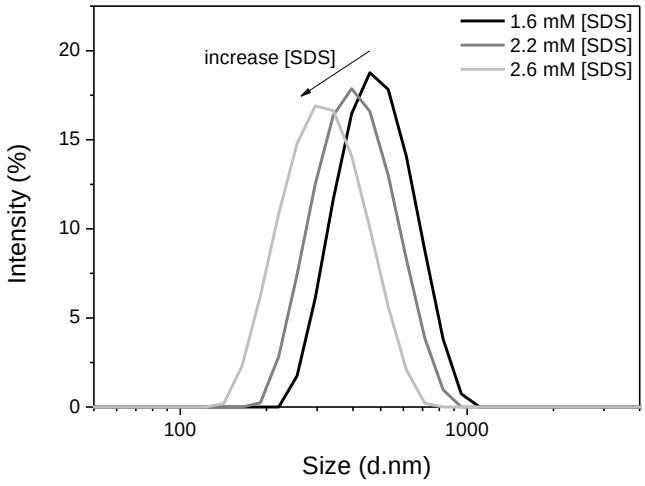

Figure S1 - Hydrodynamic diameter of p(NIPMAM) nanogels with 5 mol% BIS in ddH_2O synthesized in the presence of 1.6, 2.2 and 2.6 mM of SDS with polymerization time above 6 hours.
Source: By the author.

Figure S1 shows the size distribution of hydrodynamic diameter with different concentration of SDS. It was observed that there is a limitation for SDS amount to produce monodisperse nanogels above 2.7 mM of SDS for 5 mol% BIS containing p(NIPMAM) nanogels even at concentrations below SDS critical micelle concentration of 8.2 mM in water.

To investigate nanogels size and dispersity as a function of polymerization time, the previously described synthesis conditions were employed although SDS added amount was fixed at 38 mg. Polymerization time is considered from the moment the initiator was added. To collect the samples at each time point, a syringe with a long needle was employed and 0.5 ml was collected every 30 min. Between 90 and 240 min of reaction an increase in particle size is observed and, from 270 min of reaction there was no significant change of the size of the nanogels which relates to the consumption of the initiator, APS (Figure S2).

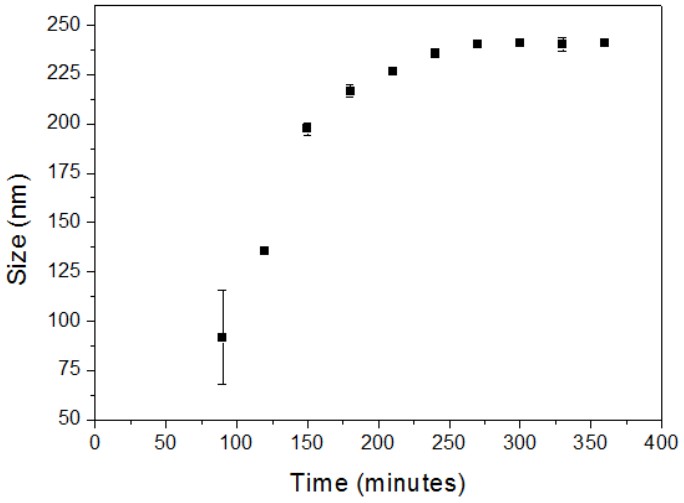

Figure S2 - P(NIPMAM) nanogels (5 mol% BIS) hydrodynamic diameter as function of polymerization time Values represented are mean ± SD of 3 measurements from the same batch.
Source: By the author.

Nanogels fluorescence and flow cytometry

The nanogels have different fluorescence intensities at same concentration. Figure S3a displays the spectra for each nanogels from 645 to 1000 nm with excitation at 633 nm.

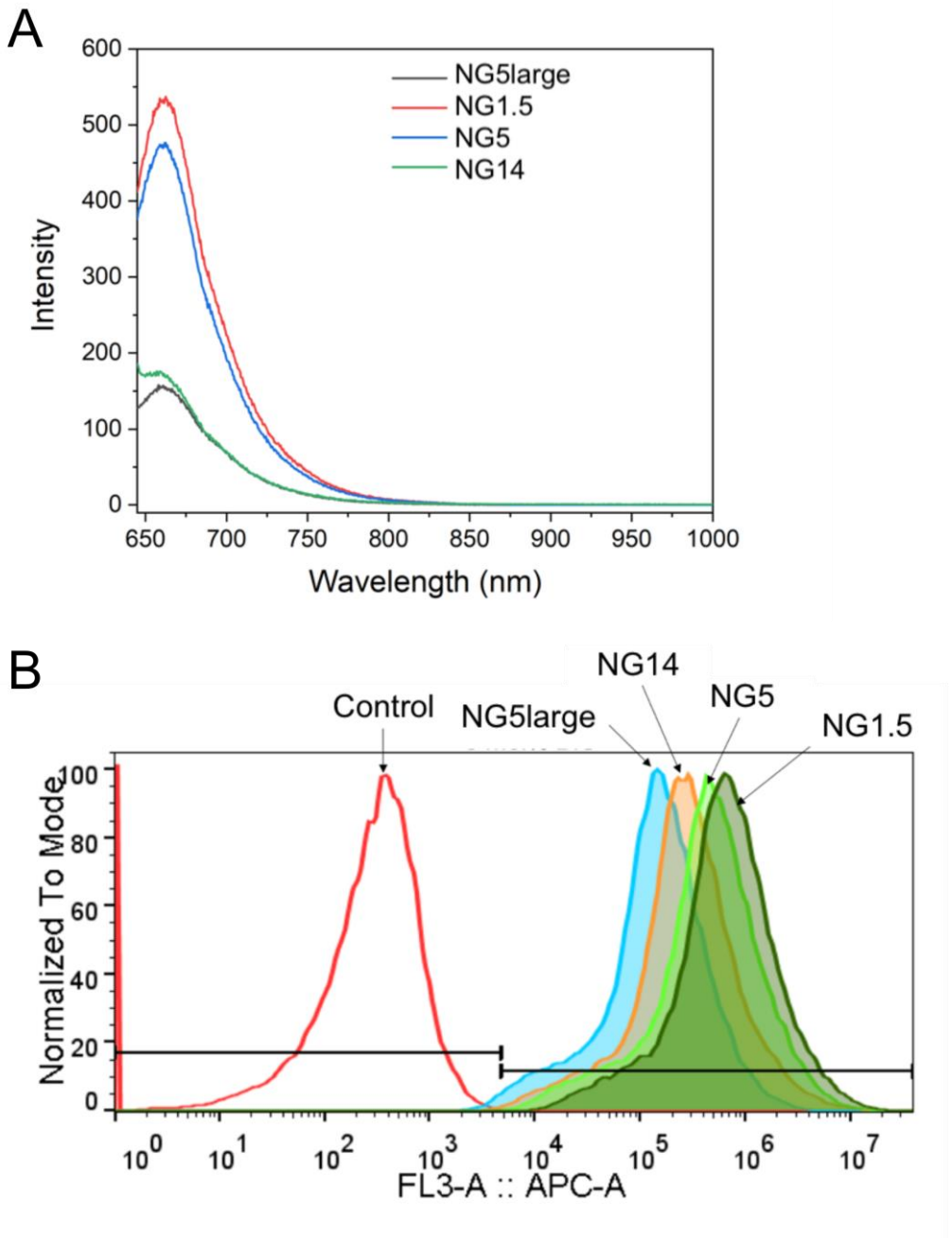

Figure S3 - A) Fluorescence of Nile blue in p(NIPMAM) nanogels in EMB-2 complete medium at 100 µg ml^{-1} with excitation at 633 nm and emission was record from 645 to 1000 nm, and B) flow cytometry histogram profiles of hCMEC/D3 cells after nanogels incubation for 2 hours at 37ºC using the APC channel (670/30 band pass filter) and laser excitation 640 nm.
Source: By the author.

Figure S3B show the histogram profile of each nanogel after 2 h incubation with hCMEC/D3 polarized cell layer highlighting the different fluorescence intensity between nanogels and in agreement with the spectra at Figure S3A.

Table S1 - APC positive populations frequency for nile blue-labelled nanogels with different cross-linking densities.

Nanogel	% positive cells (APC+)			
	15 min, 37°C	30 min, 37°C	2 h, 37°C	2 h, 4°C
1.5 mol% BIS	99.93 ± 0.05	100	99.97 ± 0.05	95.0 ± 4.5
5 mol% BIS	99.8 ± 0.2	99.9 ± 0.1	99.93 ± 0.05	92 ± 5
14 mol% BIS	99.7 ± 0.2	99.77 ± 0.09	99.87 ± 0.09	86 ± 6

Source: By the author.

PDMS mold preparation

Polydimethylsiloxane (PDMS) mold was prepared by mixing PDMS elastomer and silicone elastomer curing agent at mixing ratio 10:1 of curing agent to elastomer using the Sylgard^{TM} 184 Silicone Elastomer Kit. The mix was degassed and poured in a plastic plate and left curing overnight at 70ºC. PDMS gel was cut and holes were punched to be mold to the collagen gels. The pieces were placed over glass slides and plasma treated to bond PDMS to the glass (Figure S4A). To sterilize the pieces, they were placed at 180ºC for 4 hours in closed glass containers further opened only under flow hood and transferred to 4 wells sterile plate where the collagen gel was placed inside the holes.

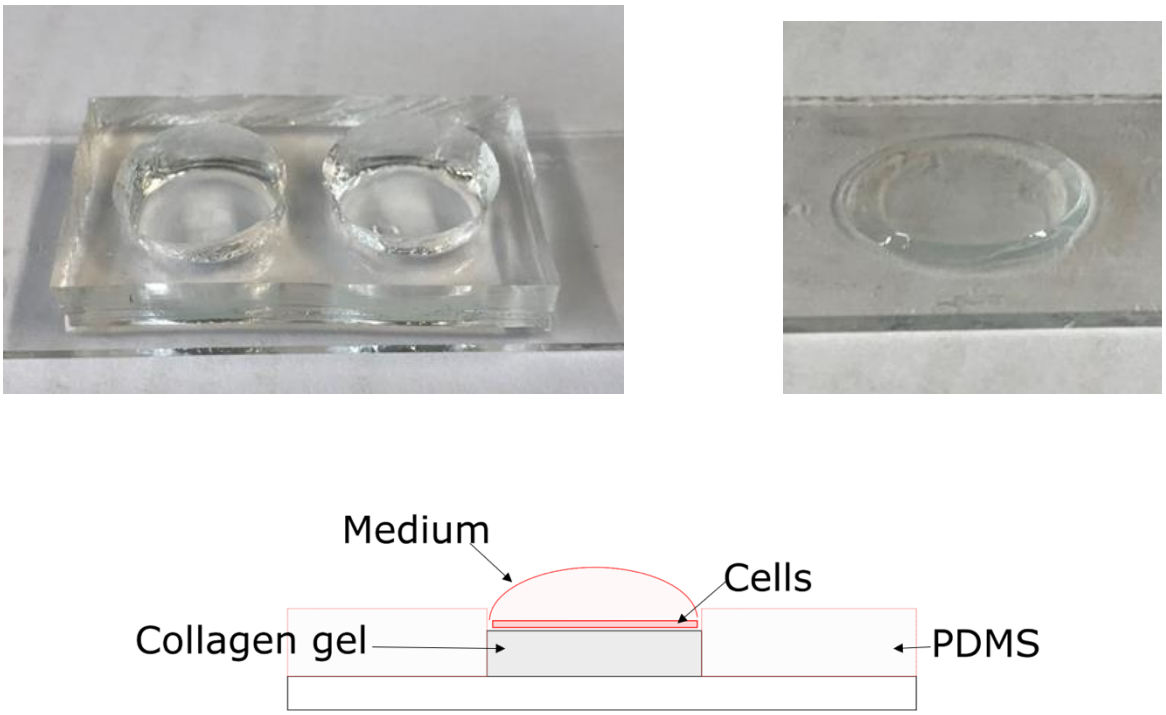

Figure S4 - A) PDMS mold after plasma treatment, B) hCMEC/D3 polarized layer on collagen gel after PDMS mold removal and C) schematic representation of PDMS mold containing collagen gel and hCMEC/D3 cell layer.
Source: By the author.

Figure S4B displays a collagen gel with a polarized cell layer after nanogel incubation and staining for microscopy followed by removal of PDMS mold and careful placement of a glass cover slip.

Appendix B – Supporting Information

The HPLC method presented good stability in matrix and no coeluted peaks were observe with the paclitaxel peak at retention time 6.7 minutes.

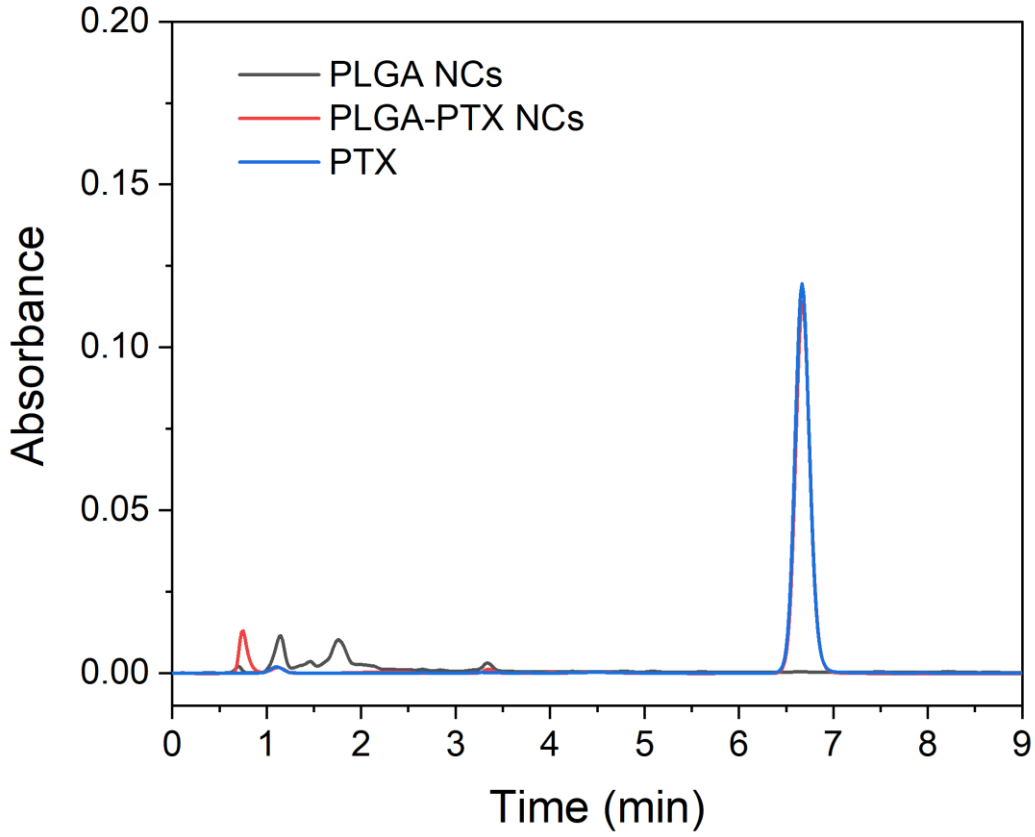

Figure S1 - HPLC chromatograms for evaluation of matrix influence for the determination of encapsulation efficiency of paclitaxel in PLGA NCs.
Source: By the author.

Representative images of PLGA-NLR and mPLGA-NLR NCs interaction with MCF-7 and MCF-10A cells after 1 h incubation.

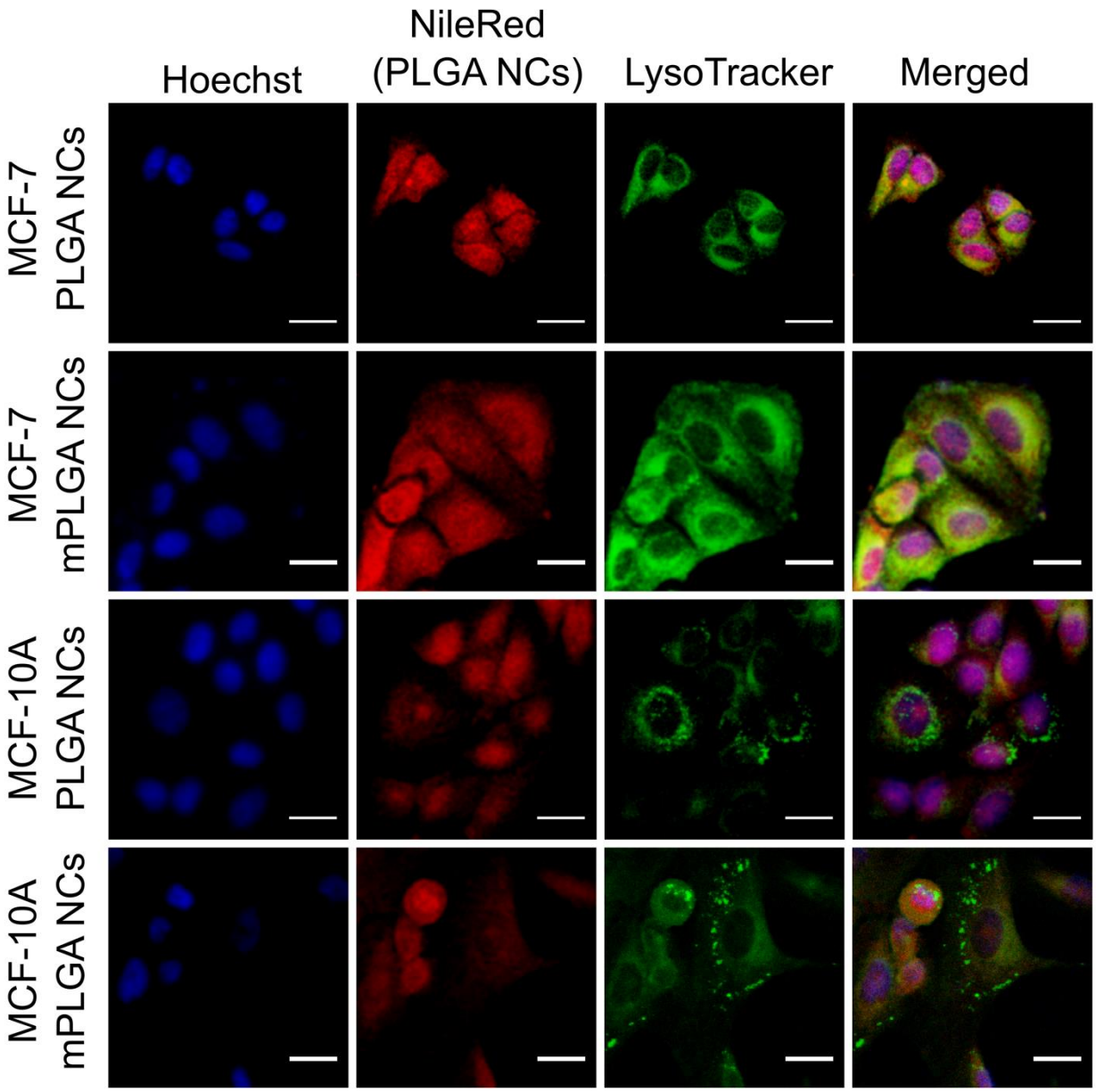

Figure S2 - Confocal laser scanning images of MCF-7 and MCF-10A cells treated with coated and non-coated PLGA-NLR NCs for 4 hours. Cell were imaged with a 63x oil-immersion objective and acquired in z-stacks at 0.4 µm intervals, 512 x 512 pixels.

Source: By the author.